MODELING OF CONTINUOUS CASTING MOLD POWDER BEHAVIOR: HEAT TRANSFER, COMBUSTION, SINTERING, AND MELTING

by

Lipsa Das

A thesis submitted to the Faculty and the Board of Trustees of the Colorado School of Mines in partial fulfillment of the requirements for the degree of Doctor of Philosophy (Thermal-Fluids).

Golden, Colorado

Date _____

Signed: _____

Lipsa Das

Signed: _____

Dr. Brian G. Thomas
Thesis Advisor

Golden, Colorado

Date _____

Signed: _____

Dr. Anthony Petrella
Professor and Department Head
Department of Mechanical Engineering

ABSTRACT

A model of temperature distribution, carbon and gas concentrations, and powder and melt pool thickness evolution has been developed for the top-surface powder layers in the continuous-casting process. Mold powder is added to the continuous caster to provide thermal and chemical insulation (prevent re-oxidation of steel), to supply liquid flux into the gap to provide lubrication, and to control horizontal heat transfer across the air gap between the copper mold and re-solidified flux, and to absorb and remove inclusions from molten steel. Therefore, maintaining sufficient powder and liquid flux layer thicknesses is important to achieve these functions. Understanding the powder melting behavior is key to maintaining a stable and adequate liquid pool thickness. Free carbon in the mold powder controls the melting rate and its concentration evolution is influenced by heat, mass transfer, and gas transport through the porous powder bed. The powder/slag region is modeled with a 1-D, fixed-grid, transient, advection-diffusion finite-volume model, and includes phase change and melting, powder densification, carbon burning, gas evolution, gas transport, and exhaust phenomena. The steady-state model has been verified with an analytical solution, and with a model with a commercial package. The transient heat transfer model has been validated with plant measurements in operating commercial slab casters, and applied to study the effect of powder properties/casting conditions, and automated vs. manual feeding. The multiphysics model including the effects of heat and mass transfer, sintering, combustion, and gas transport has been validated with lab sintering measurements. Finally, the multiphysics model has been applied to the continuous caster. The carbon in the mold powder is advected due to powder shrinkage, and liquid flux consumption, which results in carbon enrichment in the sinter layer near the bottom of the powder, which is more than in the lab experiment. This novel multiphysics model of top-surface powder behavior is a valuable tool in understanding the phenomena governing temperature, powder/slag thickness, and powder melting rate in the continuous casting process.

Keywords: Heat Transfer, Mass Transfer, Sintering, Powder Melting, Carbon combustion, Gas Transport, Finite volume, Multiphysics model, Continuous casting, Mold powders

TABLE OF CONTENTS

LIST OF FIGURES

LIST OF TABLES

LIST OF SYMBOLS

Ambient Temperature . . . . . T_{amb}

Atomic Oxygen . . . . . O

Carbon Dioxide . . . . . CO_2

Carbon monoxide . . . . . CO

Carbon volume fraction . . . . . g_C

Density . . . . . ρ

Domain bottom . . . . . $w_{final,1}$

Domain top . . . . . $w_{final,4}$

Effective Gas diffusivity . . . . . D_{eff}

Effective Heat transfer coefficient . . . . . h_{tot}

Effective Thermal conductivity . . . . . k_{eff}

Fully sintered Density . . . . . ρ_s

Gas constant . . . . . R_g

Gas species mole fractions . . . . . $x_{O_2}, x_O, x_{CO_2}, x_{CO}, x_{CO}, x_{N_2}$

Gas species moles . . . . . $n_{O_2}, n_O, n_{CO_2}, n_{CO}, n_{CO}, n_{N_2}$

Global Time . . . . . t

Grid location (vertical) . . . . . z

Liquid flux Density . . . . . ρ_f

Local time . . . . . t_{local}

Moles of carbon . . . . . n_C

Molten flux-sinter interface . . . . . $w_{final,2}$

Molten steel temperature . . . . . $T_{melt,steel}$

Nitrogen . . . . . N_2

Nusselt number . . . . . Nu

Oscillation frequency . . . . . f

Oxygen . . . . . O_2

Pore fraction . . . . . α_g

Powder Density . . . . . ρ_{app}

Powder Density at room temperature . . . . . $\rho_{app,0}$

Powder Shrinkage velocity . . . . . $v_{shrink,p}$

Powder Softening Temperature . . . . . T_{sof}

Powder top surface . . . . . $w_{final,3}$

Powder tortuosity . . . . . τ

Prandtl number . . . . . Pr

Pressure . . . . . P

Rayleigh number . . . . . Ra

Reaction Rates . . . . . r_1, r_2, r_3, r_4

Reaction equilibrium constants . . . . . K_1, K_2, K_3, K_4

Reaction rate constants . . . . . $k_{CO,O}, k_{CO,O_2}, k_1, k_2, k_3, k_{O_2}$

Reynolds number . . . . . Re

Sintering rate constant . . . . . K_s

Slag melting temperature . . . . . $T_{melt,slag}$

Specific heat . . . . . c_p

Strand cross-section area . . . . . A_c

Strand thickness . . . . . th

Strand width . . . . . W

Temperature . . . . . T

Thermal conductivity . . . . . k

Total gas concentration . . . . . c_g

Total gas moles . . . . . $n_{tot,g}$

LIST OF ABBREVIATIONS

Continuous Caster CC

Four Equation combustion Model 4-eCM

Heat transfer coefficient . . . . . HTC

High Strength Low Alloy . . . . . HSLA

Medium carbon . . . . . MC

Narrow Face . . . . . NF

Steady State . . . . . SS

Submerged Entry Nozzle . . . . . SEN

Ultra-low Carbon . . . . . ULC

Wide Face . . . . . WF

ACKNOWLEDGMENTS

I thank my research advisor, Prof. Brian G. Thomas for his guidance and teaching which has shaped my outlook on solving research problems, and taught me to systematically develop different layers of the project, and build on new knowledge gained during this process. I have learned a lot from his extensive knowledge and wisdom, and thank him for his continuous support and encouragement over the years. I have worked on different aspects of the casting process from developing a Primary Dendrite Arm Spacing (PDAS) model, simulating fluid flow, transport and capture of bubble, and slag particles in the Continuous Casting strand to developing a Multiphysics mold powder model under his guidance, and have significantly improved my computational abilities during this process. I am thankful for our brainstorming sessions during model development, and debugging, which have helped me appreciate the subtle nuances of numerical modeling, and further improve the model. From writing better codes to model complex multiphysics, and making it more efficient, to communicating the practical aspects of the casting process, his guidance has been valuable.

I gratefully acknowledge the financial support by the member companies of Continuous Casting Center (CCC) at Colorado School of Mines, which includes: Baosteel, Cleveland Cliffs, CBMM, Evraz, JFE Steel Corp., RHI Magnesita, Nucor Steel, Pukyong/Posco, SSAB, Tata Steel, USS, voestalpine, ANSYS/ Fluent. I would also like to thank the National Science Foundation (NSF) for providing financial support (Grant: CMMI-18-08731). I especially thank researchers at TATA Steel, Netherlands, Stefan Senge, Jan Kromhout, Edward Dekker, Ton Spierings, Dirk van der Plas for their support and collaboration on the mold powder model, and for providing us with measurements to validate our model, and for sharing their knowledge, and experience with us. I am also thankful to Dofasco researchers, Joydeep Sengupta, Jackie Leung and Bruce Farrand, and previous CCC researchers Matt Zappulla, and Adnan Akhtar, for previous plant measurements involving nail dipping at ArcelorMittal Dofasco (2015). I thank Ansys Inc. Academic Partnership Program for FLUENT license for model verification runs.

I thank my thesis committee members: Prof. Robert Braun, Prof. Gregory Jackson, Prof. Emmanuel De Moor, Prof. Nils Tilton, and Prof. Denis Aslangil for sharing their knowledge and insights with me, which helped improve our work. I thank all the committee members for their continuous support and encouragement during my PhD journey. I am also grateful to Prof. Gregory Bogin, and Prof. Jason Porter for their exciting courses, which helped me develop a fundamental understanding of transport phenomena, and taught me the ability to create in-house codes.

I thank Prof. Dipak Mazumdar, Indian Institute of Technology (IIT), Kanpur for introducing me to transport phenomena during my M.Tech., and for continuously encouraging me to go deeper into the field.

I am thankful to my CCC researchers, Dr. Seong Mook Cho, and Matt Zappula for their help, and advice, and colleagues Mingyi Liang,and Hamed Olia, for their immense support, and encouragement, and for our insightful research discussions. I also thank Dylan Palmer, Vipul Gupta, and Ehsan Jebellat for their support. I thank ME, seniors, Jicheng Lou, and Gandhali Kogekar for their mentorship during my initial years.

I thank my friends, Malavikha Rajiv Moorthy, Milan Agnani, Mayuri Kushare, Rohit Bardpurkar, Amogh Thatte, Keerthana Krishnan, Shneka Muthukumaraswamy, Akshit Sharma, Nandini Negi, Pratyasha Mohapatra, Megha Acharya, Sampreeti Jena for their support and encouragement during my PhD journey.

I thank our family friends, Sadhu Behera and Sunanda Prusty for their support, and encouragement.

Finally, I thank my parents, Biswakabi Das, and Kalyani Das, and grandparents, Banamabar Das, and Dr. Kiranbala Das for their immense love, blessings, and words of wisdom and encouragement that have inspired me to keep going during difficult times.

This thesis is dedicated to my parents, Biswakabi Das and Kalyani Das.

For their endless love, blessings, and encouragement.

CHAPTER 1

INTRODUCTION

Steel is one of the most recycled and widely used materials in today's world. While ingot casting produces a small fraction of steel products in special-alloy steel plants, almost 96 % of the world's steel [1] is produced by the continuous casting process (Figure 1.1).

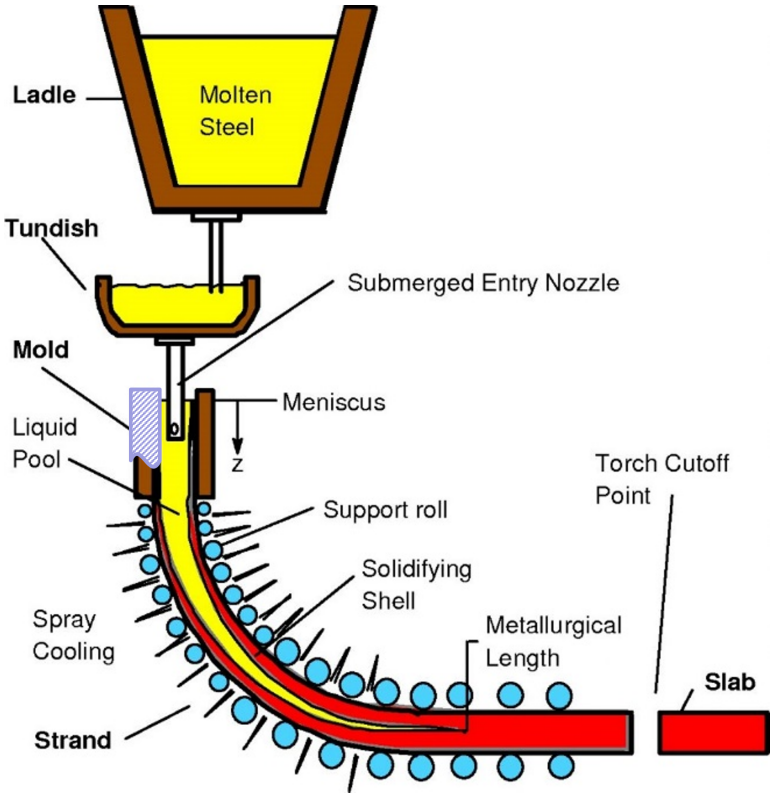

Figure 1.1 Continuous Casting process schematic [2]

1.1 Continuous Casting Process

Continuous casting involves the solidification of molten steel into slabs, billets, or blooms which later get rolled, and finished into final products. Molten steel flows from the ladle through a tundish into a mold through a submerged entry nozzle (SEN). The flow bifurcates through the ports toward the narrow face mold walls. Depending on many factors, such as the port angle, nozzle clogging, etc., the flow can either be symmetric, or asymmetric, which can affect the heat transfer and inclusion removal from steel. The continuous slab-casting mold ($\sim 1m$ in length) in Figure 1.1 consists of four copper plates with

water-cooling channels, which remove heat from the molten steel to solidify it along the mold walls. This horizontal heat transfer through the mold, solidifying steel shell, and air gap has an important effect on steel surface quality after it is cast. In a slab caster, the mold consists of two wide faces (WF) and two narrow faces (NF). The mold oscillates (at a frequency of 1-5 Hz) vertically to prevent sticking of the steel shell to the mold walls. There are drive rolls to pull the shell downward at a casting speed, which balances with the incoming liquid steel so that the process runs in steady state. The shell thickness keeps increasing, and by the time it reaches near mold exit, it is about 30 mm thick and can support the remaining liquid.

1.2 Research Motivation and Background

The top half of the copper mold (which is a closeup of the region containing the blue rectangle in Figure 1.1) is illustrated in Figure 1.2. Note Figure 1.1 is showing the edge view of two wide face molds in a view looking at the narrow faces, while Figure 1.2 is showing the front view where the mold is one of the narrow faces.

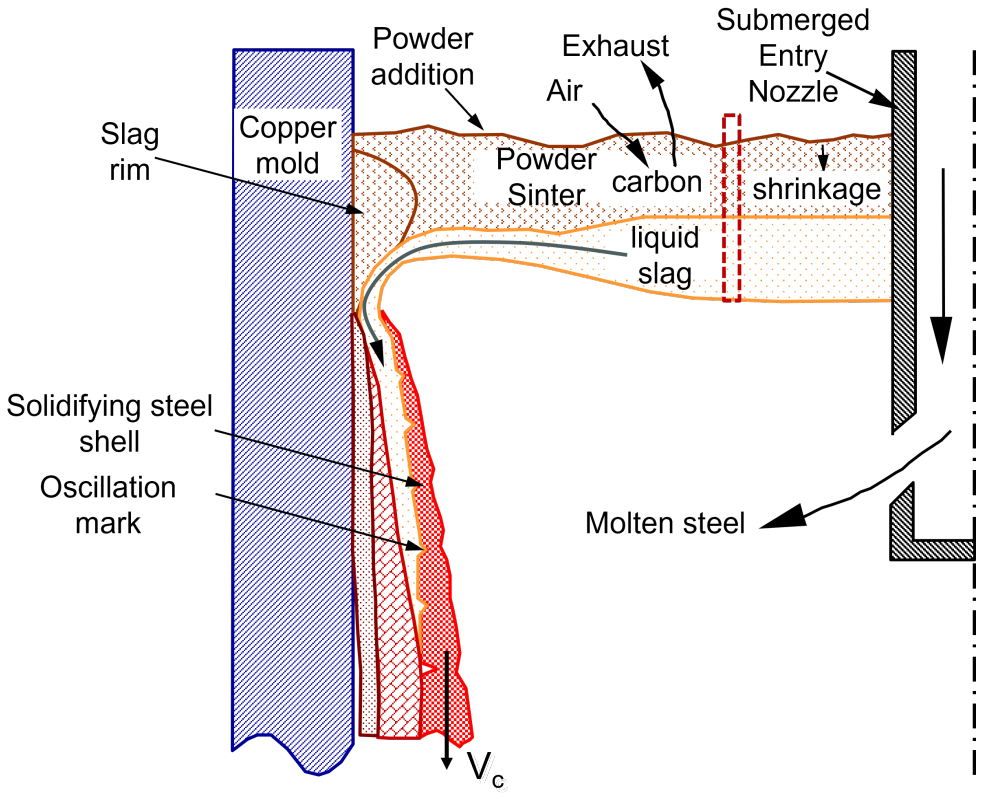

Figure 1.2 Schematic of phenomena with current model domain (red dotted rectangle) [3]

In continuous casting of steel, mold powder is added to the top surface of the molten steel in the mold to provide thermal insulation to prevent heat loss from the molten steel, which could result in significant

drops in liquid metal temperature, and in extreme cases can lead to meniscus freezing. Mold powder is also essential to prevent reoxidation by providing chemical insulation [4–7], as molten steel might come in contact with oxygen from the ambient, and re-oxidize to form detrimental particles which can jeopardize steel quality.

Mold powder melts to form liquid slag which can absorb inclusions such as alumina from molten steel, and improve the final steel quality. Additionally, the liquid slag lubricates the gap between the solidifying steel shell and oscillating water-cooled copper mold, thereby preventing friction, controlling heat transfer across the gap, and helping in the removal of impurities in the steel. Due to any reason, if any of the above functions cannot occur properly, then this can lead to serious quality problems, such as caused by mold powder entrapment (depending on fluid flow and surface tension, etc.), insufficient liquid flux feeding into the gap, thereby increasing friction. This can also lead to various surface defects, and in severe cases, breakouts [8] in the plant, which cause the casting to stop temporarily to restore standard casting conditions.

While heat transfer across the interfacial gap is important to steel surface quality, vertical heat transfer through the top surface of the mold powder is needed to provide thermal insulation, and stable melting so that the top surface does not freeze (one of the main purposes of controlling vertical heat transfer). Meniscus freezing can cause re-oxidation leading to detrimental oxide inclusions in the final product.

Mold powders are essential to prevent oxidation and meniscus freezing and to avoid contamination, such as caused by carbon from the sintered layer coming into contact with ultra-low carbon molten steel. The melting rate should be controlled to provide sufficient liquid flux flow into the gap for proper lubrication, while not being excessive, and also to prevent the carbon-rich sintered layer from coming in contact with the molten steel. It is important to maintain a stable liquid slag layer that is thick enough to completely cover the molten steel, and to provide continuous feeding into the interfacial gap. However, the liquid slag layer should not be allowed to become too thick. An excessive melting rate can lead to increased slag entrainment, and the level fluctuations create slag "bears" or "ropes", which are very large solidified slag rims, that hinder slag infiltration into the gap, leading to surface defects (small slag rims always form and are very helpful if not too big).

Mold powders usually consist of a mixture of oxides mainly silica, alumina, calcium oxide, sodium oxide, and magnesium oxide with varying amounts of titania, zirconia, borium oxide, and lithium oxide. The powder contains three phases, namely the oxide mixture, air and carbonaceous content in form of isolated carbon as graphite, coke, lampblack or tied up as carbonate compounds. During the powder heating, various phenomena occur like moisture evaporation, decomposition of carbonates ($\sim 500°C$), combustion of unburnt carbon ($\sim 500 - 900°C$), sintering of mineral particles, and finally melting to form a

liquid slag pool above $900°C$ (Figure 1.2). The melting and reaction rates depend on the carbon content, porosity, density, size distribution of the powder particles, powder particle shape, thermal properties, and other controlling factors like the thickness of the powder layer and powder addition process, etc[9]. The free carbon in the mold powder helps regulate the slag melting rate, which is important for mold lubrication, and the formation of solid flux which controls heat transfer across the gap.

Figure 1.3 (a) and (b) show the transient sintering and melting process as powder particles move from top to bottom of the layer. The mold powder can be either granulated powder or ordinary fine powder. The granulated powders investigated in this study are manufactured such that the powder is heated with air to make the contents explode, creating hollow shells of the various oxides that comprise the powder, giving it very low density and high porosity ($\geq$70%). The particulate spheres (roughly spherical) are packed such that the external porosity is similar to body-centered cubic (32%), and the internal porosity is 50-60%, so the effective porosity of the hollow spheres (formed when the internal contents explode) becomes 70-80%. The size of non-granulated powder/slag particles in ordinary fine powder can range from 5-150µ, while that of the granulated powder/slag particles vary from 80-800 µ. The size of graphite particles is 45 µ.[10].

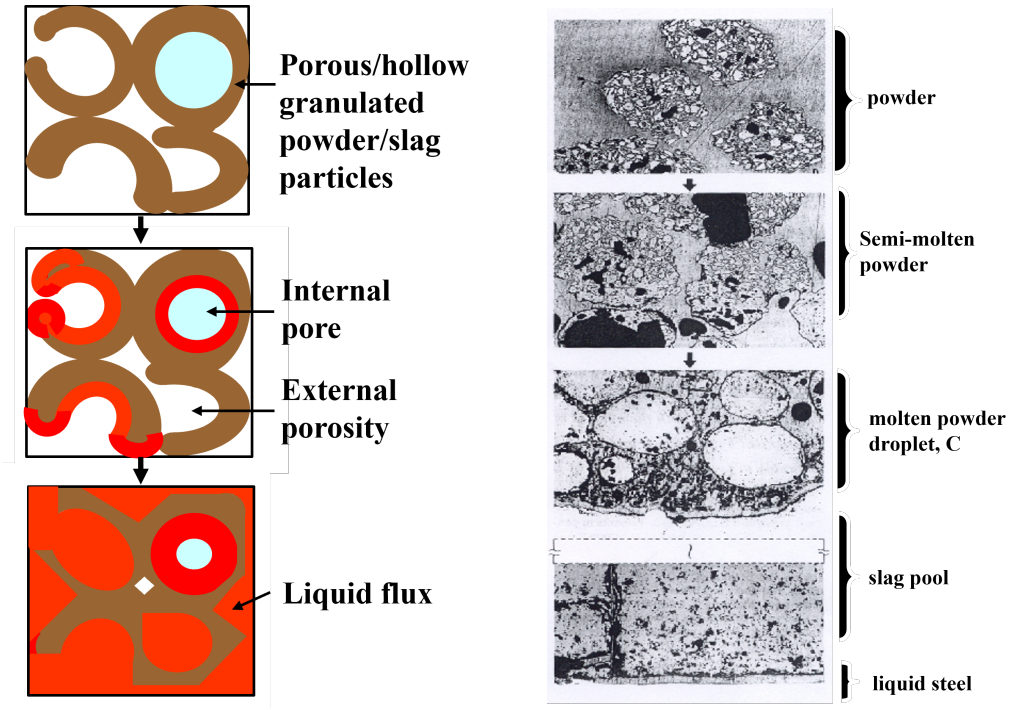

Figure 1.3 (a) Schematic of porous / hollow granulated powder/slag particles sintering and gradually melting (b) Micrographs of the powder sintering and melting process [11] (Powder heats up and minerals sinter. Gradually, the moisture evaporates, and carbonates decompose ($\sim 500°C$). Free carbon in the mold powder combusts ($\sim 500 - 900°C$), and eventually, the sintered powder melts to form a liquid slag pool above $900°C$

In order to control the melting rate, both types of powder are mixed with a prescribed amount of carbon, either integrated into the powder, or as separate carbon particles, called "free carbon". The top layer of the powder in the mold consists of the loose particles, as added from either an automated powder feeder or by pouring manually from a bag. These particles gradually undergo sintering and densification to produce a dense, C-enriched sinter layer towards the bottom and liquid slag. The sintered layer gradually accumulates carbon which has not burned away. The liquid slag gradually percolates down to form a molten slag/layer beneath the sintered layer, that floats above the molten steel. Towards the meniscus region, liquid slag is consumed into the gap between the solidifying steel shell and the copper mold wall during the oscillation cycles. The consumption rate depends on the oscillation practice, and conditions in the interfacial gap. This consumption greatly affects the thickness of the liquid slag layer, which acts as a reservoir for the consumption. Liquid slag consumed in this way acts to lubricate the gap between shell and mold, prevent friction, and regulate heat transfer in the gap. Please note that the words, 'liquid flux' and 'molten slag' are used interchangeably in this thesis, and refer to the molten powder.

The carbon in the powder has an important effect on the sintering and melting behavior [12–20]. Carbon controls the melting rate (adding carbon to the mold powder decreases the powder melting rate [21]), but the mechanism is not understood. Improving understanding of powder melting mechanisms by testing hypotheses is one of the objectives of the current research. The carbon also undergoes combustion [12–14] through several chemical reactions leading to the formation of carbon dioxide and carbon monoxide. These reactions are controlled by both chemical kinetics and diffusion [13, 22–29] due to the transport of oxygen into the powder, and the transport of combustion products upwards and out of the powder top surface. The combustion is controlled by chemical reaction at low temperatures (300 to 400 °C), and by mass transfer inside the powder and gas at high temperatures (600 to 800 °C) [13]. A region of mixed control is described to be present between these temperatures [13].

To date, the combustion and gas transport models have only been applied and compared with the lab sintering experiment, where detailed measurements are available. However, no model or experiment of carbon combustion exists for a commercial caster. It is difficult to conduct lab experiments to measure the combustion kinetics of mold powders in the presence of a liquid flux layer. It is also arduous to replicate all the plant conditions in a lab experiment or extrapolate the experimental results directly to the plant scenario. Few controlled quantitative lab experiments [12, 30, 31] exist in the literature that can be used as benchmark experiments. Plant experiments are also very difficult [32], and expensive to conduct, with often separate trials requiring special conditions that can result in rejecting the steel slab due to not meeting the product specifications. Therefore, computational models are a useful tool to investigate the process, to understand the mechanisms, and their relative importance. Hence, developing the model to

match the lab measurements available is a necessary step toward implementing the combustion behavior for a real caster simulation.

1.3 Research Objectives and Outline

This research aims to gain a fundamental understanding of mold powder behavior and develop a multi-phase, multi-physics computational model of the continuous casting mold powders considering heat and mass transfer, powder densification and shrinkage, carbon combustion and advection, gas diffusion, advection, and exhaust.

A summary of the specific research objectives are presented below:

- Develop a steady state model to calculate the temperature field through the mold slag layers, and verify it with an analytical solution, and an Ansys Fluent model
- Develop a transient thermal model (heat, and mass transfer module) to predict thermal behavior in mold powder/slag layers and verify it with a previous steady-state in-house code, and with an Ansys Fluent model
- Develop a Multiphysics model using the transient thermal model, which includes the following features:

  Rate kinetics of the sintering process for the powder/sinter layer, causing void fraction decrease and density increase with temperature and time

  A multi-species, 4-equation combustion model (4-eCM) with chemical reaction rates, gas diffusion, transport, and exhaust to predict resulting carbon and gas distributions
- Validate model with lab experiments of powder sintering (temperature, carbon and exhaust gas distribution)
- Apply the model to a commercial continuous caster (including liquid flux layer, and slag consumption into the gap) and validate with available plant measurements (temperature, powder/slag layer thicknesses)

First, a steady-state heat transfer model is developed which is verified with Ansys Fluent, and an analytical solution derived by the author. Following this, a transient heat and mass transfer model is developed, and the calculated powder surface temperatures and powder/slag levels are validated with plant measurements [32, 33] conducted in previous work by CCC researchers (Adnan Akhtar, Matt Zappulla) and CCC sponsor (Joydeep Sengupta) at Dofasco. Then, the sintering and densification physics is

implemented into the model to account for the contraction of pore spaces resulting in powder compaction, and shrinkage, which enhances the heat conduction through the powder/slag layers.

In the current study, granulated mold powders, and carbon in the form of graphite are investigated. The pore spaces are initially filled up with air which later gets mixed with the reacting gases. The model results for temperature and carbon distribution, powder shrinkage, and gaseous exhaust are validated with the lab sintering measurements available in the literature [12]. Then, the multi-reaction complete combustion model with the transport, and sintering physics is implemented to predict the temperature, powder/slag levels, pore fraction, carbon and gas distribution in a real continuous caster. To our best knowledge, no comprehensive computational model/experiment exists in literature to predict the heat transfer, mass transfer, gas reactions, exhaust gas composition, and combustion of mold powders in an actual caster.

1.4 Dissertation Outline

This dissertation is divided into 8 chapters.

Chapter 2 contains a literature review of computational models of top surface powder and slag layer behavior, and previous experiments to predict/measure the temperature distribution, density variation, carbon combustion, gas transport, and powder melting rate in those layers. This review aims to gain a comprehensive understanding of advances in mold powder studies whether in the form of lab experiments, or empirical/computational models probing to study one or multiple aspects of mold powder behavior during heating, phase transition, melting, and carbon burning.

Chapter 3 introduces the steady-state heat transfer model and verifies it with analytical solution and ANSYS Fluent for constant powder/slag properties, and with Fluent for temperature-dependent properties.

Chapter 4 introduces the transient heat and mass transfer model, along with the interface balance model which calculates the location of phase boundaries changing due to powder addition, liquid flux consumption, and powder melting. The transient model is verified with ANSYS Fluent.

Chapter 5 introduces the multiphysics model with the sintering and combustion behavior of mold powders. It describes the sintering kinetics of granulated mold powders and model validation with lab measurements. The density-temperature relationship is studied taking into account the effect of time, and sintering rate constants. It also explains the carbon combustion physics and gas transport through the powder bed, and validation with lab measurements. The combustion model in this chapter builds on the heat transfer, and mass transfer model described in Chapter 4, and uses the thermal profile to predict the densification, carbon and gas distribution through the powder layer, and the gaseous exhaust from the top of the powder layer.

Chapter 6 contains the transient thermal model application to the commercial steel continuous casting process. First, the heat and mass transfer model is used to predict the powder top surface temperature and the powder/liquid flux levels. The model predictions are validated with plant measurements in commercial operations, including specifically, the thick-slab caster at Dofasco and the thick-slab caster at Tata Steel. The model is found to capture the physics well and predict the temperature and powder levels for both scenarios which agree with plant measurements.

Parametric studies are conducted to understand the effect of parameters such as powder packing, slag consumption, and carbon burning (a preliminary study that accounts for carbon burning through an effective specific heat of the mold powder). Following the parametric studies, various powder-feeding mechanisms prevalent in the plant like manual powder feeding (through an intermittent powder addition by a plant operator), and automated feeding (through a robot, or well-designed control system) are explored.

Chapter 7 presents the multiphysics model application to continuous caster. It considers the sintering physics, and carbon combustion, diffusion, and gas transport behavior to predict the density profile, and carbon and gas distribution. The model properties with the sintering phenomena are more complex than the piece-wise linear properties used in the first study of the continuous caster. So, the model needs to be re-validated with the plant measurements. Among the measurement cases available, the best case with an ultra-low carbon steel slag is used to re-validate the surface temperature and powder/slag levels in a commercial caster.

Chapter 8 summarizes the research conclusions and future work for the model. The future work section describes the new physics that is relevant to studying the mold powder behavior and can be explored in a future version of the model.

Appendix A presents the nomenclature for the various symbols, and variables mentioned in the dissertation document.

Appendix B mentions the copyright permissions for the external figures included in this work.

CHAPTER 2
LITERATURE REVIEW

This chapter reviews the previous work done by researchers on the modeling of continuous casting mold powders focusing on these areas: Heat transfer and fluid flow, powder consumption, sintering, combustion, gas transport, powder melting, and additional multi-physics.

2.1 Heat Transfer, and Fluid Flow

Several studies exist in the literature to study horizontal heat transfer across the gap between the solidifying steel and the copper continuous casting mold. However, only a few models are available in the literature that studied the vertical heat transfer through the powder/slag layers on the top surface above the molten steel in the mold. McDavid et al.[34] developed a 3-D, steady-state, finite element-based model using the commercial code, FIDAP to study the combined effect of heat transfer, and fluid flow inside the top-surface flux layers in steel continuous casting. Akhtar et. al. [32, 33] conducted measurements of powder levels, and powder surface temperatures using nail dipping tests in the plant. Akhtar also developed a 2-D, computational model in ANSYS Fluent to calculate the temperature distribution through the nail in a nail-dipping experiment, and compared them with the measurements. Nakano et. al. [35] also developed a finite difference-based model to predict the temperature distribution through the powder considering the powder consumption in the form of liquid flux removal rate from the domain bottom.

A study of radiation heat transfer through mold fluxes[36] found that the absorption and extinction coefficients do not have any appreciable change with temperature below 773K. A gray gas assumption was utilized in the model to calculate the radiation heat flux. The radiative conductivity was found to be larger for low carbon and ultra low carbon steel as compared to medium carbon steel. This was attributed to different solidification patterns and higher melting rates rather than to the optical properties of slags with lower carbon content.

Bin Zhao conducted 2-D numerical simulations to quantify the effect of coupled heat transfer, and fluid flow on heat transfer in a thin molten flux layer above molten steel using commercial code, ANSYS Fluent [37]. The effect of natural convection in the flux layer, along with bottom shear velocity, and effect of temperature dependent viscosity was studied. The contours of density gradient in the convection cells constructed from the temperature gradient are matched with the fringes from the experimental interferograms (Figure 2.1). Natural convection was found to be suppressed for thin flux layers, when the transverse flow of molten steel below the surface is sufficient, which usually occurs in commercial casters, so

the Nusselt number was found to increase linearly with bottom shear velocity.

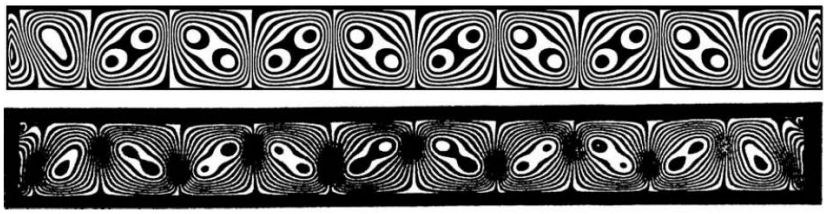

Figure 2.1 Comparison of computed and measured flow patterns in a thin molten slag layer with natural convection cells showing (top) Horizontal density gradient contours from 2-D computational simulation (Case 1A) [37]; (bottom) Interferograms from the experiment showing fringes from temperature-dependent density [38]

The variation of the heat transfer, represented through a Nusselt number (Nu) with the molten steel velocity is shown in Figure 2.2. This parameter (Nu) represents an increase in thermal conductivity of the molten slag layer due to enhanced convection due to mixing because of fluid flow (mixing augmented conduction). It is observed that Nusselt number increases near linearly with bottom shear velocity. A higher Nusselt number, and hence higher molten slag thermal conductivity is observed for slag (b) which has a smaller viscosity than slag (a). This occurs because the end effects get extended with higher flow circulation in the flux layer. The extent to which Nu increases depends on the flux viscosity. The results for slags (b) and (c) match, even though the properties are different, because the dimensionless numbers, Rayleigh number(Ra) and Prandtl (Pr), match, which depend on slag properties (density, molecular viscosity, and thermal diffusivity), showing that those parameters control the Nusselt number (Nu).

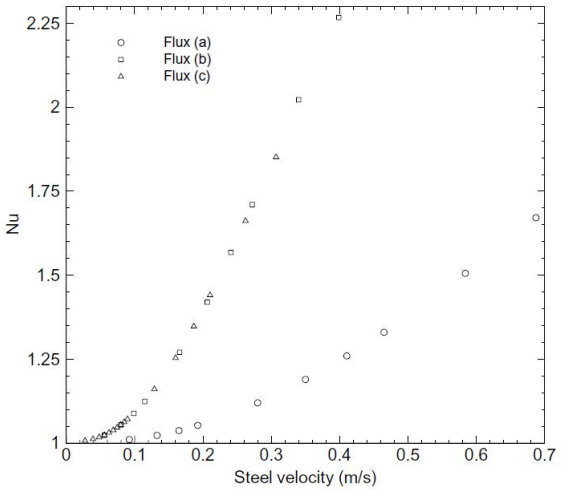

Figure 2.2 Variation of Nusselt number due to convection heat transfer through the molten slag with molten steel velocity beneath the slag layer for two different slags [37]

2.2 Powder consumption

Previous researchers have conducted studies to evaluate the effect of the physical and chemical properties of mold slags, and casting conditions on powder consumption. An empirical criterion developed by Wolf [39] gives an optimum molten slag viscosity for having the least amount of mold friction at a particular casting speed. He also evaluated a target molten flux consumption rate[40] so that the caster can operate in a stable manner without leading to breakouts. Several other empirical equations exist in the literature which estimate the mold powder consumption based on mold oscillation, and mold flux crystallization temperature[41, 42].

The powder consumption model used in this dissertation is a semi-empirical model based on extensive plant trials conducted on continuously cast ultra-low carbon steel slabs [43]. Flux is consumed into the gap between the solidifying steel and the mold walls via 3 components: a slow-moving re-solidified or crystallized layer against the mold wall, a liquid layer, and by flux trapped in the oscillation marks. Flux consumed due to lubrication is estimated by subtracting the flux contained in the oscillation marks (OM) from the total measured consumption. So, the flux consumed due to lubrication of the interfacial gap between the mold wall, and solidifying steel strand is the major consumption source at higher casting speed, while the slag that flows into the gap and gets trapped in the oscillation marks is the dominant mass sink for slag at lower casting speeds. If the liquid flux lubrication layer is too thin, this can result in higher friction, and the formation of transverse cracks, and when it is non-uniform around the strand perimeter, it can lead to stress concentration and longitudinal cracks and breakouts.

2.3 Sintering

Granulated powders have a high porosity ($\geq$70%) at room temperature. As the powder heats up, the particles become more closely packed, and the total porosity decreases. The total porosity is the sum of internal pores inside each hollow particle, and external pores (which define the packing factor) in between the particles. So, the particle density increases with both higher temperatures and longer times. Sintering refers to the complicated phenomena of partial melting, sticking together of the particles, and densification. Sintering rate kinetics has been studied by several researchers [12, 44–46].

In the 1960s and 1970s, the fundamental physics of sintering was developed. Thummler et. al performed a detailed literature review of the sintering process explaining the various transport mechanisms during the sintering process as pore spaces decrease, and neck formation occurs resulting in the cohesion of powder particles [44]. He proposed the exponential Arrhenius relation as governing the sintering process.

$$k_s = [k_0 exp^{-\frac{Q}{RT}}]^n \tag{2.1}$$

where: n: exponent, Q: activation energy, k_s: rate constant of sintering, T: Temperature,

The sintering rate depends greatly on the form of the carbon, (free carbon - graphite chunks, vs fines vs combined chemically as carbon compounds) and the form of the powder (fines vs granulated)[11]. An isothermal sintering study of uranium oxide in an optical dilatometer exists in literature [45]. The uranium oxide compacts sintered had constant non-stoichiometry and the oxygen partial pressure was measured by a stabilized zirconia solid electrolyte cell. The sintering kinetics was studied, and an empirical densification rate equation was developed which was valid for a temperature range of 1000-1550 ° C. The temperature effect on sintering agreed with previous literature. They fit their measurements to the following rate equation:

$$\frac{V_0 - V_{th}}{V_s - V_{th}} = e^{k_s t^n} \tag{2.2}$$

where, V_0: volume at unsintered conditions, V_{th}: volume at theoretical fully sintered conditions, V_s: volume at sintered condition, n: exponent, Q: activation energy, k_s: rate constant defined in the previous equation

In another work [46], the uniformity in mold flux composition of spray granulated fluxes, and its effect on properties during heating was studied through experimental techniques like TG-DSC, XRD, SEM-EDS, and sintering measurements. It was found that during the granulation process, Na and C enrichment took place on the powder particle surface due to different outward diffusion of the various raw materials used during sintering.

Since then, the above method has been applied to different materials, and compounds similar to mold powders such as Calcium Carbonate ($CaCO_3$) [47–52]. A well-known classical model in literature, the german-Munir model [53] calculates the surface area decrease during early, and intermediate stages of sintering. In work by Maya et. al [50], the effect of surface diffusion, and grain boundary diffusion were studied in a mathematical model of CO_2 catalyzed CaO sintering.

2.4 Combustion and Gas Transport

The carbon in the casting powder undergoes combustion through several reactions[12, 13, 54] leading to the formation of carbon dioxide and carbon monoxide. These reactions are controlled by both chemical kinetics and diffusion due to the transport of oxygen into the powder and the transport of combustion products out of the powder layers.

Isothermal lab experiments have been carried out in the literature to investigate the carbon combustion of mold powders [13]. In the work by Schwerdtferger et. al., large samples were combusted with oxygen by keeping them at a constant temperature. Different regimes were found governing the kinetics of carbon

combustion. The chemical reaction involving the oxidation of carbon to form carbon dioxide has a dominant effect at low temperatures (300-400 °C), while at higher temperatures (600-800 °C), the mass transfer within the powder layers, and in gaseous space above the powder is important for carbon combustion in the powder[13]. A region of mixed control is described to be present in between these temperatures[13]. The top powder zone being at low temperatures does not favor the combustion reactions to occur. In the real casting process, temperature gradients exist within the powder which need to be taken into account, and it is important to understand the combustion behavior in mold powders[12].

Another lab-scale study in the literature by Supradist et. al. investigated the carbon combustion behavior under a temperature gradient, by heating as-received powder along with added graphite for two hours[12]. At the end of the experiment, the density and carbon distribution through the powder layers are measured after cooling the powder to room temperature. A strong variation of carbon distribution was found with the original carbon content remaining intact at the powder top, a minimum carbon content in the powder interior close to halfway through the powder column, and another minimum residual carbon towards the powder bottom. The density measurements showed a clear trend of the powder packing being stronger at higher temperatures. However, up to $\sim$ 400 ° C, there was no change in density even though the powder temperature was above the ambient temperature. The density profile for the powder including graphite was reported to be lower than the mold powder received from the plant. As a result of sintering, and densification, the resulting powder thickness was found to be shorter than the initial level. Along with measuring the powder height, the off-gas released at the powder top surface was also monitored. A computational model was developed to simulate the lab measurements [12].

2.5 Powder Melting

A heat transfer model developed by Delhalle et. al. [55] explores the temperature distribution through the powder/slag layers. The calculated temperature isotherms are shown in Figure 2.3. The molten slag layer thickness increases with a lower powder melting temperature and higher thermal conductivity[56, 57]. As long as the surface temperature is below 800 °C, the molten flux level doesn't change with powder thickness. If operators at the plant exercise caution to avoid the "red spots" by adding powder intermittently, then the amount of powder added, or the addition frequency is not expected to affect the important process parameters [55].

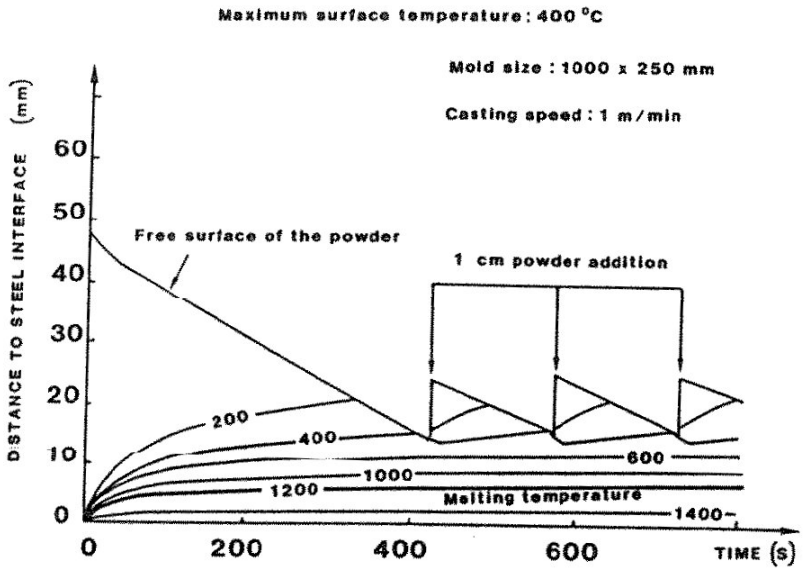

Figure 2.3 Temperature isotherms [55]

At a given powder melting temperature, the molten flux layer thickness decreases with higher flux consumption velocity. But higher casting speed can also enhance the convection in the molten pool, and melt more powder, resulting in a compensatory effect[55]. Powder melting rate depends on the melting temperature, and flux consumption rate, and cannot be classified as an inherent powder property, but rather a result of process conditions[55]. It is the residual of the powder addition rate, and molten flux consumption rate, and can vary during the casting process, as temperature, sintering behavior, and carbon combustion evolves.

During sintering, mold powder particles sinter to form a dense cohesive mass, and the liquid droplets gradually filter down to contribute to the liquid slag pool beneath the powder layers. It is important to maintain sufficient molten flux thickness to provide adequate feeding of liquid slag to be consumed to serve as lubrication of the gap between the solidifying strand and copper mold to avoid the sticking of the strand which can lead to breakouts. It is known that carbon decreases the melting rate[14, 31, 58–62] of powder by separating the powder particles and slowing down the rate of sintering. Several models in literature[11, 21, 54] predict the molten flux thickness for different C contents (See Figure 2.4). The caster was not run for the other case[11], as too small slag depth might result in insufficient lubrication, leading to breakouts. It is seen that higher carbon contents result in a thinner liquid flux layer[11]. The Nakano model matches the measured plant values for 1% C and 2% carbon cases.

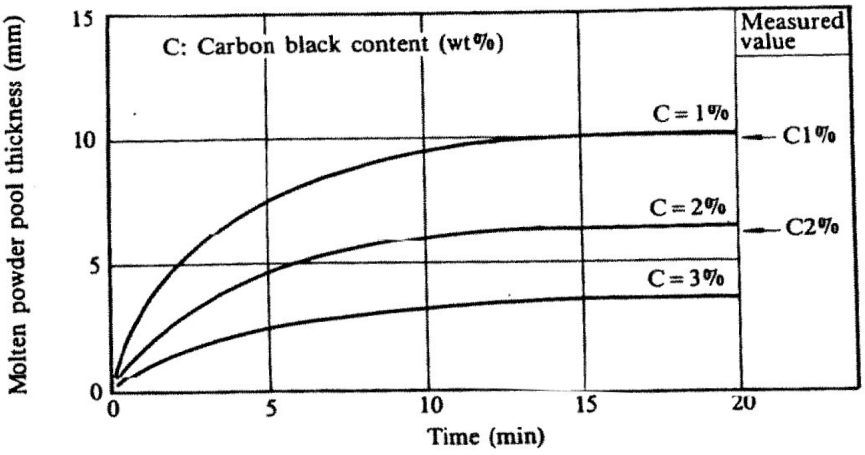

Figure 2.4 Predicted and measured molten flux thickness for different carbon contents [11]

Another study by Bin Xie et. al [21] observed the effect of different types of carbonaceous materials on the powder melting rate. Carbon has been found to affect both the powder sintering and melting rates [11, 21]. It was found that the higher the carbon content, and the dispersivity of the carbon, the lower the powder melting rate (Figure 2.5). Carbon black was found to have a more pronounced effect on the powder fusing rate than graphite.

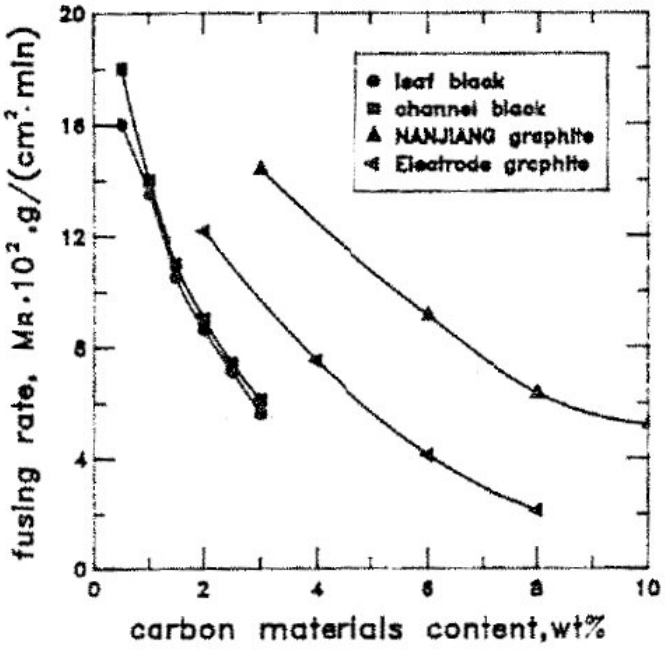

Figure 2.5 Effect of different types of carbon on powder melting rate [21]

In very recent work by Chen et. al [30, 54], it has been found that upon increasing the powder thickness, the powder melting rate has been observed to follow an 'M-curve'.

2.6 High-speed thin slab casting

A lot of work has been done to study mold powder performance for high-speed casting [61, 63–67]. For high-speed casting (with speeds up to 6 m/min), adequate powder melting is essential to provide necessary lubrication between the strand, and the mold, and for proper control of heat transfer across the gap. In comparison to standard slab casting, lower slag viscosity, higher solidification temperature, and basicity are characteristics of mold powders for thin slab casting.

2.7 Additional Phenomena

The effect of the structure of silicate slags on the thermal expansion, viscosity, electrical, and thermal conductivity has been studied by Mills [68]. The depolymerization of the melt is the most important factor in influencing most of the physical properties of the slag, including its thermal conductivity and especially its viscosity.

Matsushita et. al [69] measured the density of mold flux slags using sessile drop and Electrostatic Levitation method. In addition to the powder composition and properties, mold flux performance [70] is primarily affected by several factors (i) casting conditions (casting speed, oscillation frequency, stroke, etc.) (ii) steel grade and the dimensions of the mold (iii) fluctuations in mold level (iv) turbulent flow of molten metal which can result in slag and particle entrapment. For a given set of casting conditions, mold dimensions, and steel grade, three properties were reported[70] to ensure optimal lubrication and heat transfer, which are (i) viscosity (ii) break temperature, and (iii) degree of crystallinity in the slag. These properties affect fluid flow, crystallization also affects thermal conditions.

Carbon pick-up by molten steel is a major concern for ultra-low carbon (3-6 ppm [71]), and low carbon steel due to high carbon content in the powder/slag[72] (especially in the sinter layer), or due to molten steel coming in contact with the powder during level fluctuations or insufficient liquid slag levels. Increasing liquid flux level thickness makes it difficult to control due to higher slag overflow into the gap. Studies on steel decarburization are essential to minimize the detrimental effects of carbon on steel contamination. LeFebvre et. al [71] conducted experiments in which they replaced free carbon with SiC and Si_3N_4 and observed their powder melting characteristics, liquid flux depth, powder consumption, and refractory wear of the SEN nozzle, and metal-slag interaction. Test product with 0.6% free carbon and 0.35% of Si_3N_4 showed similar powder behavior, with a 5 ppm reduction in carbon uptake, and no extra increased uptake of Si and N.

Another study[73] investigates the effect of basicity index on the alumina absorption of molten powder. The work reports that $A1_2O_3$ content in the liquid flux formed due to powder melting increases with the time after casting begins according to the $A1_2O_3$ absorption capacity of the powder, but after some time, reaches a constant value that matches the alumina absorption capacity of the powder[73]. The oxide absorption rate of the molten powder is found to be proportional to the basicity index of the powder. The molten flux viscosity is also reported to increase with increasing $A1_2O_3$ content (Figure 2.6).

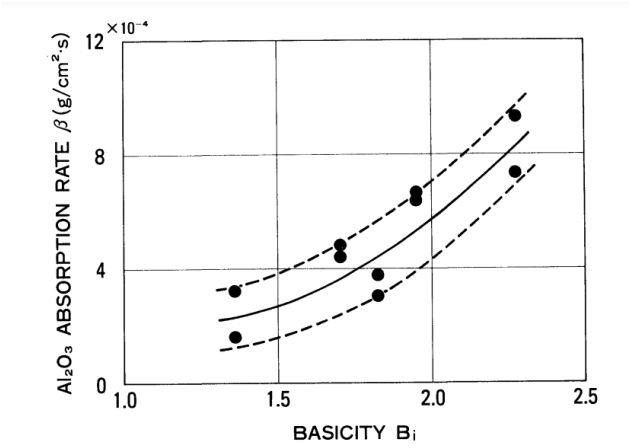

Figure 2.6 Correlation between alumina absorption of molten powder and basicity [73]

There are several environmental concerns about using mold powders containing calcium fluoride, as the fluorine gas released into the atmosphere can be detrimental to the safety of plant workers, cause corrosion of plant equipment, and leach from landfill areas into the groundwater. Several attempts have been made to produce fluorine-free mold powders [74, 75]. Industrial trials[76] showed that using fluorine-free fluxes led to a reduction in SEN erosion rates, and prominent decreases in F^{-1} in the cooling water in the scaling pit, without any decrease in surface quality, and mold behavior.

CHAPTER 3

OVERVIEW OF MODELS AND STEADY-STATE MODEL

The multiphysics model has been built in several steps. First, a steady state model in-house code was developed in MATLAB to solve the energy balance through the powder/slag layers using the fsolve simultaneous equation solver in Matlab [77]. This was followed by the development of a transient heat and mass transfer model with interface movement. Next, the sintering kinetics was implemented into the transient thermal model to account for the shrinkage of pore spaces in the powder. Then finally, the carbon and gas transport model was implemented to result in the advanced multiphysics model.

3.1 Steady State Heat Transfer

This section contains the details of the steady-state model and its verification with analytical solution and Ansys Fluent. A schematic of the slag layers showing the general model domain, along with an optical micrograph of the powder, and the model grid are shown in Figure 3.1. Several different fluxes occur in the process, namely, (a) heat flux (predominantly in the upward direction) (b) powder/slag mass flux (in the downward direction), and (c) gaseous species flux (predominantly in the upward direction).

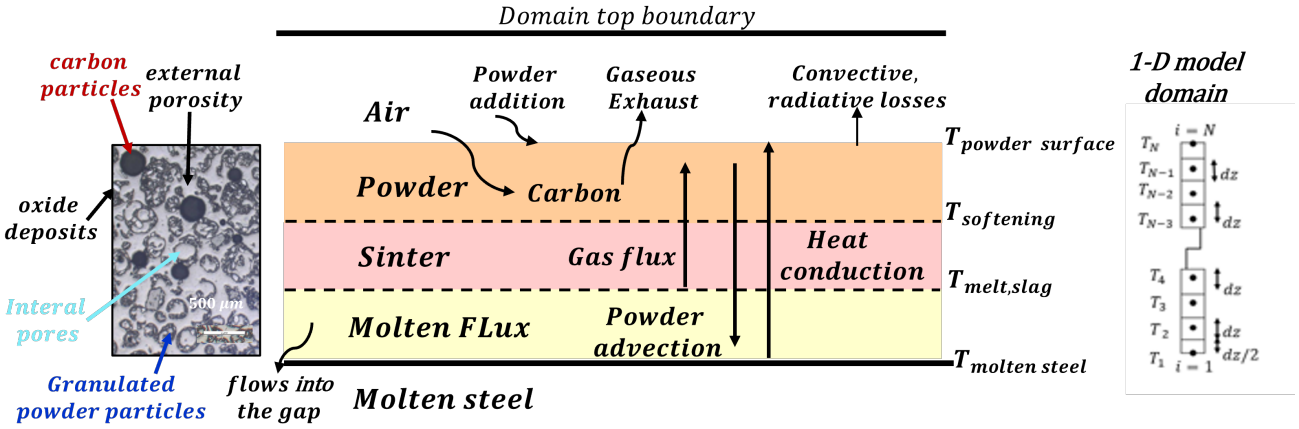

Figure 3.1 Closeup of powder/slag layers showing (a) Optical micrograph of mold powder structure [78] (b) Model domain (c) Corresponding grid of computational cells.

The 1-D vertical domain (Figure 3.1) represents the layers of liquid flux, powder/sinter, and some air (gravity is negative z-direction-towards the molten steel in the domain). The figure shows the different phases in the mold powder/slag, namely, (loose) powder, (dense) sinter, and molten flux layers. The molten flux layer is present only in a commercial caster, and not in lab experiments on powder sintering.

Heat and mass flow are considered in the vertical direction z, where z=0 represents the molten flux-liquid steel interface. The powder/slag region (Figure 3.1) is modeled from the top of the molten steel interface with the liquid slag to the top of the powder layer and some of the air above (which takes away heat to the environment, and supplies oxygen). The different phase transition temperatures are shown in the figure. Air is present at the top of the domain, which gets replaced with cold powder during powder additions.

The top of the top cell in the computational domain (as well as other cells in the region above the loose powder) is comprised of air and is set to an ambient temperature of 300K (domain top boundary). The bottom of the bottom cell at z = 0 in the domain represents the interface between the top surface of the molten steel and the bottom of the liquid slag layer (domain bottom boundary). This bottom boundary is fixed at the local temperature of the molten steel. The number and size of the cells in the domain are fixed. Cell indices increase from the domain bottom as we move up toward the powder top surface.

Heat supplied from the molten steel is conducted upwards through these various layers. Heat is also advected downwards due to the powder shrinkage and liquid flux removal from the bottom (liquid slag layer) due to consumption. Heat leaves the powder top surface (powder-air interface) due to convection and radiation. Thermal properties, including thermal conductivity, specific heat, and density, are temperature, and phase-dependent, and increase towards the bottom of the domain (as we move from the powder towards the molten flux).

It takes into account the heat conduction from the hot molten steel upwards through the powder/slag layers, and heat advection due to liquid flux consumption from the powder surface downward towards the powder/slag bottom. The governing equation for steady-state energy balance is as follows:

$$\rho c_p v_{cons,f} \frac{\partial T}{\partial z} + k \frac{\partial^2 T}{\partial z^2} + \frac{\partial k}{\partial T} \left(\frac{\partial T}{\partial z}\right)^2 = 0 \tag{3.1}$$

ρ: density, c_p: specific heat, $v_{cons,f}$: flux consumption velocity, T: Temperature, k: thermal conductivity, z: vertical direction

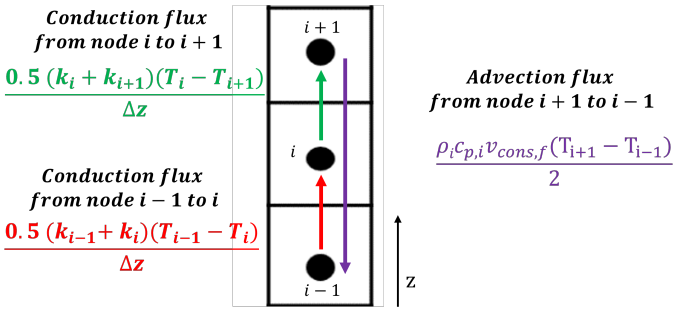

Figure 3.2 Steady state model- Thermal fluxes

In Figure 3.2, an internal cell along with its neighbors are shown. The nodes are lined up such that the bottommost node at the liquid flux- molten steel interface is indexed as 1, and the top most powder node (corresponding to the powder-air interface) is indexed as N. as shown, heat conduction occurs from node i-1 to i and i to i+1 based on the thermal gradient, and the thermal advection occurs in the opposite direction due to powder movement as it is pulled downwards in the vertical $-z$ direction (in this picture from top to bottom) due to flux consumption velocity, and powder shrinkage velocity.

In the steady-state model, only the effect of flux consumption on downward advection velocity in the powder was considered. Powder shrinkage was ignored in this simple model while calculating the steady-state temperature distribution through the powder/slag layers. This effect is later included in the multiphysics model by implementing the sintering kinetics. The flux balances are solved using a non-linear equation solver, fsolve in MATLAB. The bottom node is at the melting temperature of molten steel ($1823K$) and an effective heat transfer takes place at the powder top surface due to convection, and radiation (correlation for heat convection, and radiation are described in transient model boundary condition section 4.2.1 in Chapter 4).

A flowchart of the solution methodology of the steady-state model is shown in Figure 3.3. The fluxes are calculated based on the property models, and an initial guess for the temperature field, and the solver iterates to minimize the residuals based on a set tolerance (allowable error of 10^{-9}) and outputs a temperature distribution after convergence.

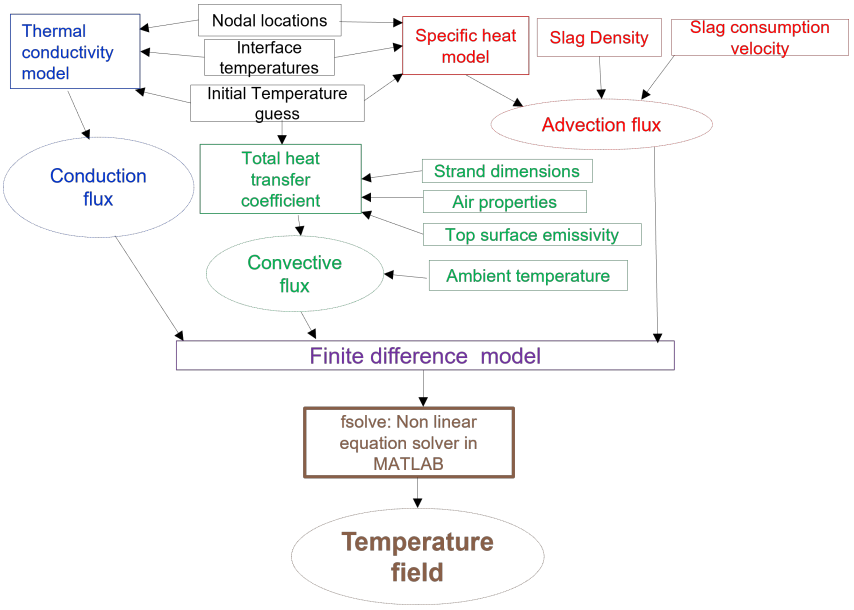

Figure 3.3 Steady state model flowchart

The steady-state model is run for a High Strength Low Alloy (HSLA) Steel slag case with input parameters given in Table 3.1. First, a grid independence study is conducted to determine an optimal cell size that can be used to get a reasonable solution. The case solves the 1D, Steady-state, conduction heat transfer with advection (implemented through a downward powder/slag velocity) and convective heat transfer at the top surface. Constant thermal properties for Thermal conductivity (k), and Total heat transfer coefficient (h_{tot}), density (ρ), Specific heat (c_p) are used in order to facilitate model verification.

Table 3.1 Model Parameters

Properties and Boundary conditions	HSLA slag
Total powder/ slag thickness, w_{tot}	55 mm
Casting speed, v_c	1.4 m/min
Convection coefficient (top surface), h_{tot}	2.1 W/m^2K
Ambient Temperature (domain top), T_{amb}	300 K
Steel temperature (bottom boundary fixed temp), $T_{melt,steel}$	1823 K
Density, ρ	$2600k/m^3$
Empirical constant, k_e	17.8
Advection (consumption) velocity, v_{cons}	0.0243 mm/s
Thermal conductivity, k	1.5 $W/m-K$
Specific heat, c_p	2982 $J/kg-K$
Powder softening temperature, T_{sof}	$1300K$
Sinter mid region temperature, $T_{sinter,mid}$	$1350K$
Slag melting temperature, $T_{melt,slag}$	$1400K$

Slag consumption has an important effect on the resulting heat and mass transfer through the powder/slag. The advection/flux consumption velocity is calculated using an empirical model by Shin et. al.[43], and using the flux properties and casting conditions from Akhtar et. al [32] given in Table 3.1. The equations for the calculation of consumption velocity, v_{cons} are given below [43]:

$$q_{OM} = 2.5 * 10^{-2} \rho_{slag} k_e^{1.43} t_n^{0.389} v_s^{-1.49} (\sqrt{\frac{2\Delta\gamma}{\Delta\rho g}})^{0.556} \tag{3.2}$$

$$q_{lub} = 0.507 e^{3.59 t_p} \tag{3.3}$$

$$t_n = \frac{1}{\pi f} \cos^{-1}(\frac{v_s}{\pi s f}) \tag{3.4}$$

$$t_{cycle} = 1/f \tag{3.5}$$

$$t_p = t_{cycle} - t_n \tag{3.6}$$

$$q_{tot} = q_{lub} + q_{OM} \tag{3.7}$$

$$q_{area} = q_{tot} * \frac{f}{v_s} \tag{3.8}$$

$$q_{tot_1} = q_{tot} * f \tag{3.9}$$

$$q_m = q_{tot_1} * 2(th_{strand} * W_{strand}) * 0.001 \tag{3.10}$$

$$v_{cons} = \frac{q_m}{\rho_{slag} th_{strand} W_{strand}} * 1000 \tag{3.11}$$

where: q_{OM}: oscillation mark consumption per cycle [g/m cycle], q_{lub}: lubrication consumption per cycle [g/m cycle], k_e: empirical constant that varies with the powder, t_n: negative trip time [s], v_s: casting speed [mm/s], $\Delta\gamma$: surface tension difference between liquid slag and steel [N/m], $\Delta\rho$: density difference between liquid slag and molten steel [kg/m^3], t_p: positive strip time [s], f: oscillation frequency [cycles/s], s: oscillation stroke [mm], t_{cycle}: total period of an oscillation cycle [s], q_{tot}: total consumption per cycle [g/m cycle], q_{tot_1}: total flux consumption per unit length [g/ms], q_m: flux consumption per unit time [kg/s], v_{cons}: consumption velocity [mm/s], W_{strand}: width of strand [m], th_{strand}: thickness of strand [m], q_{area}: flux consumption per unit area [kg/m^2].

Figure 3.4 shows classic convergence where the difference between the 550 cells and 1600 cells solutions based on the maximum difference between the temperature drops is 0.25% which is about 3°C error. A similar study was carried out for Fluent, and the maximum difference between the MATLAB and Fluent solutions for 550 cells to 1600 cells is 0.36%. Based on these results, 0.1mm is found to be an acceptable cell size for both efficiency and accuracy and is used for subsequent runs (0.1 mm = 550 nodes for a total powder/slag thickness of 55mm).

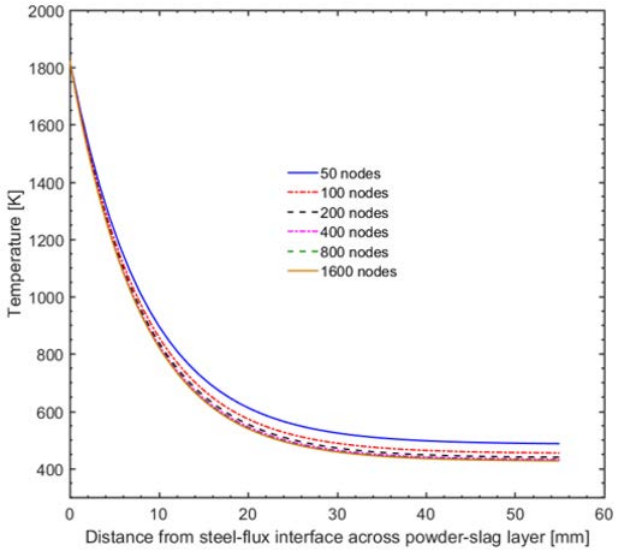

Figure 3.4 Grid independence study for the steady state model of temperature distribution through HSLA slag with constant properties

The steady-state model needs to be verified before the transient model can be developed to accurately predict the thermal profile through the powder/slag layers. An analytical solution is developed for steady-state heat transfer with liquid flux advection, and constant powder properties, and then the steady-state model is verified with both the analytical solution and an ANSYS Fluent model for constant properties and also verified with an ANSYS Fluent model for temperature-dependent properties.

The mesh used for ANSYS Fluent run is shown in Figure 3.5, and the thermal properties used in the run are shown in Figure 3.6 (a) and (b). The mesh was made by Adnan Akhtar [32], and includes a nail in the domain for investigating the use of nail oxide colors, which depend on nail temperatures, as a tool to measure the slag depth. In this work, only results on the far left boundary are compared so that the effect of the nail is negligible.

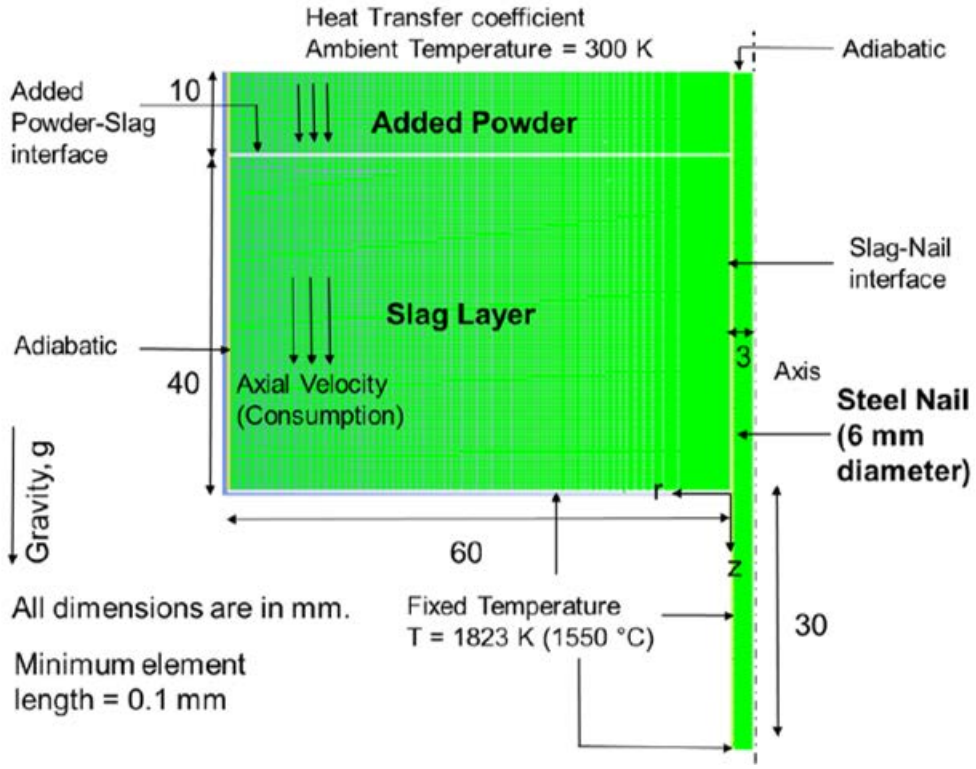

Figure 3.5 Fluent Mesh [32]

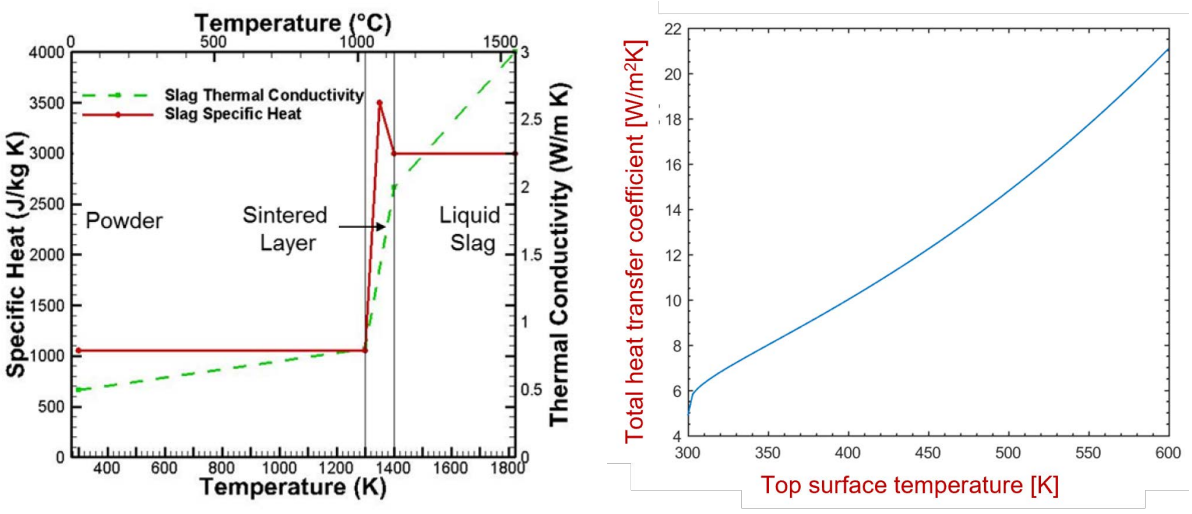

Figure 3.6 (a) HSLA steel slag properties for temperature-dependent case simulation [32] (b) Heat transfer coefficient

To verify the accuracy of the steady-state model, it was compared with results from a classic analytical solution. The analytical solution based on balancing is presented below:

Rate of Conduction heat transfer unit (W/m^3) = Rate of Advection heat transfer per unit volume (W/m^3) as follows:

$$-\rho c_p v_{cons,f} \frac{\partial T}{\partial z} = k \frac{\partial^2 T}{\partial z^2} \tag{3.12}$$

$$T = c_1 e^{\frac{-\rho c_p v_{cons,f} z}{k}} + c_2 \tag{3.13}$$

Boundary conditions are:

$$T = T_{melt,steel} \quad \text{(molten steel-slag interface at z=0)} \tag{3.14}$$

Conduction heat flux reaching the top surface = Convection heat flux leaving the top surface

$$-k \frac{\partial T}{\partial z} = h_{tot}(T_s - T_{amb}) \quad \text{(powder top surface at z=}z_{tot}\text{)} \tag{3.15}$$

Solving for the integration constants using the boundary conditions:

$$c_1 = \frac{h_{tot}(T_{amb} - T_{melt,steel})}{h_{tot}(e^{\frac{-\rho c_p v_{cons,f} w_{tot}}{k}} - 1) - \rho c_p v_{cons,f} e^{\frac{-\rho c_p v_{cons,f} w_{tot}}{k}}} \tag{3.16}$$

$$c_2 = T_{melt,steel} - \frac{h_{tot}(T_{amb} - T_{melt,steel})}{h_{tot}(e^{\frac{-\rho c_p v_{cons,f} w_{tot}}{k}} - 1) - \rho c_p v_{cons,f} e^{\frac{-\rho c_p v_{cons,f} w_{tot}}{k}}} \tag{3.17}$$

where: ρ: density $[kg/m^3]$, c_p: specific heat $[J/kg-K]$, $v_{cons,f}$: liquid flux consumption velocity $[m/s]$, T: Temperature [K], z: grid location [m], k: Thermal conductivity $[W/m-K]$, c_1, c_2: integration

constants $[K]$, h_{tot}: heat transfer coefficent at powder top surface $[W/m^2K]$, T_{amb}: Ambient Temperature $[K]$, $T_{melt,steel}$: molten steel temperature $[K]$, w_{tot}: total powder/slag thickness $[m]$

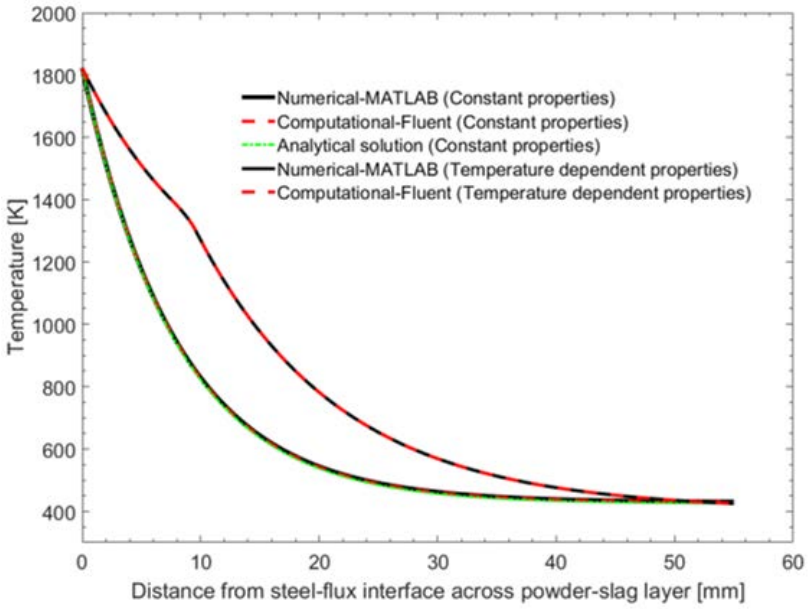

Figure 3.7 Steady state Model verification with Analytical solution and Fluent

The model shows a good match with both the analytical solution, and Fluent w.r.t. to the temperature profile (Figure 3.7), and heat fluxes at the powder/slag top and bottom surface (Table 3.2 below).

Table 3.2 Model verification with ANSYS Fluent

Heat Flux	MATLAB	Fluent
Top surface: Convection, q_{conv}	-1,382 W/m^2	-1,382 W/m^2
Steel-Molten Flux interface: Conduction, q_{cond}	-156,338 W/m^2	-156,319 W/m^2

The powder top surface convective heat flux was found to be $1.38kW/m^2$ (heat loss) for both the MATLAB and ANSYS Fluent models. The case was simulated in ANSYS Fluent to verify the accuracy of the steady-state model. Based on the heat flux calculated at the steel-molten flux interface with the current property model, an effective heat transfer coefficient of $h_{tot} = 103\ W/m^2K$ was applied as the top surface boundary condition of molten steel CFD simulations without having to simulate the slag layer. The model was found to be reasonably accurate and make reliable predictions of temperature distribution. This verified the steady-state model, and the model was used to validate the transient model.

CHAPTER 4

TRANSIENT THERMAL MODEL

4.1 Transient Heat Transfer model

A one-dimensional (1-D), finite-difference-based fixed-grid, transient heat transfer model has been developed in MATLAB, to compute the heat and mass transfer during transients in the process. The model domain represents a typical local region of the powder layer surface. For initial simulations, it is considered to represent an average powder/slag thickness to which an air layer is added, to handle the rises and drops in the powder level due to the combined actions of powder addition, powder shrinkage, and liquid flux consumption.

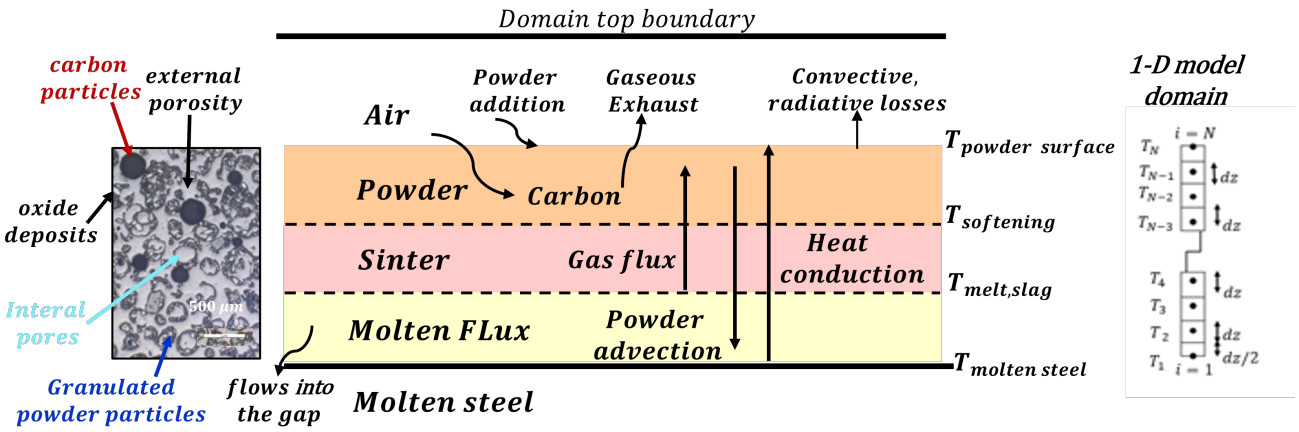

Figure 4.1 Closeup of powder/slag layers showing (a) Optical micrograph of mold powder structure [78] (b) Model domain (c) Corresponding grid of computational cells.

Liquid flux consumption can be quantified in several different ways. These different measures are equivalent and each of them determines the rate of powder usage, based on the strand dimensions, casting speed, mold oscillation frequency, and local density. Higher casting speeds result in greater powder consumption. The most common method is to average consumption over time, or the mold surface area, such as downward velocity through the various powder layers (mm/s), as shown in (Figure 4.1), consumption averaged over the external surface area (length and width directions) of the surface of the moving solidifying steel shell as it is withdrawn downwards at the casting speed (kg/m^2). Other methods include measuring the addition rate of powder to the top surface according to the bags added per hour (kg/hr.), or, consumption of the liquid slag into the interfacial gap per oscillation cycle (g/m-cycle). In this work, consumption is quantified by the downward velocity through the various powder layers (mm/s), as

shown in Figure 4.1.

The macroscopic interfaces or phase boundaries between the air and powder/sinter layers and between the powder/sinter and liquid flux layers, evolve with time according to heat flow and mass transfer between the cells in the domain. The phase of each cell can change with time due to the mass transfer associated with shrinkage of the powder column, powder addition at the top surface, and advection of powder down through the domain, according to the consumption.

4.2 Thermal submodel description

Heat transfer in the powder, sintering layer, and molten slag that comprise the system is modeled with the transient heat conduction equation, given in Eq. 4.1. The first term on the LHS represents the change in heat content due to transient behavior. Heat is conducted through the powder layers according to the last 2 terms in Eq 4.1, which are supplied from the molten steel (the last two terms in equation 4.1 are for conduction of heat through the powder layers from the molten steel below the domain to the top surface which is exposed to ambient air). Heat is advected due to the powder movement in the downward direction due to shrinkage (third term), and, also advected due to liquid flux removal from the bottom (second term). Heat loss occurs from the powder top surface (powder-air interface) due to convection, and radiation, given in the boundary condition (next) section. The change in temperature of the powder layer with time is given by the transient term, the first term in Eq. 4.1. Temperature-dependent property functions including thermal conductivity, specific heat, and density have higher values as we move from the top toward the liquid flux region at the bottom. The phase change due to heat transfer is handled through an enhanced effective specific heat profile (function of temperature) over the phase-change temperature region, which takes into account the latent heat released due to melting in the powder/slag layer. There is a steep jump in the specific heat during this phase transition. The energy released in the gas reactions is relatively negligible and therefore is ignored.

$$\rho c_p \frac{\partial T}{\partial t} = \rho c_p v_{cons,f} \frac{\partial T}{\partial z} + \rho c_p v_{shrink,p} \frac{\partial T}{\partial z} + k \frac{\partial^2 T}{\partial z^2} + \frac{\partial k}{\partial T} (\frac{\partial T}{\partial z})^2 \tag{4.1}$$

This equation is solved using explicit, central difference scheme for the time and spatial numerical discretization:

$$T_i{}^{r+1} = T_i{}^r + \Delta t^{r+1}(v_1+v_2)\frac{T_{i+1}{}^r - T_{i-1}{}^r}{2\Delta z} + \alpha^*(T_i{}^r)\frac{T_{i+1}{}^r - 2T_i^r + T_{i-1}{}^r}{\Delta z^2}\Delta t^{r+1} + \frac{\Delta t^{r+1}}{\rho^* c_p^*}\frac{\partial k}{\partial T}^{r+1}(\frac{T_{i+1}{}^r - T_{i-1}{}^r}{2\Delta z})^2 \tag{4.2}$$

where: r: previous time step, $r+1$: current time step, i: node number, $v_{shrink,p}$: powder shrinkage velocity, $v_{cons,f}$: flux consumption velocity, v_1: ${v_{cons,f}}^{r+1}$, v_2: ${v_{shrink,p}}^{r+1}$, T: Temperature, Δt: time step

size, Δz: grid spacing, α: thermal diffusivity, ρ: density, c_p: specific heat, k: thermal conductivity, $*$: adjusted properties after mass balance

4.3 Interface conditions

The Air-Powder interface (at the top surface between the air above the caster and the powder/sinter material layer) moves through the cells in the fixed grid based on the mass balance due to powder addition, shrinkage due to densification, and liquid flux consumption. After an immediate powder addition, an air cell can get designated as a powder cell (depending on the amount of powder added), while if there is enough shrinkage, or slag consumption (based on the velocities, and the time step size) in that time step such that the interface jumps 1 cell (it might even cross a cell over a few time-steps) down, then previously powder cell gets considered as an air cell now. For all air cells in the domain, an ambient temperature of $300K$ is assigned. All the thermal properties of the air cells also get updated to the air property values. Since, the phase of each cell can change with time based on the process transients, at every time step, the topmost cell containing powder is determined, and the Air-Powder interface boundary condition is applied to the moving interface.

$$-k\frac{\partial T}{\partial z} = h_{tot}(T_N - T_{amb}) \tag{4.3}$$

$$h_{tot} = h_{conv} + h_{rad}, h_{conv} = Nu\frac{k_{air}}{L_c}, h_{rad} = \sigma\epsilon(T_N^4 - T_{amb}^4), L_c = \frac{W_{strand} + th_{strand}}{2} \tag{4.4}$$

$$Nu = 0.14Ra^{0.33}, Ra = 2 * 10^7 - 3 * 10^{10} \quad (turbulent flow)$$

$$= 0.54\mathrm{Ra}^{0.25}, Ra = 10^5 - 2 * 10^7 \quad (laminar flow) \tag{4.5}$$

$$Ra = \frac{\rho_a g\beta\Delta T L^3}{\mu_a \alpha_a} \tag{4.6}$$

where, N: top-most node (powder surface), T_{amb}: Ambient temperature (300K), h_{tot}: Total heat transfer coefficient (W/m^2K), h_{conv}: Convective heat transfer coefficient (W/m^2K), h_{rad}: Effective radiative heat transfer coefficient (W/m^2K), Nu: Nusselt number, k_{air}: air conductivity [$W/m-K$], L_c: characteristic length [m], W_{strand}: strand width [m], th_{strand}: strand thickness [m], Ra: Rayleigh number, ρ_a: Air density, μ_a: Air viscosity, α_a: Air thermal diffusivity, g: acceleration due to gravity, β: thermal expansion coefficient, ΔT: temperature difference between surface and ambient.

In this process, the airflow above the mold is fully turbulent, with a typical Ra number of $1.65 * 10^9$. Thus, the turbulent flow condition is used to calculate the Nusselt number in equation 4.5.

The Powder-Liquid interface, at the bottom of the sinter layer and top of the molten flux layer, is given no special treatment. Thus, the cell containing this interface is subjected to conduction and advection

fluxes the same as all the internal cells. This greatly enhances the gas mixing in the region above the powder after exhaust gas evolution, as discussed in the next chapter.

4.4 Bottom boundary condition

Continuous caster case

$$T_1 = T_{melt,steel}(1823K), z = 0 \tag{4.7}$$

Lab sintering experiment case

$$-k\frac{\partial T_1}{\partial z} = h_1(T_1 - T_{furnace}), h_1 = 29,000W/m^2K, z = 0 \tag{4.8}$$

4.5 Mass Transfer submodel description

Mass transfer occurs vertically between the cells due to powder addition at the top surface (manual addition at special times, or continuous addition through an automatic feeder), combined with liquid flux consumption from the bottom (continuous), and powder shrinkage due to sintering and densification. Consequently, the total powder level, and the amount of powder/slag, carbon, and gaseous moles in all the cells change with time. In the model, after getting the initial temperature distribution (could be from results of a steady-state model, or could simulate from the start of the process after the powder is first added to the molten steel), mass balance takes place, following which the interface calculation takes place. The model is step-wise coupled, such that interface calculation (at the beginning of the time step), powder mass balance, interface calculation (as mass transfer is expected to move the interfaces around based on powder addition, liquid flux consumption, and powder shrinkage), energy balance, carbon, and gas calculations (to be discussed in the next chapter) occur within the same time step one after other, and since it is an explicit model and uses a small time step ($\sim 10^{-5}$s), all equations can be considered to be solved in a near-simultaneous manner.

$$\frac{\partial m_p}{\partial t} = \dot{m}_{add_p} - \dot{m}_{cons_f} - \dot{m}_{adv_p} \tag{4.9}$$

m_p: mass of powder/slag in cell, t: time, $\dot{m}_{add_p}$: rate of powder addition (occurring at the top surface), $\dot{m}_{cons_f}$: rate of liquid flux consumption (in the molten slag layer at the domain bottom), $\dot{m}_{adv_p}$: rate of powder advection due to shrinkage due to powder sintering and densification.

Powder addition may be continuous (a constant non-zero powder addition rate), or intermittent (high powder addition rate at special times). The amount of powder added, or consumed as liquid flux translates to an effective change in the powder/slag height which is predicted by the interface balance model. (please note: Liquid flux and Liquid Slag essentially refer to the molten powder, and are interchangeably used in the thesis)

4.6 Interface balance submodel description

4.6.1 Phase boundaries after Energy balance

The Powder-Liquid flux interface, between the bottom of the sinter layer and the top of the liquid slag layer, is calculated based on the fixed transition temperature (∼1400K) after the energy balance by linear interpolation between the nodal locations and temperatures. The Air-Powder interface remains at the same location after mass balance in the same time step during the energy balance (since the powder top surface might get hotter, but will not undergo any phase transition as its temperatures are too low due to being exposed to the ambient). The domain top (the interface between the ambient surroundings and the air layer) and the domain bottom (the interface between the liquid flux and the molten steel) remain fixed throughout the simulation.

$$w_{final,1}^{r+1} = 0 \tag{4.10}$$

$$w_{final,2}^{r+1} = z_{below,sf} + \frac{z_{above,sf} - z_{below,sf}}{T_{above,sf} - T_{below,sf}} * (T_{melt,slag} - T_{below,sf}) \tag{4.11}$$

$$w_{final,3}^{r+1} = w_{inter,3}^{r+1} \tag{4.12}$$

$$w_{final,4}^{r+1} = z_{domain,top} \tag{4.13}$$

$inter$: after mass balance within the time step , $final$: after energy balance within the time step , $r+1$: current time step [#], $w_{final,1}$: Molten steel - Liquid flux interface (domain bottom- fixed) [m], $w_{final,2}$: Liquid flux - Powder/Sinter interface [m], $w_{final,3}$: Powder/Sinter- Air interface [m], $w_{final,4}$: Air-Ambient interface (domain top- fixed) [m], $z_{below,sf}$: node/cell index below the phase boundary (powder/sinter- liquid flux) [m], $z_{above,sf}$: node/cell index above the phase boundary (powder/sinter- liquid flux) [m], $T_{below,sf}$: Temperature of the cell below the phase boundary (powder/sinter- liquid flux interface) [K], $T_{above,sf}$: Temperature of the cell above the phase boundary (powder/sinter- liquid flux interface) [K], $T_{melt,slag}$: Powder melting temperature (to form liquid flux) [K], $z_{domain,top}$: domain top boundary (sum of cell heights in the powder/slag layer, and air layer)

Even though a cell can contain multiple phases (Air, Powder, or Liquid), each cell is designated as a particular phase at a specific time based on the location of the phase boundary in the cell, and the node. If the interface passes through the cell center or is above it, then the cell is designated to have the phase below the interface. And, if the interface is below the cell center, then the phase above the boundary is assigned to the cell. This methodology is also applied to the phase boundary calculation for the mass balance discussed in the next section.

4.6.2 Phase boundaries after Mass balance

Next, the Liquid flux-sinter interface is dropped based on the instantaneous consumption velocity $v_{cons,f}$, and the time step size. The powder-air interface may increase by the powder addition amount/level known from the plant measurements/settings (if the current time corresponds to the powder addition time for intermittent powder addition case). Additionally, this interface drops due to two more reasons: a) Since the liquid flux layer at the bottom drops, this level drop also causes the powder/sinter interface to drop b) Due to heat transfer and sintering in the previous time step, powder particles become closely packed, and undergo densification. This powder compaction is another cause of a drop in powder levels. The total powder shrinkage is calculated by summing up all the instantaneous shrinkage (due to powder shrinkage velocity, $v_{shrink,p}$) experienced by all the cells based on their local temperatures and sintering times. The domain top (Air layer-ambient) and bottom (Liquid Flux-Molten steel interface) as well as the interfaces between all cells remain fixed throughout the simulation for this fixed-grid methodology. This explains the powder mass balance.

$$w_{inter,1}^{r+1} = 0 \tag{4.14}$$

$$w_{inter,2}^{r+1} = w_{final,2}^{r+1} - \frac{\dot{m}_{cons_f} * dt}{\rho_f * A_c} \tag{4.15}$$

$$w_{inter,3}^{r+1} = w_{final,3}^{r+1} - \frac{\dot{m}_{cons_f} * dt}{\rho_f * A_c} - ht_{shrinkage} \tag{4.16}$$

$$w_{inter,4}^{r+1} = z_{domain,top} \tag{4.17}$$

$inter$: after mass balance within the time step, $final$: after energy balance within the time step, $r+1$: current time step [#], $w_{inter,1}$: Molten steel - Liquid flux interface (domain bottom- fixed) $[m]$, $w_{inter,2}$: Liquid flux - Powder/Sinter interface $[m]$, $w_{inter,3}$: Powder/Sinter- Air interface $[m]$, $w_{inter,4}$: Air- Ambient interface (domain top- fixed) $[m]$, $\dot{m}_{cons_f}$: liquid flux consumption rate $[kg/s]$, dt: time step size $[s]$, ρ_f: liquid slag density $[kg/m^3]$, A_c: Strand cross-section area $[m^2]$, $ht_{shrinkage}$: total powder shrinkage $[m]$, $z_{domain,top}$: domain top boundary (sum of cell heights in the powder/slag layer, and air layer)

4.7 Solution Methodology

A flowchart of the advanced transient model is presented in Figure 4.2. The red and green boxes contain a transient, heat transfer submodel, and mass transfer submodel of the powder/flux layers that were explained in the previous sections. In the current chapter, we will be focusing on the thermal behavior of mold powders taking into account the effect of mass transfer, and phase transition due to melting, and verify the model with ANSYS Fluent. In the next chapter, we will explain the sintering

physics included in the multi-physics model and validate the model with lab sintering experiments [12]. Also, we will discuss the carbon and gas calculation capabilities of the model.

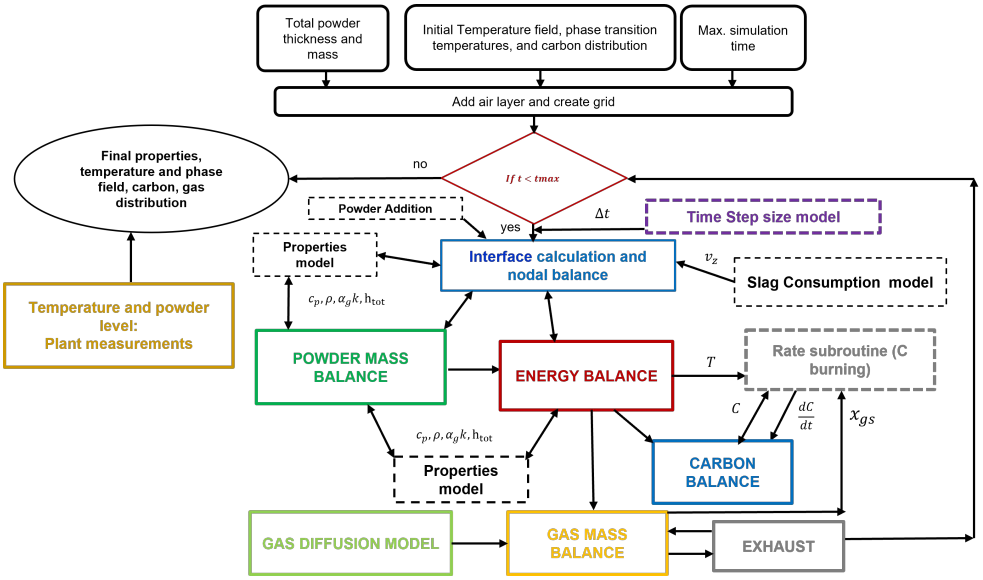

Figure 4.2 Transient Model Flow Chart

As shown in the flowchart, a time step size model is used to calculate a suitable time step size for marching the solution based on the stability criteria required for an explicit model. A slag consumption model is used to estimate the flux consumption into the gap between the solidifying steel and oscillating water-cooled copper mold. Property subroutines are used to estimate the powder properties such as thermal conductivity, density, specific heat, pore fraction as a function of temperature, location along the vertical direction, and time. The Energy balance module of the program calculates the temperature distribution through the powder/slag layers based on the governing equations, and boundary conditions. The Mass balance module takes into account the mass transfer between cells due to the powder addition, powder shrinkage, and liquid flux consumption, and considers the downward advection of powder as it heats up and densifies, or loses mass due to molten powder flowing into the gap to provide lubrication.

The model is first applied to predict the thermal profile and powder/slag levels in a continuous caster in a test problem to compare with a Fluent simulation for model verification. Sintering kinetics effects on shrinkage are not considered in this caster run. The surface temperatures and powder levels are also validated with plant measurements at Dofasco [32]. Next, the multiphysics model is applied including the sintering kinetics to predict the temperature distribution, powder shrinkage due to densification, and pore fraction for the lab measurements [12] without the liquid flux layer. The powder shrinkage is validated, and the temperature profile is verified with existing models in literature [12]. The multi-physics model is also

applied including the combustion and gas transport behavior (to be discussed in the next chapter). Finally, the complete model of the caster is simulated and compared with plant measurements at both Dofasco and Tata Steel for transient conditions involving intermittent powder addition.

4.8 Verification with Fluent model

To verify the simple transient thermal submodel, transient heating of powder in a steel continuous caster was simulated with two different computational models. Conditions were chosen to match a particular trial with HSLA steel in the Dofasco plant.[32] First, a simulation was conducted using the commercial code, Fluent, with the axisymmetric domain shown in Figure 4.3 (a)[32]. Temperature-dependent thermal properties are shown in Figure 4.3(b)[32]. A constant powder/slag density of $2600 kg/m^3$ was used owing to the inability of Fluent to easily handle the effect of shrinkage due to sintering. Other parameters are given in Table 4.1, including a liquid flux consumption rate of 60.1 kg/hr. Starting with a steady-state solution for 40 mm of cold powder, 10 mm of cold powder was added to the top surface, and thicknesses were assumed to remain constant while calculating transient evolution of the thermal profile.

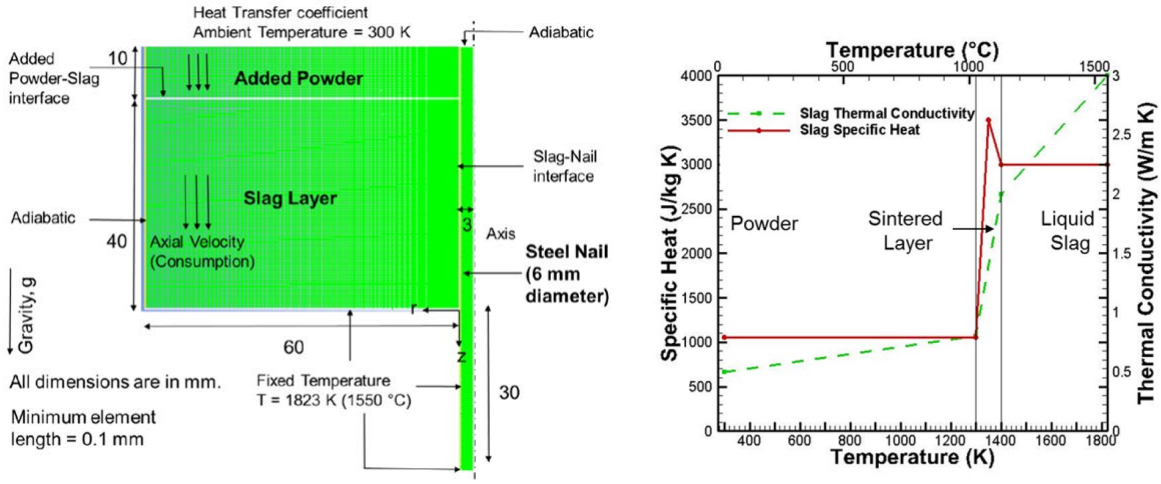

Figure 4.3 (a) Fluent Mesh [32](b) HSLA steel slag properties[32]

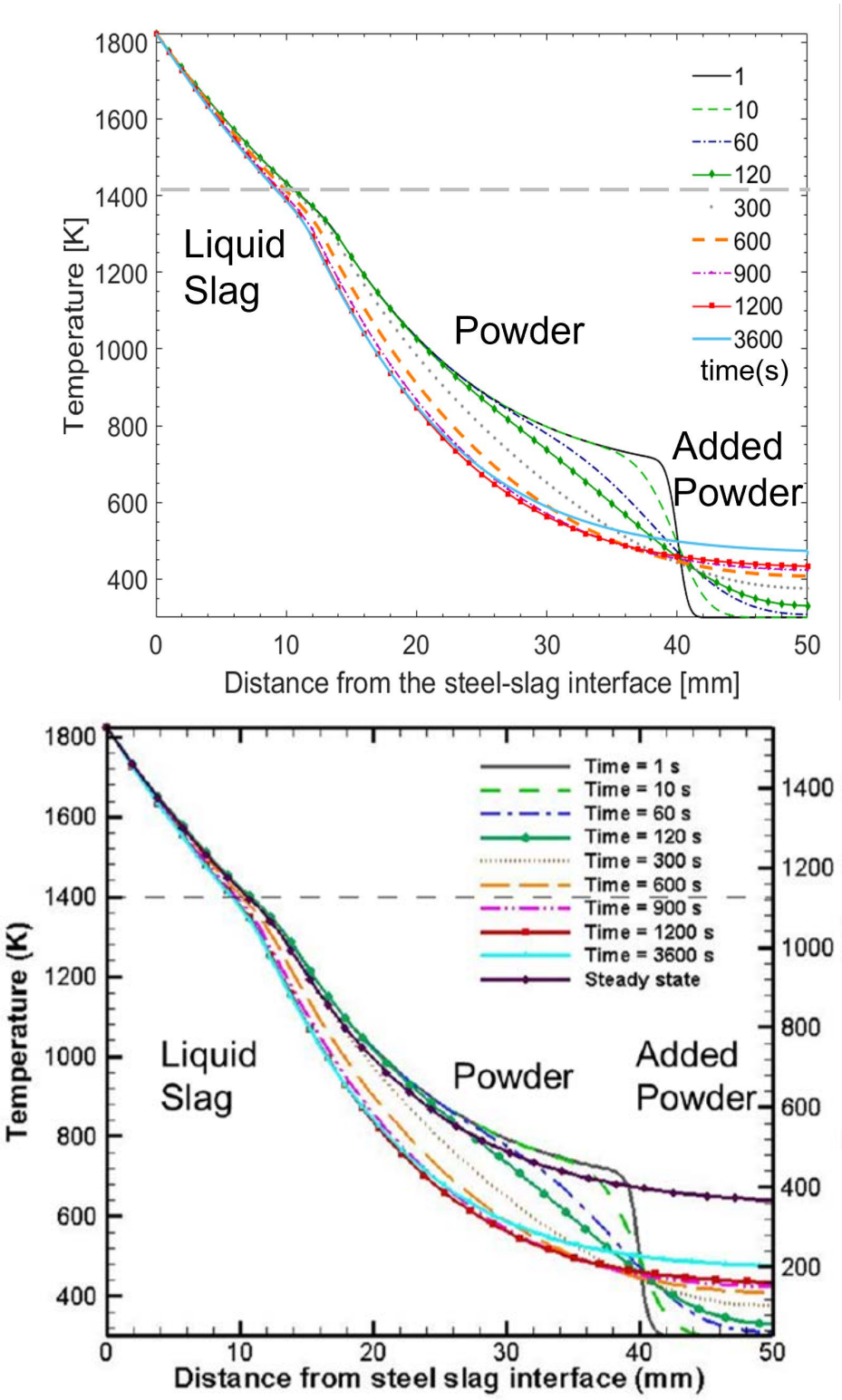

Figure 4.4 (a) Model verification (a) MATLAB in-house code (b) Fluent model [32]

Table 4.1 Casting conditions for the trial considered for model verification.

Casting conditions/Parameters	Value
Casting speed	1.4 m/min
Axial advection velocity	2.43*10$^-$5m/s
Molten Steel temperature	1823 K
Liquid flux- Sinter phase transition temperature	1400 K
Sinter- Powder phase transition temperature	1300 K
Strand width	1207 mm
Strand thickness	220 mm
Slag density	2600 kg/m^3
Heat transfer coefficient	3.3 W/m^2K

In this verification problem, a Fluent simulation was done to calculate the powder temperature distribution, and our current MATLAB-based model was run for similar conditions to compare the thermal profiles at different times. A constant powder/slag density of $2600 kg/m^3$ was used throughout the simulation (both MATLAB and Fluent). A time-step size of 0.0023s was used in the simulation. The heat transfer coefficient was low due to the continuous powder addition assumption which results in a high-temperature difference between the powder surface and the ambient). The powder surface temperature for the 40mm slag layer from the pyrometer reading at the plant was found to be 705 K.

Identical properties and conditions were used in both the in-house model and in Fluent. The thermal evolution of temperature during powder heating is shown in Figure 4.4. When cold powder is instantly added, the temperature drops in the powder interior, and gradually the new powder added to the top begins to heat up. The temperature evolution occurs slowly, as even after one hour, the temperature is still changing. The average time between powder additions in the plant is 3.5 minutes. And in the model after 3.5 minutes, the surface temperature was found to rise only to 90°C. The powder surface is thought to never reach steady-state condition, as powder additions keep happening from time to time.

The transient model results match with Fluent, as shown by comparing Figure 4.4 (a) with Figure 4.4 (b). Both of them exhibit a similar thermal evolution history. This verifies our model after which we proceed to validate our full model (except for liquid slag and consumption) with the sintering experiment.

CHAPTER 5
MULTIPHYSICS MODEL

After developing the simple transient model and applying it to predict the thermal behavior of continuous casting mold powders, the transient model is further expanded to include powder sintering physics, multi-species combustion reactions, exhaust gas balance, gas diffusion through the porous bed to predict the carbon, and gas distribution through the powder/sinter layer. This model uses the same domain shown in Figure 4.1, and tracks all three fluxes: heat flux, powder mass flux, and gaseous species flux. The gas behavior is not only coupled with the combustion physics but is also important in affecting the heat transfer through the powder layers by providing insulation. Therefore, it is imperative to study the carbon burning and gas evolution in mold powders. First, powder sintering behavior will be implemented into the multiphysics model. This will be followed by implementing the chemical reactions and gas transport through the mold powders. This multiphysics model will then be applied to the lab experiment of Supradist et. al. [12] where measurements are available for model validation, and then applied to the continuous caster (Chapter 7).

5.1 Sintering submodel

Granulated powders have a high porosity at room temperature. As the powder heats up, the particles become more closely packed (See Figure 5.1 and Figure 5.2), and the total porosity decreases. The total porosity is the sum of internal pores inside each hollow particle, and external pores in between the particles. So, the instantaneous apparent powder particle density, ρ_{app}, increases with both higher temperatures and longer times, t. Sintering rate kinetics are given by [12, 44, 45]:

$$\left(\frac{\rho_{app} - \rho^0_{app}}{\rho_s - \rho_{app}}\right)\frac{\rho_s}{\rho^0_{app}} = K_s t^n \tag{5.1}$$

The porosity of the powder/slag can be calculated using the powder density, and fully sintered theoretical density. The equation for powder pore fraction is as follows:

Pore fraction,

$$\alpha_g = 1 - \frac{\rho_{app}}{\rho_s} \tag{5.2}$$

The symbols and their units are defined in the Appendix, Table A.2.

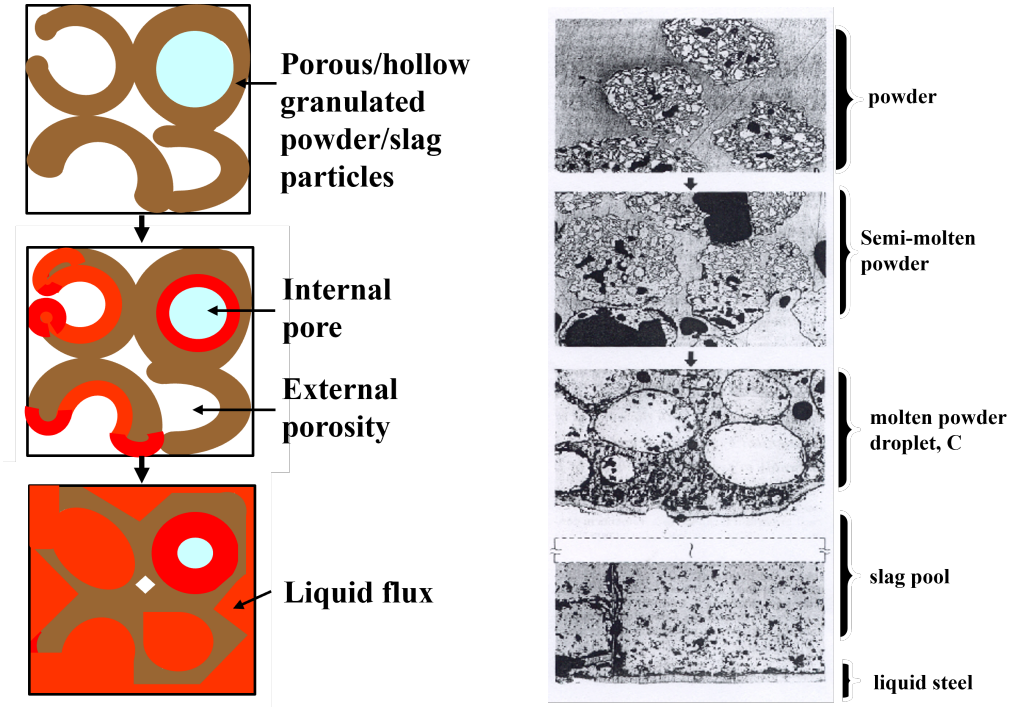

Figure 5.1 (a) Pore sintering and melting schematic, pores (white spaces) decrease as sintering occurs (b) Micrograph of the sintering process [11] (reproduced from Chapter 1)

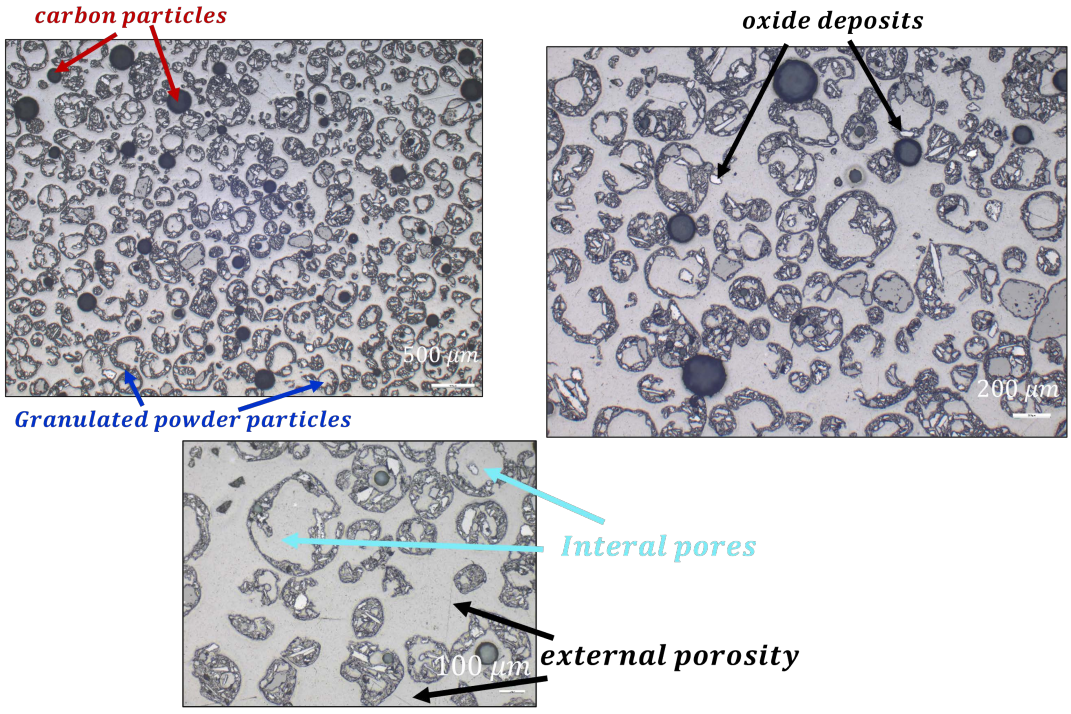

Figure 5.2 Closeup of powder/slag layers showing Optical micrographs at different magnification (a) 500x (b) 200x (c) 100x of mold powder structure [78]

The effective thermal conductivity relation of the powder/sinter layer is assumed to follow the relation by Russel[79].

$$k_{eff} = (\frac{1-\alpha_g^{1/3}}{k_{solid}} + \frac{\alpha_g^{1/3}}{(1-\alpha_g^{2/3})k_{solid} + \alpha_g^{2/3}k_{gas}})^{-1} \tag{5.3}$$

In the above equation, t: sintering time, Apparent density at $t = 0$, $\rho_{app}^0 = 620\ kg/m^3$, ρ_{app}: Instantaneous density, $\rho_s = 2700\ kg/m^3$ (solid powder density), $n = 0.5$, Sintering rate constant, $K_s(T < 400°C) = 0$, $K_s(600°C) = 0.036$, $K_s(800°C) = 0.045$, $K_s(1000°C) = 0.361$, k_{eff}: effective powder thermal conductivity, k_{solid}: solid powder thermal conductivity, k_{gas}: gas thermal conductivity, α_g: powder pore fraction.

The sintering model used in this work from literature has the physical flaw that the sintering always increases with increasing time even during cooling, which may not be realistic. This should be improved in the future by using a better correlation from the literature. For the most part, the powder is heating up, so we can expect the effect of this error to be small. Note that the measured data is fit with a continuously-increasing set of line segments, to avoid an illogical reversal in sintering and density.

The current sintering model can be improved by augmenting it with a microstructure-scale particle melting model in which: radial heat conduction within a generic shaped powder particle, its evolving surface area, evolving porosity/density, and conduction across the gaps and contact areas are all considered to track the degree of sintering for the macro-scale model.

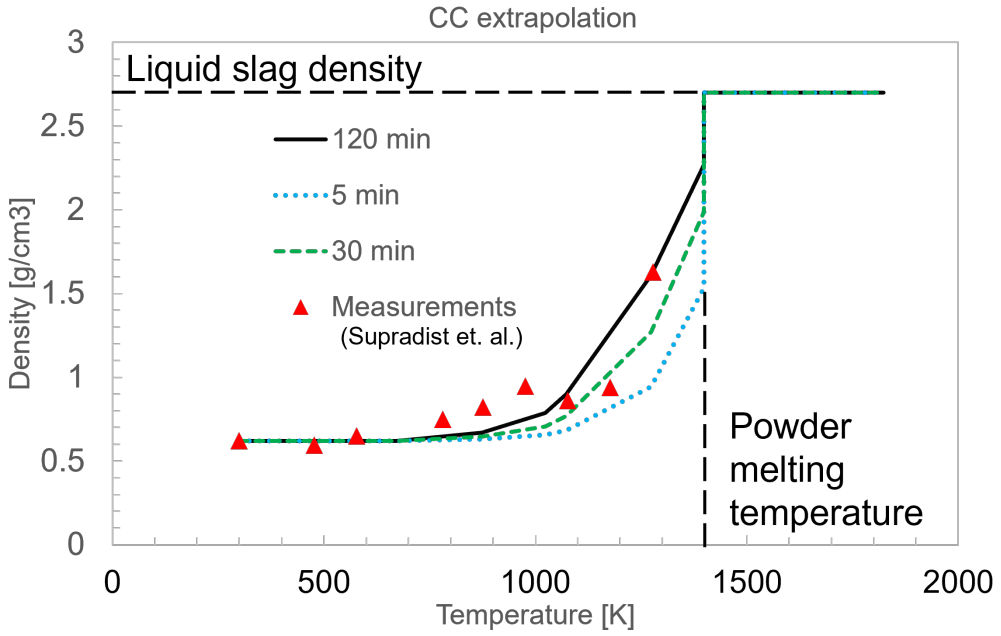

Figure 5.3 Powder sintered density - current model and measurements from literature[12]

As porosity decreases, density increases (Figure 5.3), and thermal conductivity increases, the total powder shrinkage is estimated to quantify the extent of densification. This is a step-wise linear approximate fit of the density measurement from the lab experiment[12]. The fitting has been done based on the measured value of sintering rate constants, and then the rate constant equations as a function of temperature are input into the sintering model to calculate the powder/slag density. The powder shrinkage velocity ($v_{shrink,p}$) is modeled in the same way as the flux consumption velocity ($v_{cons,f}$), which shifts mass downwards from the powder in each cell to the cell below.

To measure density, Supradist[12] placed the powder in an alumina crucible and heated it in an induction furnace for two hours at temperatures ranging from 200 to 1000 °C [12]. Later the samples were cooled, weighed, coated with wax (to prevent water penetration), and immersed in water (for samples heated above 600°C) to measure their volume using Archimedes' principle, and hence their density[12].

After describing the sintering model, the carbon combustion, and gas transport physics is introduced to predict the carbon and gas distribution due to the temperature, and density distribution through the powder layers.

5.2 Combustion and Gas Transport Model description

The heat transfer is modeled in the entire domain, while sintering behavior, gas transport, and combustion phenomena are modeled only in the powder layers. Carbon is assumed to be present in the form of free carbon, and no carbonate decomposition is considered in the current model because carbonate decomposition is slow and can be neglected. A constant system pressure of 1 atm is considered in the entire domain. This important assumption is reasonable because the powder layer is thin, and has low density, high porosity, and consequently likely very high permeability. Thus, any pressure build-up is expected to be small, so can be neglected in the model.

In addition to simulating the effect of chemical reactions, and diffusion, the current powder model is further improved to include the effect of shrinkage velocity and evaluate the resulting temperature, carbon, and gas distribution due to downward mass transfer because of powder shrinkage during sintering.

Due to the powder shrinkage during sintering, oxides and carbon present in the powder along with the gases contained in the cell get moved to the cells below. This results in carbon accumulation near the bottom of the sinter layer. This is because the carbon-rich material has too low density to penetrate through the liquid slag layer, which in turn floats on top of the molten steel. While applying the model to a continuous caster, the liquid flux consumption into the gap also has an additional effect on the advection of carbon, gas, and oxides in addition to the effect of powder shrinkage.

Combustion in the mold powder at a given time, t, during a simulation depends on the remaining carbon content, temperature, and gas content at the given location in the powder layers. Various phenomena need to be considered to accurately predict the carbon and gas distribution through the mold powders, including the chemical reaction kinetics, gas diffusion and transport through the pores, and gas exhaust from the top surface to the ambient. These in turn depend on the temperature, density (and, porosity, and phase compositions) calculated by the thermal and sintering models described in Chapter 4, and the previous section respectively. Depending on the temperature and pore distribution through powder, the combustion physics in certain regions of the powder can be reaction-controlled, or diffusion-controlled. The temperature and properties calculated by the heat and mass transfer model along with the sintering model results are input to this carbon and gas balance model. Gas diffusion also depends on two factors: (i)Kinetic effect- due to the thermal effects and (ii)Tortuosity effect- due to pore size, distribution, and powder particle size distribution. As the powder heats up, the carbon and gas distributions evolve to reach near-equilibrium at long times.

5.2.1 Combustion Gas reactions

A multi-species, 4-equation combustion model [12] (4-eCM) has been used to calculate the chemical reaction rates, and obtain the resulting carbon and gas distributions. The rates of combustion reactions ($mol/cm^3 min$) were taken from available literature [12, 13, 80, 81].

The gas reactions occurring in the powder during combustion in mold powders are presented below:

1. Carbon dioxide formation at low temperature

Carbon combusts in the presence of oxygen to form carbon dioxide at low temperatures in the powder interior (heterogeneous reaction)

$$C + O_2 = CO_2, \qquad (r_1) \tag{5.4}$$

The first reaction, r_1 is based on experimental work on carbon combustion of mold powders in air [12, 13].

$$r_1 = \frac{g_C^0 \rho_C}{M_C} (\frac{g_C}{g_C^0})^\alpha k_{O_2} p (x_{O_2} - \frac{x_{CO_2}}{K_{(1)}}) \tag{5.5}$$

The equilibrium and rate constants as a function of temperature are given by:

$$logK_{(1)} = \frac{20950}{T} + 0.088 \tag{5.6}$$

$$logk_{O_2} = \frac{-7590}{T} + 9.58 \tag{5.7}$$

where: r_1: Reaction rate [$mol/cm^3 powder/min$], g_C^0: Initial carbon volume fraction (0.0141) for the lab experiment, g_C: Carbon volume fraction at time t, ρ_C: Density of carbon ($2.2 g/cm^3$) (considered to be

constant during the heating process), M_C: Molecular mass of carbon ($12.011 g/mol$), α: exponent (1.87 at $400°C$)-assumed to be constant during the reactions, k_{O_2}: Rate constant for the reaction [$atm^{-1}min^{-1}$], p: partial pressure, x_{O_2}: Oxygen mole fraction [#], x_{CO_2}: Carbon dioxide mole fraction [#], $K_{(1)}$: Equilibrium constant, T: Temperature [K]

2. Carbon monoxide formation at high temperature- Boudouard reaction

Carbon combusts in the presence of carbon dioxide at high temperatures (close to the powder bottom) to form carbon monoxide (heterogeneous reaction). This reaction is endothermic, which is another reason why it requires a high powder temperature to occur (also it is thermodynamically stable).

$$C + CO_2 = 2CO \qquad (r_2) \tag{5.8}$$

The rate constants of this reaction are based on work on charcoal combustion by Turkdogan, [12, 81].

$$r_2 = \frac{g_C^0 \rho_C}{M_C} (\frac{g_C}{g_C^0})^\beta \frac{k_1 p (x_{CO_2} - \frac{p x_{CO}^2}{K_{(2)}})}{1 + k_2 p x_{CO} + k_3 p x_{CO_2}} \tag{5.9}$$

The equilibrium and rate constants as a function of temperature are given by:

$$logK_{(2)} = \frac{-9000}{T} + 9.219 \tag{5.10}$$

$$logk_1 = \frac{-13200}{T} + 9.68 \tag{5.11}$$

$$logk_2 = \frac{5850}{T} - 3.97 \tag{5.12}$$

$$k_3 = 0 \tag{5.13}$$

r_2: Reaction rate [$mol/cm^3 powder/min$], β: exponent (1 at $400°C$)-assumed to be constant during the reactions, k_1, k_2, k_3: Rate constants for the reaction, k_1: [$atm^{-1}min^{-1}$], k_2, k_3: [atm^{-1}], x_{CO}: Carbon monoxide mole fraction [#], $K_{(2)}$: Equilibrium constant [atm]

3. Carbon monoxide oxidation to form carbon dioxide- first half reaction

A small amount of carbon monoxide reacts with molecular oxygen to form carbon dioxide and atomic oxygen (homogeneous reaction)

$$CO + O_2 = CO_2 + O \qquad (r_3) \tag{5.14}$$

The rate constants of this reaction are based on work on charcoal combustion by Warnatz, [12, 80].

$$r_3 = 60 g_g c_g^2 k_{CO,O_2} (x_{CO} x_{O_2} - \frac{x_{CO_2} x_O}{K_{(3)}}) \tag{5.15}$$

The equilibrium and rate constants as a function of temperature are given by:

$$logK_{(3)} = \frac{1650}{T} - 1.215 \tag{5.16}$$

$$logk_{CO,O_2} = \frac{-10450}{T} + 12.40 \tag{5.17}$$

r_3: Reaction rate $[mol/cm^3 powder/min]$, k_{CO,O_2}: Rate constant for the reaction $[cm^3 mol^{-1} s^{-1}]$, x_O: Atomic oxygen mole fraction[#], $K_{(3)}$: Equilibrium constant g_g: gas fraction c_g: gas concentration $[mol/cm^3]$

4. Carbon monoxide oxidation to form carbon dioxide- second half reaction

A small amount of carbon monoxide reacts with atomic oxygen to form carbon dioxide in the presence of a metal ion catalyst (homogeneous reaction)

$$CO + O + M^+ = CO_2 + M^+ \qquad (r_4) \tag{5.18}$$

The rate constants of this reaction are based on work on charcoal combustion by Warnatz, [12, 80].

$$r_4 = 60 g_g c_g^3 x_M^+ k_{CO,O}(x_{CO} x_O - \frac{x_{CO_2}}{K_{(4)}}) \tag{5.19}$$

The equilibrium and rate constants as a function of temperature are given by:

$$logK_{(4)} = \frac{27940}{T} - 7.916 \tag{5.20}$$

$$logk_{CO,O} = \frac{-990}{T} + 13.85 \tag{5.21}$$

r_4: Reaction rate $[mol/cm^3 powder/min]$, $k_{CO,O}$: Rate constant for the reaction $[cm^6 mol^{-2} atm^{-1}/s^{-1}]$, x_O: Atomic oxygen mole fraction, $K_{(4)}$: Equilibrium constant $[atm^{-1}]$

The last two reactions (oxidation of carbon monoxide to form carbon dioxide) involving atomic oxygen, add up to give the resulting equation:

$$2CO + O_2 = 2CO_2 \tag{5.22}$$

For a lab sintering experiment, where the temperatures are low, the reaction rates, r_3, and r_4 might not be significant. But the primary objective behind developing this multi-physics model is to apply it to the continuous caster and predict the carbon distribution through the mold powder layers. Compared to the lab experiment, the temperatures through the powder/slag layers in a commercial caster are much higher (just below the melting point of the powder), and the rates, r_3, and r_4 are expected to become higher, therefore it is important to consider the post-combustion gas reaction equation (as carbon burns to form

CO_2, and the CO_2 formed reacts with residual C to form CO, then these two gases react with each other via a 2-step reaction, resulting in gas equilibrium.)

5.2.2 Gas conservation equations

As explained before, the gas transport equations need to be solved in order to obtain the resulting gas composition distribution, including the measured off-gas composition. The amount of gas stored in a particular cell, i, can change because of transients, gas advection in/out of the cell due to powder advection because of powder shrinkage, and liquid flux consumption, gas diffusion in/out of the cell, and due to chemical reactions either involving carbon (heterogeneous reaction) or simply gases reacting among themselves (homogeneous reaction). The change in solid volume fraction is considered in the porosity calculation in this model.

The species conservation equations for five gases considered in this model, namely Oxygen, O_2, Carbon dioxide, CO_2, Carbon monoxide, CO, Atomic Oxygen, O, Nitrogen, N_2 are presented below:

$$\frac{\partial(x_{O_2}c_g)}{\partial t} + \frac{\partial(\alpha_g x_{O_2} c_g(v_{shrink,p} + v_{cons,f}))}{\partial z} = \frac{\partial}{\partial z}\frac{D_{eff}c_g\partial x_{O_2}}{\partial z} - r_1 - r_3 \tag{5.23}$$

$$\frac{\partial(x_{CO_2}c_g)}{\partial t} + \frac{\partial(\alpha_g x_{CO_2} c_g(v_{shrink,p} + v_{cons,f}))}{\partial z} = \frac{\partial}{\partial z}\frac{D_{eff}c_g\partial x_{CO_2}}{\partial z} + r_1 - r_2 + r_3 + r_4 \tag{5.24}$$

$$\frac{\partial(x_{CO}c_g)}{\partial t} + \frac{\partial(\alpha_g x_{CO} c_g(v_{shrink,p} + v_{cons,f}))}{\partial z} = \frac{\partial}{\partial z}\frac{D_{eff}c_g\partial x_{CO}}{\partial z} + 2r_2 - r_3 - r_4 \tag{5.25}$$

$$\frac{\partial(x_{O}c_g)}{\partial t} + \frac{\partial(\alpha_g x_{O} c_g(v_{shrink,p} + v_{cons,f}))}{\partial z} = \frac{\partial}{\partial z}\frac{D_{eff}c_g\partial x_{O}}{\partial z} + r_3 - r_4 \tag{5.26}$$

$$\frac{\partial(x_{N_2}c_g)}{\partial t} + \frac{\partial(\alpha_g x_{N_2} c_g(v_{shrink,p} + v_{cons,f}))}{\partial z} = \frac{\partial}{\partial z}\frac{D_{eff}c_g\partial x_{N_2}}{\partial z} \tag{5.27}$$

here: x_{O_2}: mole fraction of oxygen [#]; x_{CO_2}: mole fraction of carbon dioxide [#]; x_{CO}:mole fraction of carbon monoxide [#]; x_O: mole fraction of atomic oxygen [#]; x_{N_2}:mole fraction of nitrogen [#] c_g: total gas concentration $[mol/cm^3]$; α_g: gas volume fraction in cell (estimate of powder porosity); $v_{shrink,p}$: powder shrinkage velocity $[cm/s]$; $v_{cons,f}$: liquid flux consumption velocity $[cm/s]$; D_{eff}: Effective gas diffusivity $[cm^2/min]$; t: time [s]; z: grid location [m] (distance from domain bottom) ; r_1, r_2, r_3, r_4: reaction rates $[mol/cm^3 min]$

The gas volume in the pores in each cell of the domain is updated according to the local temperature, and pressure given in the Exhaust model in this chapter. The equations are discretized using a second-order, finite-volume scheme, and solved in the porous (gas-containing) portion of each cell using an explicit method. The resulting terms (including the reaction rates) are multiplied by the cell volume, phase fraction, and time step size to solve for the moles of gaseous species.

The species conservation equations and the solution methodology described above represent general equations that apply to the multiphysics phenomena occurring through the powder/sinter layers in a real caster.

5.2.3 Carbon mass conservation equation

The calculated temperature distribution is used to solve for the profile of carbon distribution down the powder layers using reaction rates. The carbon depletion rate $(-r_1 - r_2)$, and the terms on the left in the equation below are multiplied by the time step size, cell volume, and powder volume fraction to calculate the amount of carbon changing due to mass being stored in the cell due to transients, carbon powder advection because of powder shrinkage, and liquid flux consumption, and chemical reactions in the powder/sinter. The moles of carbon remaining in each cell are calculated and converted to volume fraction based on the volume of powder and all gases present in the cell.

$$\frac{\partial c_C}{\partial t} + \frac{\partial (g_C c_C (v_{shrink,p} + v_{cons,f}))}{\partial z} = -r_1 - r_2 \tag{5.28}$$

Here, c_C: carbon concentration $[mol/cm^3]$, g_C: carbon volume fraction [#].

5.2.4 Carbon fraction calculation

The mass fraction of carbon in each interior powder cell is given by:

$$m^{r+1}_{C,burnt,i} = \Delta n^{r+1}_{C,burnt,i} * M_C \tag{5.29}$$

$$m^{r+1}_{C,rem,i} = m^{r}_{C,rem,i} - m^{r+1}_{C,burnt,i} - m^{r+1}_{C,adv,i} \tag{5.30}$$

$$m^{r+1}_{C,adv,i} = m^{r+1}_{C,adv,shrinkage,i} + m^{r+1}_{C,adv,consumption,i} \tag{5.31}$$

$$f^{r+1}_{C,rem,i} = \frac{m^{r+1}_{C,rem,i}}{m^{r+1}_{C,rem,i} + m^{r+1}_{P,rem,i}} \tag{5.32}$$

$$f^{r+1}_{C,burnt,i} = \frac{m^{r+1}_{C,burnt,i}}{m^{r+1}_{C,rem,i} + m^{r+1}_{P,rem,i}} \tag{5.33}$$

$$f^{r+1}_{C,adv,i} = \frac{m^{r+1}_{C,adv,i}}{m^{r+1}_{C,rem,i} + m^{r+1}_{P,rem,i}} \tag{5.34}$$

$\Delta n^{r+1}_{C,burnt,i}$: decrease in the number of moles of carbon due to combustion in cell i and current time step, M_C: Molar mass of carbon (g/mol), $m^{r+1}_{C,burnt,i}$: mass of carbon burnt in cell i at current time step, $m^{r+1}_{C,rem,i}$: mass of carbon remaining in cell i at current time step, $m^{r}_{C,rem,i}$: mass of carbon remaining in cell i previous time step, $m^{r+1}_{P,rem,i}$: mass of powder in cell i at current time $m^{r+1}_{C,adv,i}$: mass of carbon advected from the cell due to powder shrinkage and liquid flux consumption at the current time step, $m^{r+1}_{C,adv,shrinkage,i}$: mass of carbon advected from the cell due to powder shrinkage at the current time step,

$m^{r+1}_{C,adv,consumption,i}$: mass of carbon advected from the cell due to liquid flux consumption at the current time step, $f^{r+1}_{C,burnt,i}$: mass fraction of carbon burnt, $f^{r+1}_{C,rem,i}$: mass fraction of carbon remaining in the cell, $f^{r+1}_{C,adv,i}$: mass fraction of carbon advected from the cell

5.2.5 Gas Diffusion- Effect of Temperature and Powder Tortuosity

The tortuosity factor for gas diffusion through powder particles has been experimentally determined by Schwerdtferger and Sardemann [82] by measuring the gas diffusivity, and the expression was derived as follows:

$$\tau = \frac{\alpha_g}{1 - 0.6\rho_s(1 - \alpha_g)} \tag{5.35}$$

The tortuosity factor further decreases the value of gas diffusion along with pore fraction. At high temperatures, the kinetic effect should increase resulting in higher gas diffusivity, but as the particles get more closely packed, the pore fraction decreases, and also the path for gas movement in the powder becomes more tortuous, and hence the effective gas diffusivity doesn't increase much.

Supradist et. al [12] modified the equation by Schwerdtferger and adopted it in the current model as well for the mold powder used in the lab sintering experiment. The equation used by Supradist for powder tortuosity calculation is given below:

$$\tau = 1 + 16\frac{\rho_{app}}{\rho_s} \tag{5.36}$$

The effect of temperature on gas diffusivity is from the classic Chapman-Enskog kinetic theory of gases [83]:

$$D_{O_2-N_2} = 0.0018583\frac{T^3(\frac{1}{M_{O_2}} + \frac{1}{M_{N_2}})}{P\sigma^2_{O_2-N_2}\Omega_{D_{O_2-N_2}}} \tag{5.37}$$

where, $D_{O_2-N_2}$: Kinetic Diffusivity, T: temperature [K], M_{O_2}: Molecular weight of oxygen [32 g/mol], M_{N_2}: Molecular weight of nitrogen [28 g/mol], P: pressure [atm], $\sigma_{O_2-N_2}$: Collision diameter (angstrom), $\Omega_{O_2-N_2}$: Collision integral for $O_2 - N_2$

A binary gas mixture relationship is used in this model based on oxygen and nitrogen, and other gases are assumed to have this same diffusivity [12].

The effect of powder tortuosity on gas diffusivity is given below:

$$D_{eff} = D_{O_2-N_2}\frac{\alpha_g}{\tau} \tag{5.38}$$

where, D_{eff}: effective diffusivity $[cm/min]$, α_g: pore fraction, ρ_s: fully sintered powder density $[kg/m^3]$, ρ_{app}: instantaneous powder density $[kg/m^3]$, τ: Tortuosity factor (depends on particle size, shape, and distribution and is generally greater than 1)

The gas diffusivity is shown in Figure 5.4. The effective diffusivity is used in the model to calculate the effect of gas diffusion through the pore spaces in the powder. For most of the powder interior, the gas diffusivity increases as we approach higher temperatures close to the powder bottom.

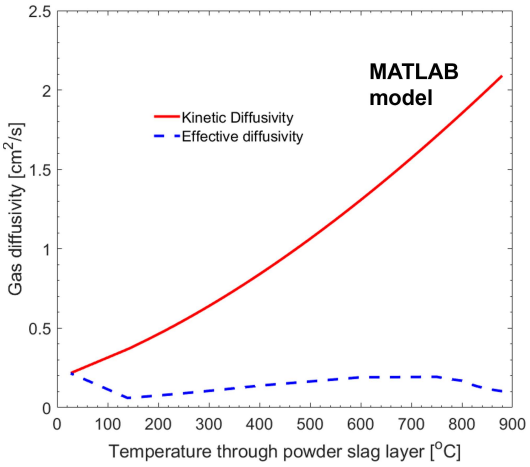

Figure 5.4 Gas diffusivity

5.2.6 Exhaust Model

The gas released due to the chemical reactions in a particular cell expands as the gas in the pore spaces between the powder particles heats up, and can no longer be accommodated in the pore spaces under the isobaric conditions ($P = 1atm$). Therefore, starting from the cell at the bottom of the domain, which cannot eject gas downwards, the gas gets ejected from the bottommost cell to the cell above, mixes with the gas in the cell, and then due to pressure balances on that cell, ejects some gas to the cell above it. This happens in each cell, and the net exhaust comes out from the top cell at the powder/air surface. The gas leaving a particular cell is considered to have the average composition of the gas inside the cell as gases mix. To take advantage of the explicit nature of the numerical solution procedure, the mixing of the exhaust from a cell with the gas in the cell above is neglected. This avoids the complexities of calculation becoming step-wise coupled, which could significantly slow down the simulation. So, the exhaust for all cells is calculated in a one-step approach, and it gets passed from one cell to another and gets released at the powder top surface.

$$n_{g,total,i}^{r+1} = n_{O_2,i}^{r+1} + n_{O,i}^{r+1} + n_{CO_2,i}^{r+1} + n_{CO,total,i}^{r+1} + n_{N_2,total,i}^{r+1} \tag{5.39}$$

$$V_{pore,i}^{r+1} = \alpha_{g,i}^{r+1} * A_c * ht_{cell,i}^{r+1} \tag{5.40}$$

$$n_{pore,i}^{r+1} = \frac{P_{tot} * 101325 * V_{pore,i}^{r+1}}{R_g * T_i^r} \tag{5.41}$$

$$n_{ae,gs,i}^{r+1} = n_{be,gs,i} - x_{be,gs,i} * (n_{g,total,i}^{r+1} - n_{pore,i}^{r+1}) \tag{5.42}$$

$n_{g,total,i}^{r+1}$: total amount of gaseous moles in cell i at time t, $n_{O_2,i}$: moles of oxygen in cell i at time t, $n_{O_2,i}$: moles of atomic oxygen in cell i at time t, $n_{CO_2,i}$: moles of carbon dioxide in cell i at time t, $n_{CO,i}$: moles of carbon monoxide, in cell i, at time t, $n_{N_2,i}$: moles of nitrogen, in cell i at time t, $V_{pore,i}^{r+1}$: pore volume in cell i at time, t (current time step) $[m^3]$, R_g: gas constant $[8.3144 J/mol - K]$, T_i: Temperature at node i [K], $n_{ae,gs,i}^{r+1}$: Gas species moles remaining in the cell after exhaust, $n_{be,gs,i}$: gas species moles in the cell after combustion and diffusion calculations (before exhaust) in the same time step, $x_{be,gs,i}$: Mole fractions of gas in the cell before exhaust the outgoing gas leaves at the same composition [#], $n_{pore,i}^{r+1}$: number of total gas moles that can be accommodated in the cell, at the given temperature and pressure.

5.2.7 Simulation details, and time step size calculation procedure

The model equations and the solution methodology described in the sections above in this chapter are used to calculate the temperature, density, pore fraction, carbon, and gas distribution through the powder/slag layers. The previous chapter presented the model flowchart in Figure 4.2. As seen in the figure, the model is generally initialized with a given powder/slag thickness, uniform ambient temperature field, cold-powder porosity and density (the initial time and temperature distribution can be used to calculate the density and porosity distribution based on sintering rate kinetics), the mass of the cold powder (the density and the pore fraction distributions can be used to evaluate the mass distribution of oxides and carbon in the powder), and powder/slag grid (extracted from the initial temperature distribution), and air grid information (needs to be sufficient enough to handle the powder additions). Some runs are initiated with a steady state solution. The powder addition information (mass of powder added/measured powder heights, and times of powder addition) are also input initially into the model.

First, the computational domain is discretized into a uniformly spaced one-dimensional grid of finite-volume model cells through the powder and air layer. The powder thickness generally varies from 35-55 mm. A grid size of 0.1mm is used for the study based on the grid-independence studies with the steady-state model (Chapter 3).

An explicit scheme is used for this multiphysics model to calculate the temperature, carbon, and gas distribution in a simple, step-wise coupled manner solved in the commercial package MATLAB. For each time step, a time-step criterion satisfying stability criteria for heat conduction, advection, and gas diffusion is calculated as follows:

$$\Delta t_{cond} = 0.1\frac{\Delta z^2}{\alpha}, \quad \Delta t_{adv_1} = 0.5\frac{\Delta z}{v_{cons,f}}, \quad \Delta t_{adv_2} = 0.5\frac{\Delta z}{v_{shrink,p}}, \quad \Delta t_{diff} = 0.1\frac{\Delta z^2}{D_{eff}} \tag{5.43}$$

$$\Delta t_t = 0.9 * min(\Delta t_{cond}, \Delta t_{adv_1}, \Delta t_{adv_2}, \Delta t_{diff}) \tag{5.44}$$

Δt_{cond}: time-step size based on heat conduction, Δt_{adv_1}: time-step size based on flux consumption velocity, Δt_{adv_2}: time-step size based on powder shrinkage velocity, Δt_{diff}: time-step size based on gas diffusivity, Δz: grid spacing, α: powder thermal diffusivity, $v_{shrink,p}$: powder shrinkage velocity, $v_{cons,f}$: flux consumption velocity, D_{eff}: Effective gas diffusivity.

Since the powder thermal properties, shrinkage velocity, and gas diffusivity vary throughout the domain with time, the cell with the maximum value is chosen for calculating the critical time step size. This criterion is checked at every time step to make sure all of the stability criteria are satisfied. The time-step size for heat transfer simulations was typically $\sim 1.6 * 10^{-3}s$. However, while solving the combustion and gas reactions, due to high gas diffusivity through the porous powder bed, the maximum time step size became about 100 times smaller ($\sim 1.6 * 10^{-5}s$).

The next calculation during each time step is to evaluate the slag consumption velocity and the powder/slag properties (thermal conductivity, specific heat, density, pore fraction). The density is calculated using the sintering submodel in Section 5.1. Then, the interface locations are updated using linear interpolation based on the phase transition temperatures for the powder-liquid interface, and the powder thickness for the air-powder interface, as described in Section 4.6.

Then, the energy balance is calculated by solving the second order, 1-D, finite volume method solution of the equations in Section 4.2 for the temperature distribution. This calculation includes the heat fluxes due to conduction, advection, the air-powder interface condition, which considers the convective and radiative losses at the powder top surface in Section 4.3, and the thermal boundary conditions in Section 4.4.

After this, the mass balance is calculated by solving the second order, 1-D, finite volume method solution of the equations in Sections 5.2.1-5.2.4 for the moles of powder, carbon, and gas species in each cell. This calculation accounts for the powder addition, liquid flux consumption, and powder shrinkage due to sintering.

This mass balance starts with the calculation of the carbon distribution through the powder/slag cells. This calculation accounts for the chemical reactions through a combustion rate subroutine (carbon burning), as shown in Figure 4.2. It also accounts for carbon advection due to shrinkage because of powder sintering, and the liquid flux consumption. The gas species molar calculations are done considering the coefficient of gas diffusion through the pores (Section 5.2.5), advection due to powder shrinkage, and change in gas species due to participation in the chemical reactions. The next step in the mass balance is the exhaust model described in Section 5.2.6, which is used to calculate the gas moles that need to be

ejected from each cell, including from the top surface, in order to maintain constant system pressure (1 atm) in the powder layer.

Finally, the gas species mole fractions are calculated from the above results. This stepwise coupled calculated procedure is carried out to complete the solution, and the computational results are then validated with the plant/lab sintering measurements.

The model took 5 days to run two hours of combustion and gas transfer calculations on a 1-node personal Windows-10 computer workstation (AMD Ryzen Threadripper PRO 5995WX, 2.7 Ghz, 512GB RAM).

5.3 Lab Powder Sintering experiment case

The multiphysics model is next applied to a lab experiment by Supradist [12] involving powder sintering to validate the powder shrinkage and densification calculations, in addition to the heat transfer model prior to applying to it a commercial caster. In this lab sintering experiment, cold powder (premixed with $5wt.\%$ graphite) is placed in a quartz tube and heated in an induction furnace for two hours [12], and the off-gas is first passed through a filter, and collected after passing it through a large gas hood and exiting through a small outlet to a gas analyzer. The setup is shown in Figure 5.5. The temperature profile, and powder shrinkage, are measured after the 2-hour experiment. The powder layers are also analyzed to measure the vertical carbon composition profile. The lab sintering experiment from the literature used to validate our model did not involve a liquid flux layer.

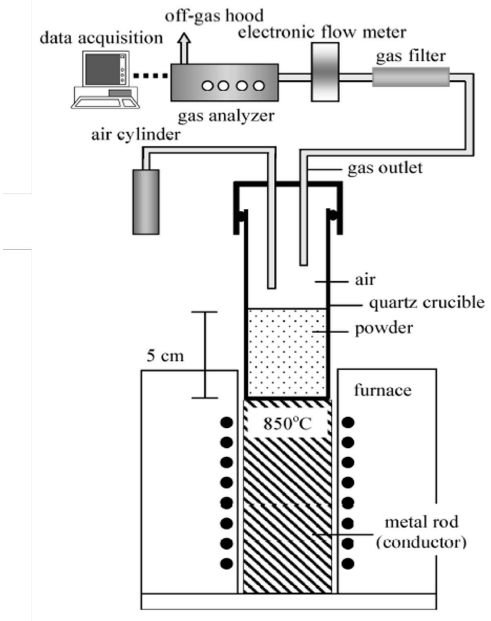

Figure 5.5 Lab setup for powder sintering experiments [12]

The multiphysics model is run for similar conditions to simulate the lab experiment, including the temperature profile along the powder column, sintering and the accompanying shrinkage of the powder column, carbon profile, and gaseous exhaust. The model is run for two cases, where Case 1 corresponds to a furnace temperature of 834 °C, and Case 2 bottom boundary condition, (fixed temperature) of the furnace temperature of 880 °C. Temperature measurements are available for Case 1, while Carbon distribution measurements are made for Case 2. So, the model is run for both cases, and the temperature results are validated for Case 1, while, temperature results are verified for Case 2 by comparing with results from another model in literature [12]. Sintering behavior is analyzed by observing model predictions of pore fraction and density considering powder shrinkage due to heating. Finally, the gas transport and carbon combustion is compared by analyzing the carbon and gas distribution through the powder/slag layers.

The thermal profile predicted by the model for case 1 is shown in Figure 5.6 (a). Initially, the powder is at room temperature (300K), but gradually it heats up from the bottom plate upward. The powder bottom almost instantaneously reaches the furnace temperature, but the powder layers on the top are the slowest to heat up. The highest temperature is at the bottom, and the temperature decreases as we move close to the top surface. The model temperature predictions lie within the error bounds of experimental measurements in the powder-top region, while higher temperatures are closer towards the powder-bottom. This can be attributed to certain experimental errors while moving the wire to measure shift in powder heights at different locations [84].

Due to sintering, the powder is undergoing densification, and so, the total powder level keeps dropping with time. This can be seen clearly in Figure 5.6 (a) where the top point in each temperature profile becomes lower at each time (seconds). The net powder shrinkage after 2 hours is compared with powder level measurements [12] in Figure 5.6 (b). The current model predicts slightly less shrinkage than the measurements but is reasonably close, so the sintering physics appears to be properly considered in the model.

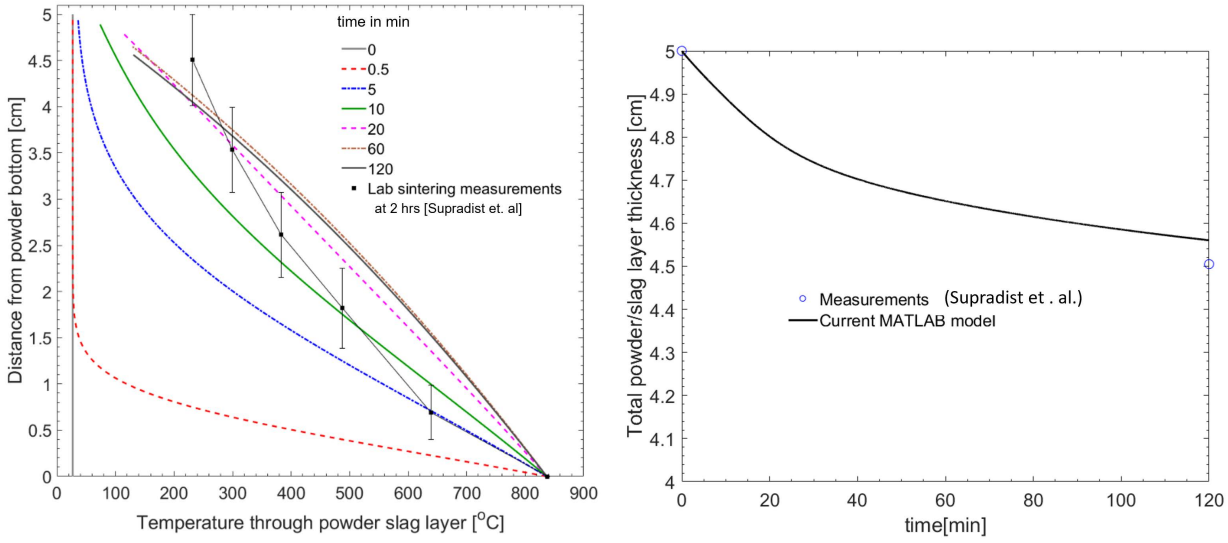

Figure 5.6 Case 1:(a) Thermal profile b) Powder Shrinkage

Next, the temperature profile is simulated for the carbon measurements case (Case 2). The thermal conductivity profile predicted by the model based on the temperature distribution after 2 hrs is shown in Figure 5.7. It is observed that as the temperature increases, the powder particles get more densely packed, and the pore fraction decreases, so the effective conductivity of the powder increases. The transition temperatures where the sintering rate constant changes slope are seen to reflect in the thermal conductivity profile. At low temperatures such as in the lab experiment, the powder's specific heat doesn't change much, therefore it can be considered to be constant [32]. But, in a commercial caster where the temperatures are higher, the specific heat of the powder/slag changes a lot due to reactions, sintering, and melting.

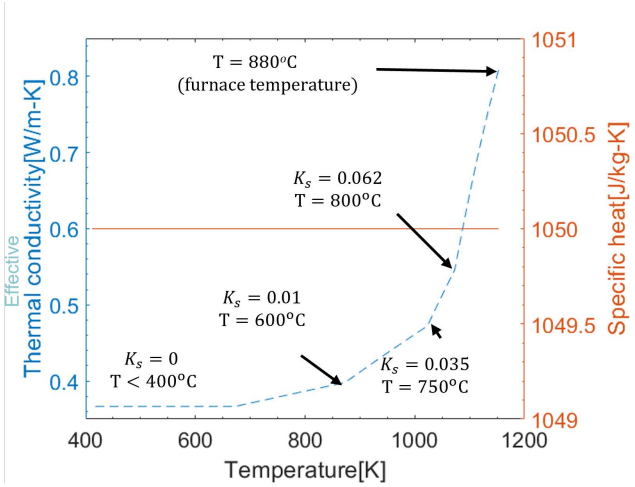

Figure 5.7 Case 2: Powder thermal conductivity as a function of temperature (higher temperature leading to lower pore fraction, and hence, higher thermal conductivity)

The temperature profile predicted by the current multiphysics model and from literature are shown in Figure 5.8. As with Case 1, predictions for Case 2 show that the powder bottom temperature agrees well with the model predictions from the literature, but the powder top surface is found to be slightly colder due to a different convection correlation used in the current model. There is a reasonably good match between both models.

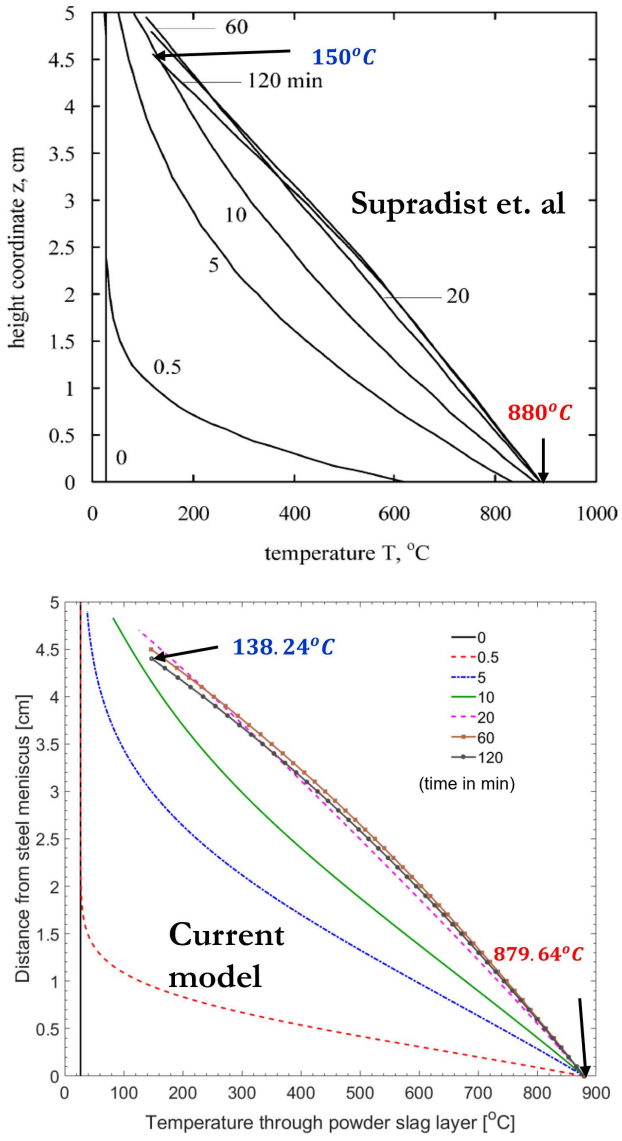

Figure 5.8 Case 2: (a) Thermal profile- literature [12] b) Temperature profile- Current Matlab Model

Since the temperature for case 2 is higher than case 1, the powder is found to be more packed, and hence has a lower height at the end of the sintering experiment after 2 hrs.

The thermal contours are shown in Figure 5.9 (b) where the highest temperature is seen at the powder bottom surface, and lowest temperature is seen at the powder top surface.

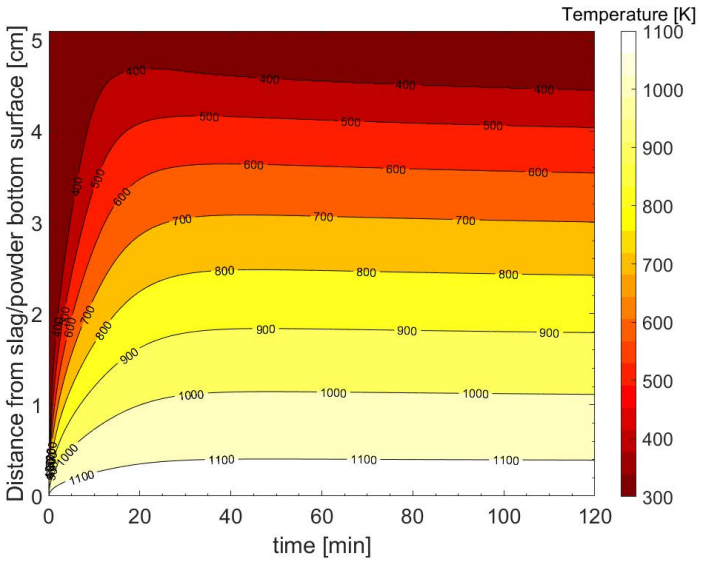

Figure 5.9 Temperature contours [Case 2]

Thermal diffusion and shrinkage of the powder column due to densification caused by powder sintering facilitate heating of the powder column with time. Temperature increases from the top surface (140 °C) to the bottom surface (879°C).

The powder shrinkage for this case is shown in Figure 5.10. It matches well with the measurements.

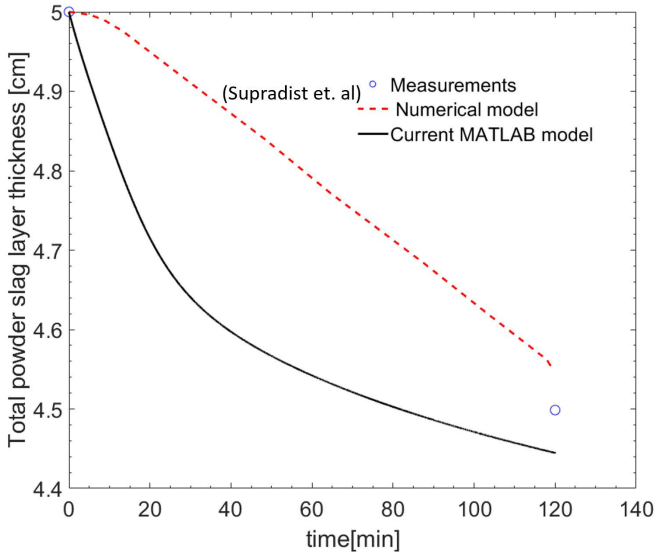

Figure 5.10 Case 2: Powder shrinkage validation and verification with Supradist model [12] and measurements [12]

The variation of density and pore fraction for case 2 is shown in Figure 5.11. Densification occurs as a function of temperature and time. Lower porosity, and consequently higher density is observed at higher temperatures and longer times. Since the temperature is highest at the powder bottom, the powder particles get densely packed resulting in the lowest pore fraction, and highest powder density. Since the sintering rate constant has a negligible value at temperatures lower than 400 °C, the warm powder towards the top surface has the same density as cold powder at room temperature.

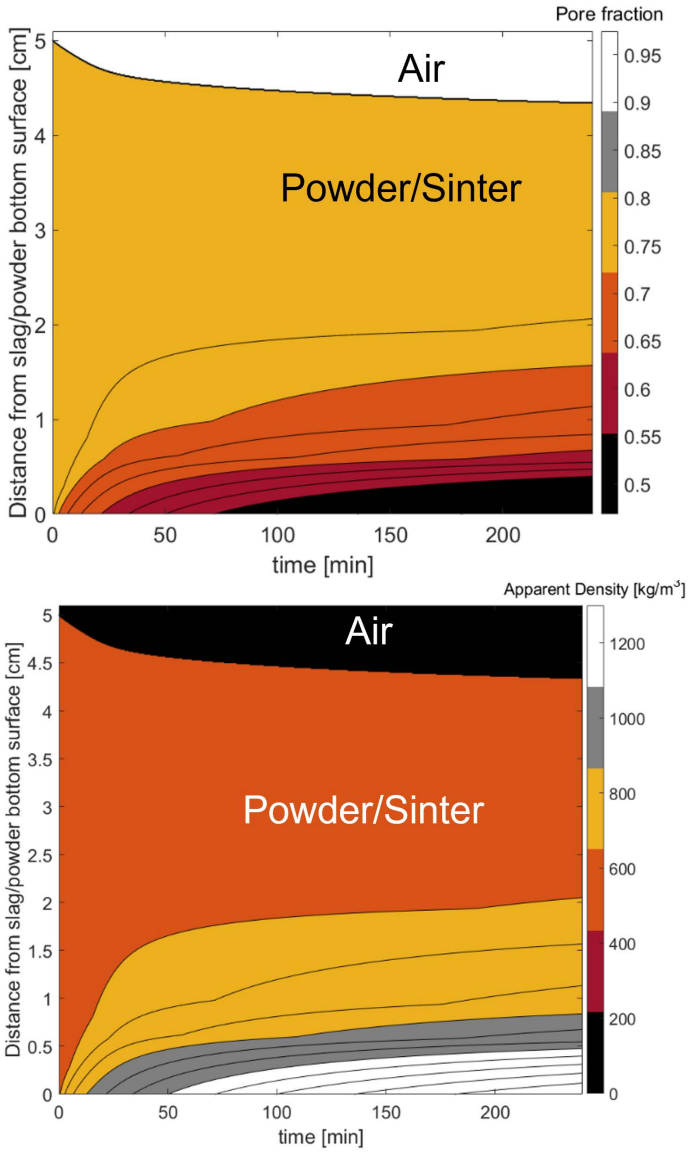

Figure 5.11 Case 2: (a) Pore fraction distribution b) Density contours

5.4 Combustion and Gas distribution results

The multiphysics model is run for the lab sintering case, and the results are compared with measurements in order to validate the model prior to applying it to the real commercial continuous casting process of interest. In the experiment by Supradist et. al, the powder has an initial height of 5 cm and is placed in a quartz tube with an inner diameter of 3.41 cm, left to undergo sintering and combustion for 2 hrs. The final powder height, density, carbon, and off-gas distribution are measured. The input density and powder shrinkage validation have been presented earlier in this chapter. The results of carbon combustion and gas transport will be discussed in this section. Air in the model domain on the top of the powder is considered to have a density of $1.225 kg/m^3$, a specific heat of $1004.9 J/kg - K$, and thermal conductivity of $2.624 * 10^{-2} W/m - K$.

The combustion and gas transport model results are given in Figure 5.12. Initially, cold powder at room temperature has a uniform carbon content (volume fraction of 0.0141). But as the thermal gradients develop in the powder with time, due to heat and mass flow, and sintering, the carbon distribution becomes non-uniform. Towards the top of the cold powder, the temperature is too low for combustion reactions to occur. So, the carbon content in the **'raw powder zone'** remains constant.

Towards the powder mid-zone, carbon combustion occurs by reaction with oxygen to form carbon dioxide (**Carbon-depleted zone**). As we move a bit deeper into the powder (still in the carbon-depleted zone), temperatures increase in the powder, thereby driving the equilibrium to the right for the formation of carbon dioxide (r_1). Due to this, more oxygen gets consumed, and carbon dioxide gets produced. There is a molar balance between the amount of oxygen that is consumed and the amount of carbon dioxide that is produced (which the model is found to satisfy). Available oxygen decreases due to chemical reactions, and it also gets removed as exhaust. The gas expands at higher temperatures, cannot be accommodated in the available pore space, and has to exit the domain. This continues until the powder runs out of oxygen (in reality the reaction reaches an equilibrium at a very low oxygen concentration ($\sim 10^{-26}$). This is where the 'carbon depleted zone' ends. As powder heats up, the zone shifts higher in the powder layer, and the cold powder in the upper zones gradually begins to heat up.

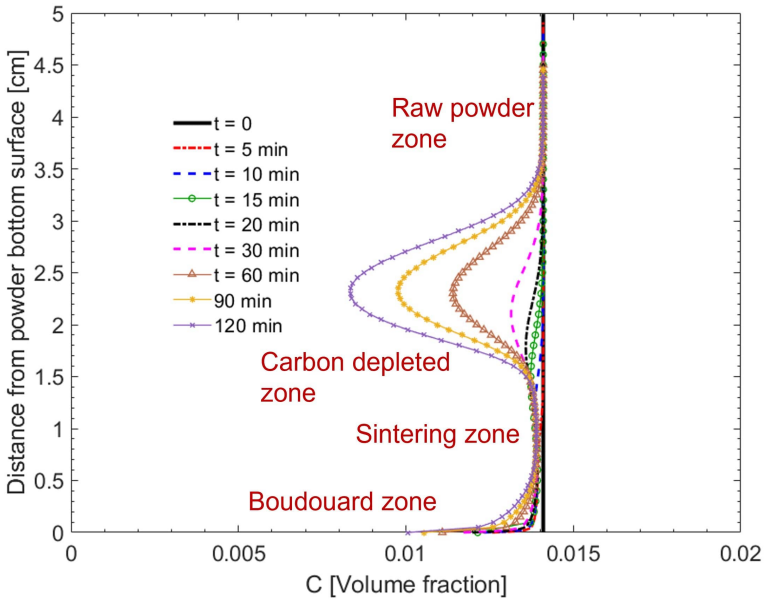

Figure 5.12 Time evolution of carbon distribution through the powder/sinter (a) Time evolution b) Model validation

Now, since the powder has exhausted almost all the available oxygen in the mid-zone, even though the temperature below is higher, carbon combustion cannot occur. So, in this region, the carbon burning slows (below the 'carbon depleted zone'). Then as we move even deeper into the powder, the temperature gets even higher, but it isn't hot enough for the endothermic Boudouard reaction to occur, and no oxygen is also available for carbon combustion. But, gas diffusion is happening in this zone as the powder is hot, and still, sufficient pore space is available for gas to diffuse into. There is some increase in carbon content in this zone due to gas diffusion, but the experiments show that there is a well-defined carbon accumulation zone around the powder here (**Sintering zone**).

Our initial simulation of the lab sintering experiment using the multi-physics model couldn't predict an increase in carbon content which is likely due to neglecting the shrinkage velocity effect. But later work presented towards the end of the chapter, shows a prominent increase in carbon content, and accumulation close to the powder bottom. The model is being further improved for better validation. As discussed earlier, some of the carbon can move down, and collect there without being able to burn as explained above. This results in a C-enriched sinter layer, which has been widely reported in the literature in the powder layers of operating steel continuous-casters.

As we move deeper into the powder layer, the powder begins to heat up even more, but it hasn't reached the phase-melting temperature to form liquid flux. Here, the temperature is so high (**Boudouard zone**), that carbon combustion (r_2) begins again where carbon reacts with the carbon dioxide present in

the pores to form carbon monoxide (Boudouard reaction).

The model predictions are compared with lab sintering measurements (Figure 5.13) found in the literature [12]. A reasonable agreement is observed between both in the variation of residual carbon profile.

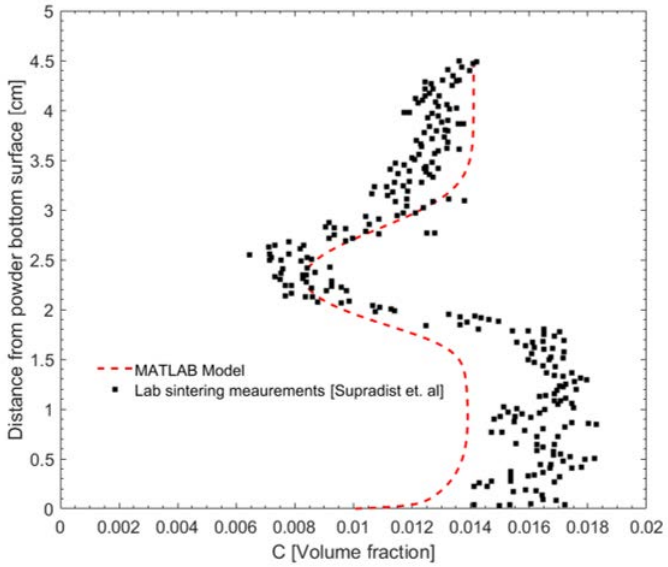

Figure 5.13 Model validation of carbon distribution through the powder/sinter

There is hardly any combustion occurring in the top region of the powder. While moving deeper into the powder column, carbon was consumed in the combustion process, to reach a minimum in the powder mid-zone. Towards the bottom, a prominent carbon accumulation region was observed in the measurements. The carbon burning predicted by our model shows the same trend as the measurements but is greater than the measurements, and the increase in carbon content towards the powder bottom is not observed in our initial model results. This is because the mass transfer of carbon occurs in a vertically downward direction towards the powder bottom due to shrinkage velocity from sintering and densification. This physics has been considered in a later developmental version of the model, and results are presented towards the end of this chapter. We expect that as some of the carbon shifts down, less carbon will be available to combust in the mid-zone, and carbon accumulation will occur towards the bottom. So, incorporating this effect will result in better validation with measurements.

The model outputs the gaseous exhaust which are post-processed considering transient mixing in the region above the mold powder in the quartz tube. The container mixing model solves a first order ordinary differential equation (ODE) considering the container (domain above the mold powder) as a single cell where perfect mixing is assumed. The equation is solved with a simple explicit model in MATLAB. Note that at steady state, the gas concentration leaving the container is calculated from the exhaust gases

leaving the powder layer, and the air flow entering the container (21% O_2, and 79 % N_2) according to the following equations:

$$\dot{n}_{gs} = \frac{n_{gs}}{\Delta t} \tag{5.45}$$

$$\dot{n}_{tot} = \sum \dot{n}_{gs} \tag{5.46}$$

$$\dot{V}_{flow,rate,gs} = V_{exp,fac} * \dot{n}_{gs} \tag{5.47}$$

$$\dot{V}_{flow,tot} = \sum \dot{V}_{flow,rate,gs} \tag{5.48}$$

Note that in the case of steady state, the above general equations simplify to the following:

$$\alpha_{gs}[\%] = \frac{\dot{V}_{flow,rate,gs}}{\dot{V}_{flow,tot} + \dot{V}_{air,flow}} * 100 \tag{5.49}$$

where: $\dot{n}_{gs}$: instantaneous molar flow rate of gas species released as exhaust [moles/s], n_{gs}: moles of exhaust of gaseous species [moles], Δt: time step size [s], $\dot{n}_{tot}$: total flow rate of gas [moles/s], $\dot{V}_{flow,rate,gs}$: volume flow rate of exhaust of gas species [L/s], $V_{exp,fac}$: volume expansion factor [L/mol] (At standard temperature, and pressure, the volume occupied by 1 mole of gas is 22.4L, the expansion factor at higher temperatures can be calculated according to the ideal gas law in equation 5.41), $\dot{V}_{flow,tot}$: Total volume flow rate of the exhaust [L/s], $\dot{V}_{air,flow}$: volume flow rate of air inflow into the container [L/s] (which is 0.0258 L/s here [12]), α_{gs}: percentage of individual gas species in the total exhaust coming out of the container[%]

The model results for gaseous exhaust coming out at the top of the container are compared with the lab sintering measurements, and are shown in Figure 5.14.

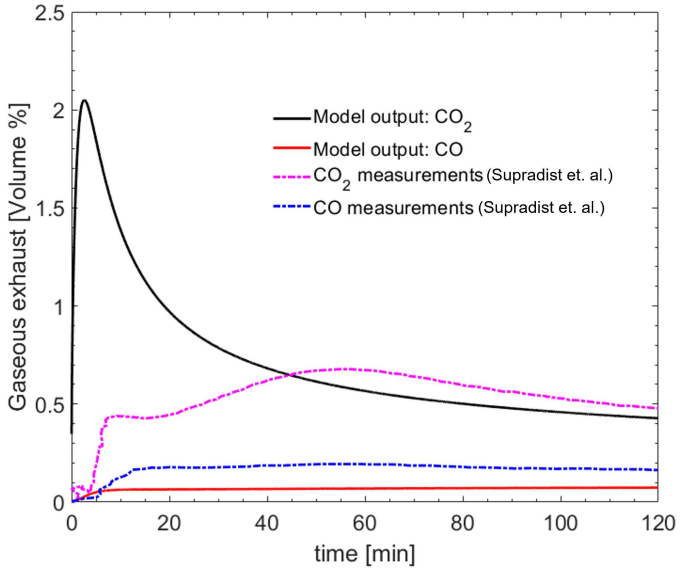

Figure 5.14 Exhaust gas validation with lab sintering measurements

An initial peak of carbon dioxide is observed, due to the exothermic carbon oxidation reaction leading to the formation of carbon dioxide. The volume percent of carbon dioxide released is found to be higher than that of carbon monoxide as Boudouard reaction takes place in a smaller section near the powder bottom. At long times, the volume of gases released as exhaust reaches a near steady-state. There is a reasonably good match between the model prediction and measurements. It is expected that upon including the effect of carbon advection due to powder shrinkage, and improving the current density profile, less carbon will be combusted at the powder bottom, resulting in less CO_2, and CO being released. This will result in better model validation with both the carbon, and off-gas measurements.

The distribution of the different gas species evolves with temperature, time, and chemical reaction rates. The growth rates of all the gas species are presented in Figure 5.15.

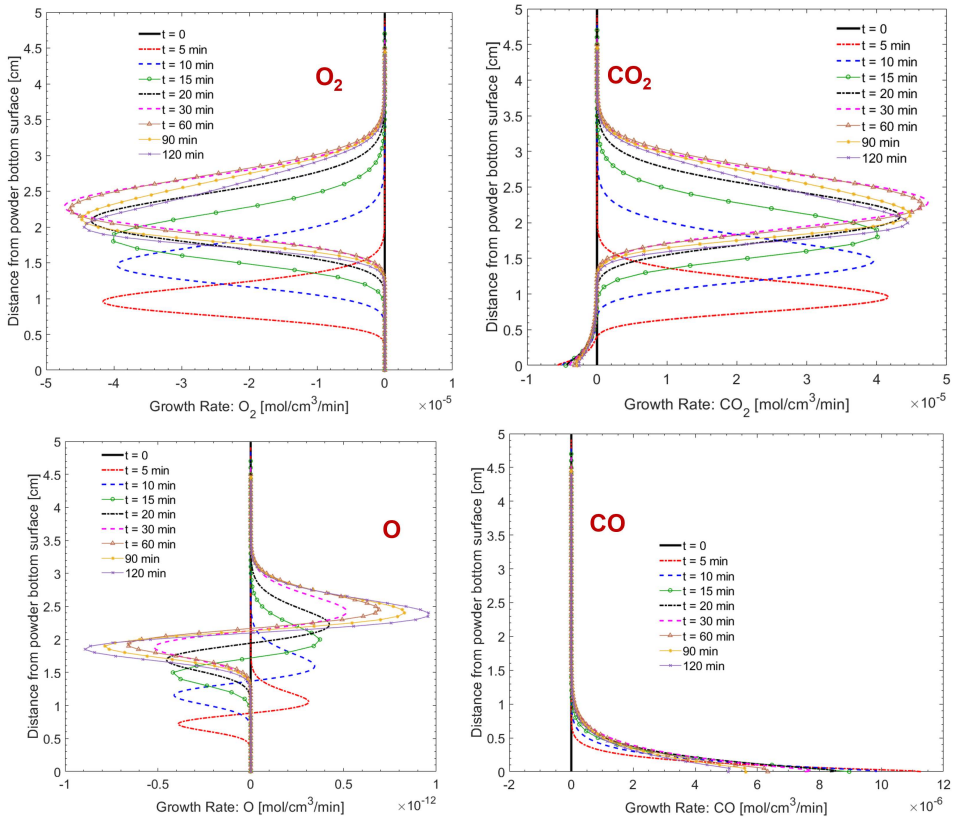

Figure 5.15 Growth rate of gas species in the powder column (a) Oxygen b) Carbon dioxide (c) Atomic Oxygen (d) Carbon monoxide

Oxygen is consumed in the combustion process by reacting with carbon to form carbon dioxide in the powder mid-zone and hence has negative growth rate. On the other hand, carbon dioxide has positive growth rates in the powder mid-zone, but negative rates close to the powder bottom. This is because it is produced by the low-temperature combustion reaction in the powder mid-zone, while it gets consumed by

the high-temperature Boudouard reaction close to the powder bottom. The endothermic Boudouard reaction forms carbon monoxide which has positive growth rates near the bottom. Atomic oxygen is found to have a negative growth rate close to the powder bottom, as here it is consumed by reaction with carbon monoxide to form carbon dioxide. Higher in the powder column, atomic oxygen is produced by the oxidation of carbon monoxide diffusing from the bottom to form carbon dioxide. At short times ($\sim$ 5 min), sharp thermal gradients exist close to the powder bottom which results in high growth rates. As the powder interior begins to heat up, the growth rates of the gases become non-zero, and the curves shift higher in the powder column.

The carbon depletion rate is shown in Figure 5.16. In the powder top region, the temperature is too low for any noticeable combustion to take place. In the powder mid zone, carbon burns, and gets depleted (growth rate < 0) by reacting with oxygen to form carbon dioxide. In the bottom region of the powder (high-temperature zone), carbon combusts (growth rate < 0) by reacting with carbon dioxide to form carbon monoxide (Boudouard reaction). The depletion of carbon is found to be more prominent than the powder bottom region.

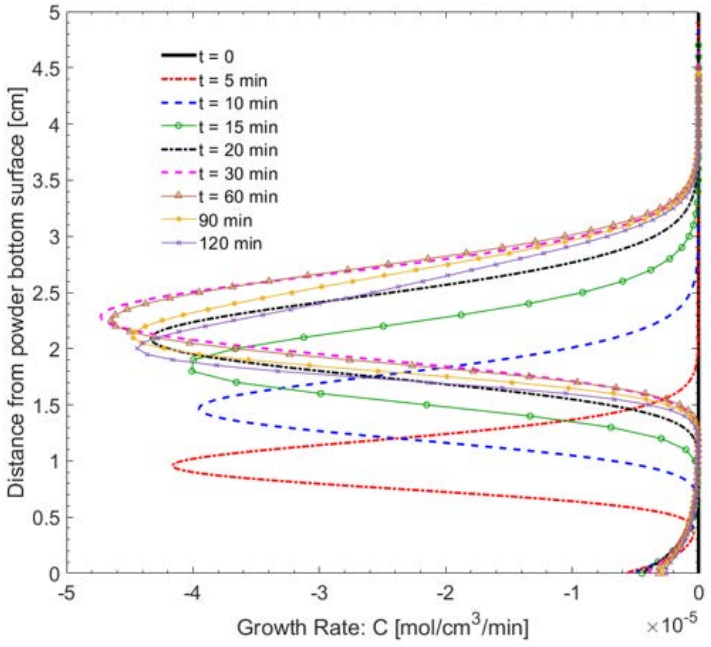

Figure 5.16 Carbon depletion rate

The distribution of oxygen and carbon dioxide in the powder is shown in Figure 5.17.

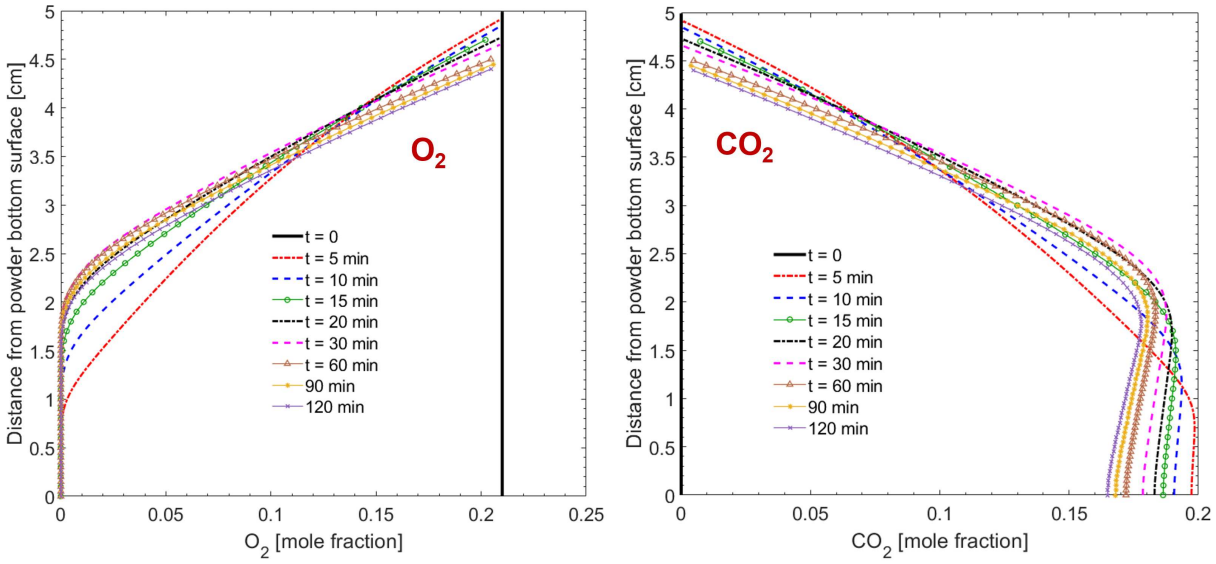

Figure 5.17 Gaseous mole fraction (a) Oxygen b) Carbon dioxide

Oxygen is primarily consumed in its reaction with carbon to form carbon dioxide. So, the amount of oxygen present in the powder gradually decreases. Towards the powder bottom, oxygen runs out fast due to higher temperatures. This 'oxygen-depleted zone' gradually moves up as the powder interior begins to heat up. As we move down from the powder top surface into the powder interior, carbon dioxide mole fraction increases, and reaches a maximum value in the powder mid-zone. Near the bottom region, the mole fraction of carbon dioxide decreases as it reacts with residual carbon to form carbon monoxide according to the Boudouard reaction. Oxygen mole fractions are found to drop from a value of 0.21 at the top cell to near zero at around 1.8 cm after two hours of powder sintering, and reaction. The graph shows an angle at the top indicating the exhaust leaving the domain. Carbon dioxide fractions reach a maximum value of 0.185 at 1.8 cm in the powder column, after which they drop to 0.165 at the bottom surface.

The distribution of carbon monoxide and atomic oxygen is shown in Figure 5.18. As seen in the gas distribution plots, carbon monoxide is formed primarily due to the reaction,r_2, in which carbon dioxide produced by the first combustion reaction, (r_1) diffuses towards the powder bottom, and reacts with available carbon (2 moles of CO formed per mole of carbon and carbon dioxide burnt). Hence, the highest carbon monoxide concentration is found at the bottom and continues to increase with time. Atomic oxygen has the lowest concentration among all the gases and is found to be highest in the powder mid-zone.

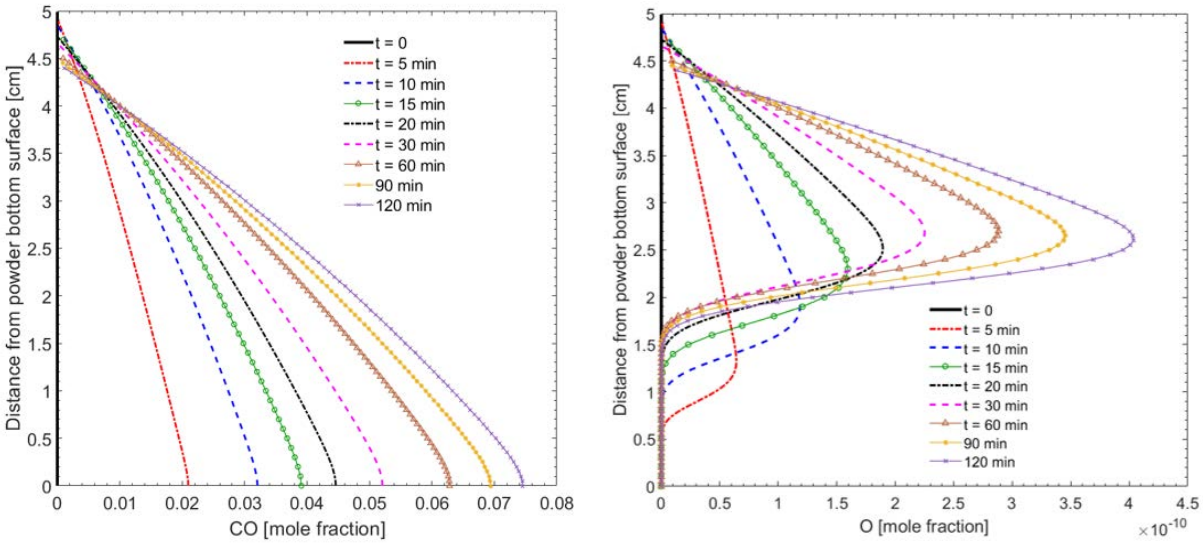

Figure 5.18 Gaseous mole fraction (a) Carbon monoxide b) Atomic oxygen

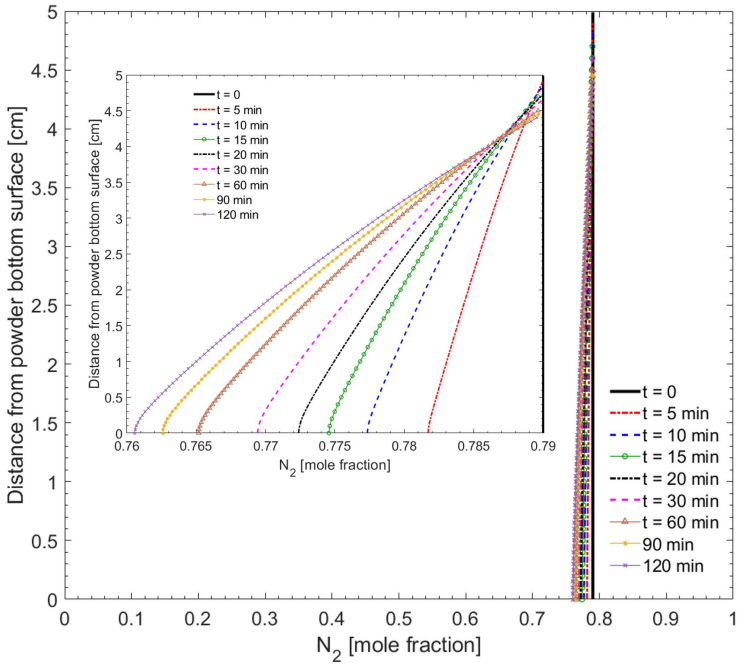

Figure 5.19 Nitrogen gas mole fraction

The gaseous molar distributions are shown in Figure 5.19. Nitrogen being an inert gas doesn't participate in any of the chemical reactions, so its concentration drops by exhaust alone. The important effect of nitrogen is to take up space in the small pores and change the concentration of oxygen and the combustion gases.

As mentioned earlier, the model needs to be improved to account for the downward movement of carbon due to powder shrinkage due to sintering. The effect of shrinkage velocity has been implemented into the model, and the resulting carbon distribution is shown in Figure 5.20.

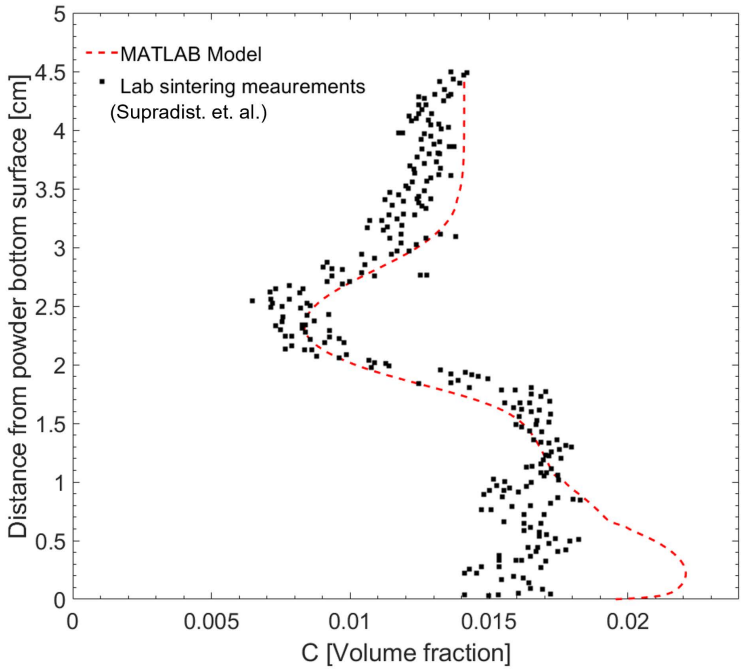

Figure 5.20 New model with effect of carbon advection and accumulation at the powder bottom

The top zone of the powder is too cold to enable the combustion reactions to occur. Oxygen diffusing down from the atmosphere above the powder in the caster reacts with carbon to form carbon dioxide, where the temperature is cooler in the upper powder. Some carbon dioxide diffuses further downwards, and at the higher temperatures near the powder bottom facilitates the formation of carbon monoxide. At intermediate distances, the carbon burns to form a mixture of CO and CO_2. As the gas percolates upwards and cools, CO further decomposes into CO_2. It is observed that carbon accumulates near the powder bottom due to the effect of powder shrinkage resulting in higher carbon concentration than the initial value. The current model over-predicts this accumulation effect, and improving the density profile to have less shrinkage can result in better validation. The model is being improved to have better match with measurements.

CHAPTER 6

TRANSIENT THERMAL MODEL APPLICATION TO CONTINUOUS CASTER

This chapter will present the results of the transient thermal model applied to the continuous caster. The model is run without the effects of sintering, or carbon burning for two commercial plant cases (both thick slab caster with manual addition, and another thick slab caster with semi-automatic addition), and the model is validated for slags for different steel grades such as Ultra-low carbon steel, and Medium carbon Steel. This model has been verified earlier with a commercial package, ANSYS Fluent (as explained in Chapter 4). The results of the simulations here are compared with plant measurements of surface temperature and powder level. The results from the advanced model will be presented in Chapter 7.

6.1 Dofasco Caster with Ultra Low Carbon steel grade (Case 1)

The simple transient model includes the effects of transient heat conduction with temperature-dependent thermal properties, and mass transport to include the important effect of slag consumption, which draws from the liquid slag pool reservoir at the bottom of the domain. Other phenomena, including the effect of sintering on density changes, are implemented into the advanced transfer model and applied in Chapter 7 to improve on the predictions presented in this chapter.

Table 6.1 Casting and model parameters, domain dimensions, properties, and phase transition temperatures for manual powder addition in a thick slab caster with ultra-low carbon steel slag [Case 1]

Properties and dimensions	Value
Total powder/slag thickness, w_{tot}	39.2 mm
Casting speed, v_c	1.2 m/min
Strand Width, W	1.531 m
Strand Thickness, th	0.22 m
Mold Oscillation frequency, f	93*v_c cpm
Oscillation stroke, s	7 mm
Powder consumption rate, Q	72.9 kg/hr
Ambient temperature (top surface)	300 K
Molten steel temperature (bottom boundary fixed temp.), $T_{melt,steel}$	1823 K
Powder Density, ρ_p	1353 kg/m^3
Sinter Density, ρ_s	1976 kg/m^3
Liquid Flux Density, ρ_f	2600 kg/m^3
Advection (consumption) velocity, $v_{cons,f}$	0.023 mm/s
Powder softening temperature, T_{sof}	1368 K
Sinter region temperature, $T_{sinter,mid}$	1387 K
Slag melting temperature, $T_{melt,slag}$	1398 K
Time step size, Δt (calculated by model- final)	$7.9 * 10^{-4}$ s

The model was run for several cases and then compared with several measurements from different steel plants. The first case involves manual powder addition at the commercial thick-slab caster at ArcelorMittal Dofasco. The casting conditions for Case 1 and operating parameters are shown in Table 6.1.

The properties for the first validation case, Case 1, are shown in Figure 6.1(a), and the temperature results are shown in Figure 6.1(b).

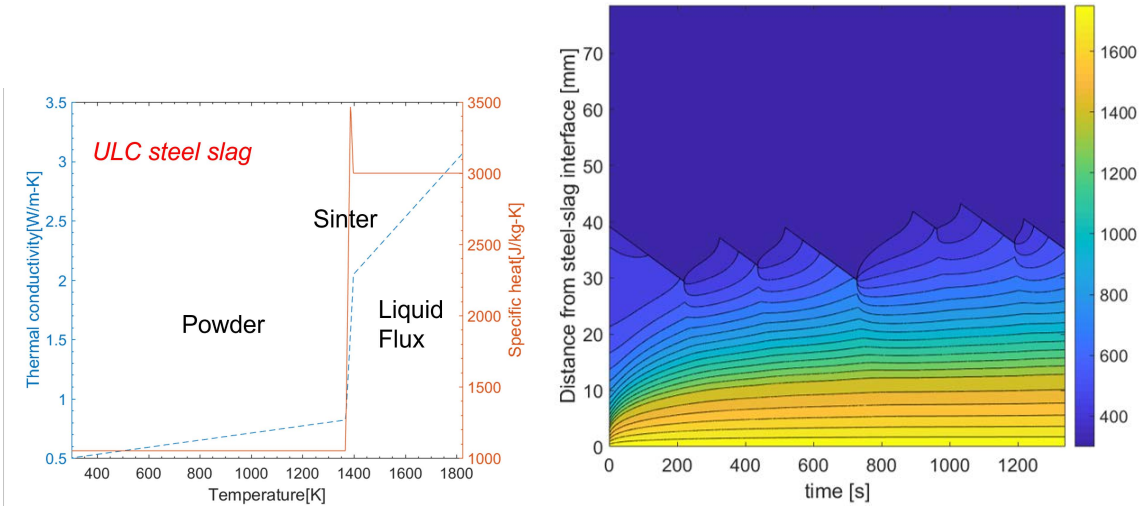

Figure 6.1 Manual Powder addition: Ultra-low carbon steel slag (a) Thermal properties, (b) Temperature contours [Case 1]

The powder surface level changes and evolution of the liquid slag layer thickness are shown in Figure 6.2(a). The resulting powder surface temperatures are presented in Figure 6.2(b). As seen in Figure 6.2(a), the powder level goes up and down during the casting process. Initial average powder thickness (based on the measurement data) and steady-state temperature distribution (from the in-house steady-state model) are applied as the initial condition before the simulation starts. As the casting process proceeds, liquid flux is consumed from the liquid slag layer (as a mass sink) and enters into the gap between the solidifying shell and the water-cooled copper mold. This results in a steady drop in the powder level between each powder addition, where the level jumps quickly. As the powder level lowers, heat conduction effects are enhanced, which in turn results in powder melting and growth and build-up of the liquid flux layer.

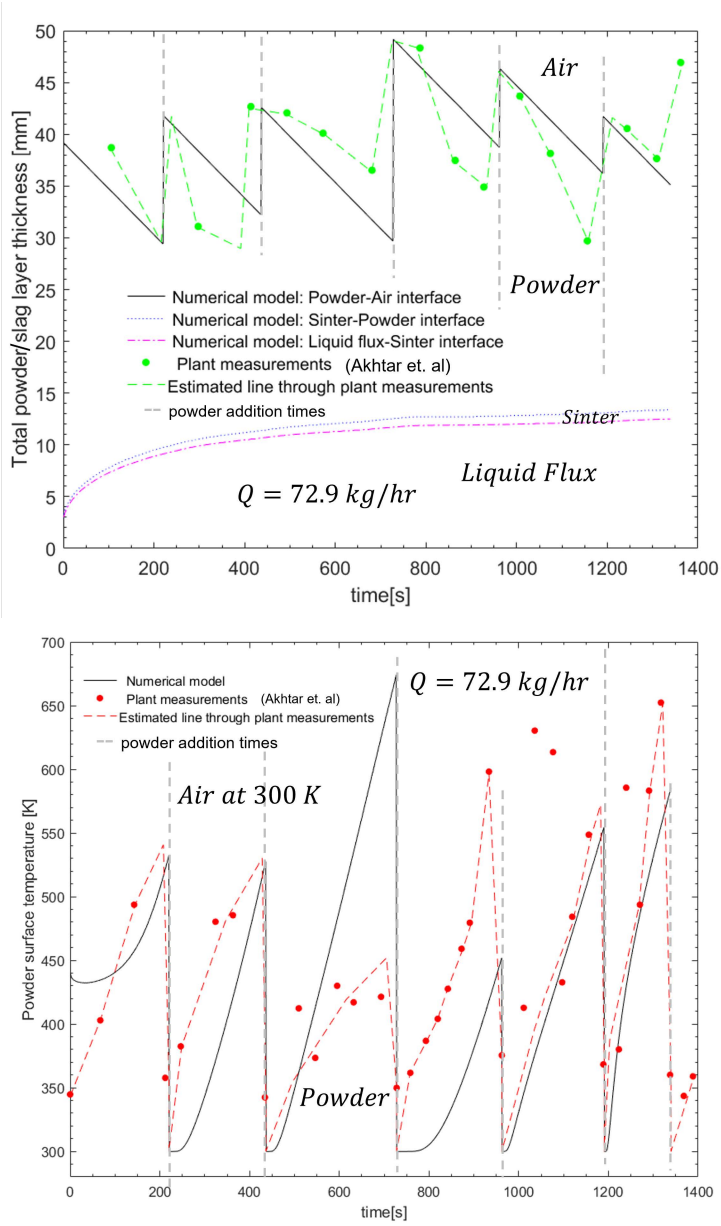

Figure 6.2 Manual Powder addition: Ultra-low carbon steel slag (a) Powder/slag thickness (b) Powder surface temperatures [Case 1]

When the powder addition takes place, this results in a sudden drop in the surface temperature since cold powder at room temperature is added. To account for this in the model, the temperature of the region of the domain with the newly added powder is fixed at 300K whenever this powder addition event occurs, according to the plant measurements. As casting continues, the powder heats up again, and the liquid slag layer keeps building. The model input considers a sufficient time frame to cover about five powder addition cycles so that a reasonable validation with plant measurements can be made. A reasonable match is

obtained between the model predictions and plant measurements of powder surface temperatures. The powder addition heights are input to the model based on the plant measurements, whereas the temperatures including the surface temperature, powder height drops after addition, and liquid flux levels are all predicted by the model. Note that the dotted line is drawn between the measured points, but is not drawn using simple line segments in order to account for the expected missing details in the temperature history near when the new powder is added.

When cold powder is added, the surface temperature naturally drops to 300K. The time duration for the powder top surface to begin to heat up at the beginning of every addition cycle has a linear relationship with the amount of powder added (Figure 6.3). The target temperature considered while measuring the delay in the time to start powder heating is 315 K. In the figure, powder addition in the x-axis corresponds to the difference between the total mold powder added and the powder-air interface level just before addition for each of the last 5 measured additions in Figure 6.3.

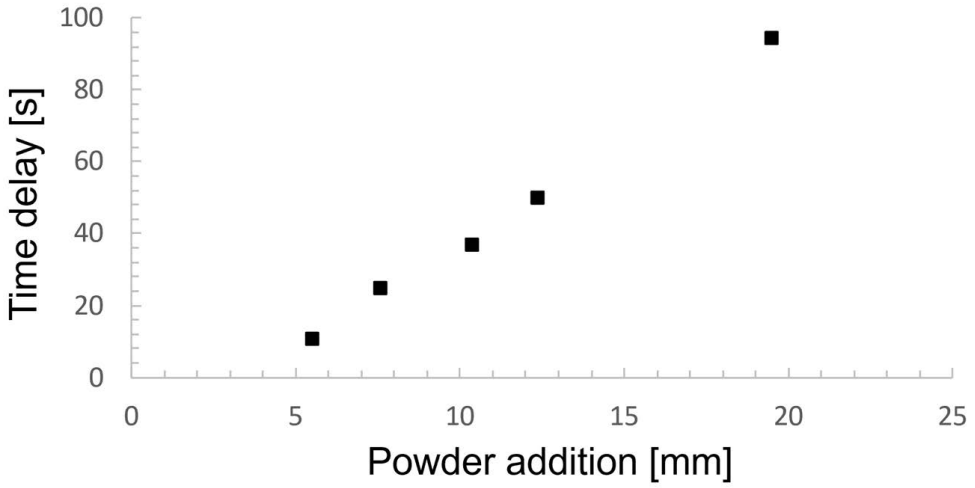

Figure 6.3 Time delay in powder heating [Case 1]

For this plant, manual powder addition occurred at certain times when the operator noticed red spots (high-temperature zone) at the powder top surface. The operators generally add bags of mold powder in order to avoid these red spots. There is no quantitative determination of how much powder should be added at what times. The lack of this quantitative knowledge is one of the underlying motivations for building this model. Most plants generally operate a "black" practice, such that the mold powder temperatures remain below the visible threshold where the color becomes visible. This is done so that sufficient powder thickness is maintained, which in turn upon melting keeps the liquid flux thickness in a

reasonable range.

6.2 Dofasco Caster - Medium Carbon steel grade (Case 2)

The model is also validated with measurements for a medium-carbon steel slag at Dofasco. The casting conditions and operating conditions are shown in Table 6.2.

Table 6.2 Casting and model parameters, domain dimensions, properties, and phase transition temperatures for manual powder addition in a thick slab caster with medium carbon steel slag [Case 2]

Properties and dimensions	Value
Total powder/slag thickness, w_{tot}	35.9 mm
Casting speed, v_c	1.3 m/min
Strand Width, W	1.575 m
Strand Thickness, th	0.22 m
Mold Oscillation frequency, f	93*v_c cpm
Oscillation stroke, s	7 mm
Powder consumption rate, Q	68.2 kg/hr
Ambient temperature (top surface)	300 K
Molten steel temperature (bottom boundary fixed temp.), $T_{melt,steel}$	1823 K
Powder Density, ρ_p	1353 kg/m^3
Sinter Density, ρ_s	1976 kg/m^3
Liquid Flux Density, ρ_f	2600 kg/m^3
Advection (consumption) velocity, $v_{cons,f}$	0.021 mm/s
Powder softening temperature, T_{sof}	1193 K
Sinter region temperature, $T_{sinter,mid}$	1276 K
Slag melting temperature, $T_{melt,slag}$	1348 K
Time step size, Δt (calculated by model- final)	$7.1 * 10^{-4}$ s

The thermal contours show the powder level changes and temperature distribution for Case 2 in Figure 6.4.

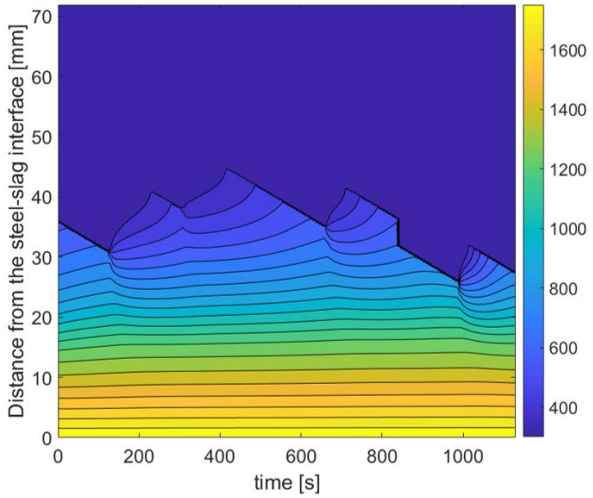

Figure 6.4 Temperature contours [case 2]

The trends between powder additions are similar to the previous case. But, one deviation to note in particular is that, generally during the special powder addition times, the measured powder level is higher compared to the value before the event. But for this case (around $850s$), the powder level is found to drop suddenly (Figure 6.5 (a)). This probably happened as the operator may have moved some powder away from the small region being measured. This increased the temperature of the powder drastically, as the powder in the interior is closer to the steel meniscus and much hotter as compared to the powder surface.

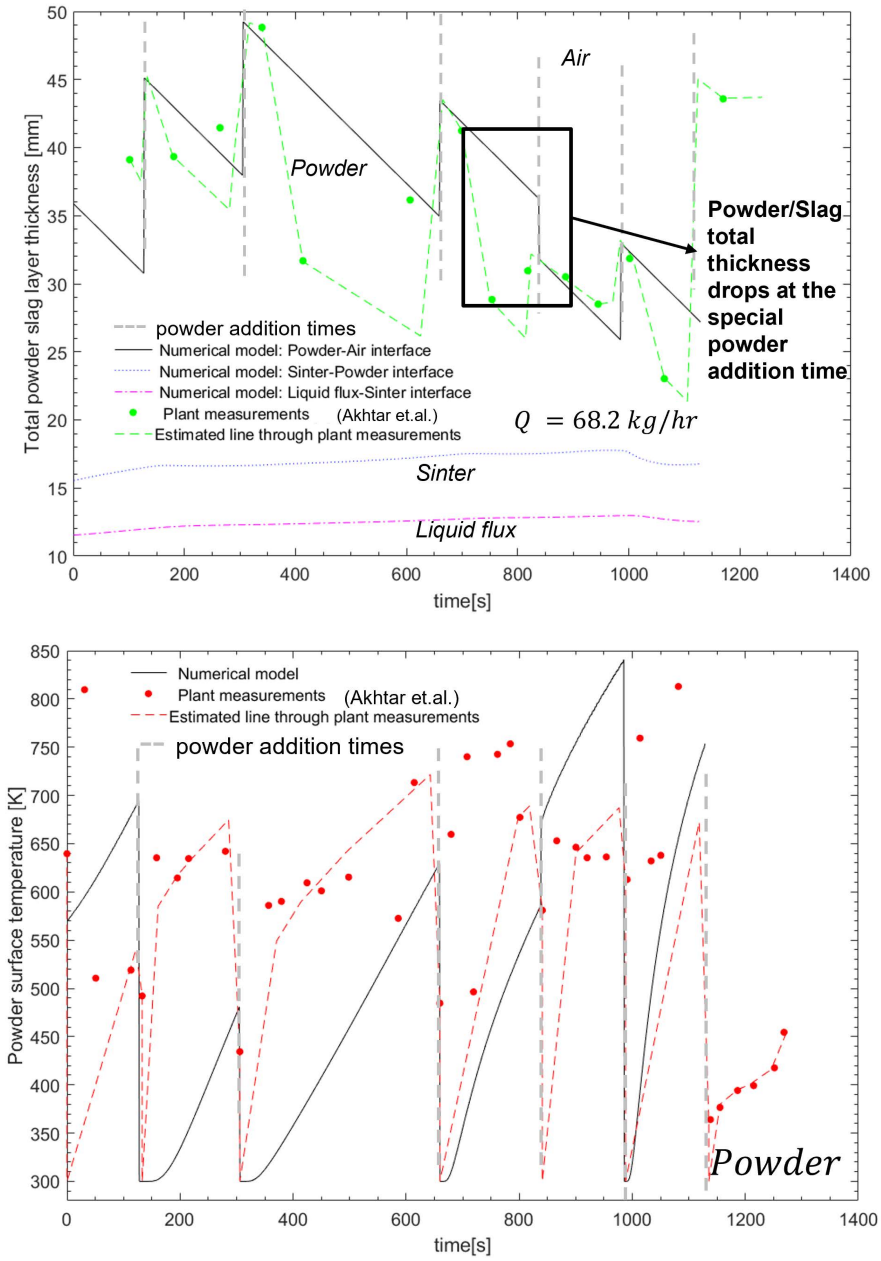

Figure 6.5 Manual Powder addition: Medium carbon steel slag (a) Powder/slag thickness b) Powder surface temperatures [Case 2]

The temperatures (Figure 6.5 (b)) are observed to be higher than in the previous case, due to lower average powder thickness, different property functions, and phase transition temperatures. The plant also reported that flashing (visible red-hot zones) was observed during casting for this case. The model exhibits the same trend as the plant measurements, and there is also a good quantitative match.

6.3 TATA Caster-Medium Carbon steel grade (Case 3)

The model was next validated with another caster at a different steel plant. The plant measurements for this thick slab caster are shown in Figure 6.6(a), and the model properties are shown in Figure 6.6(b).

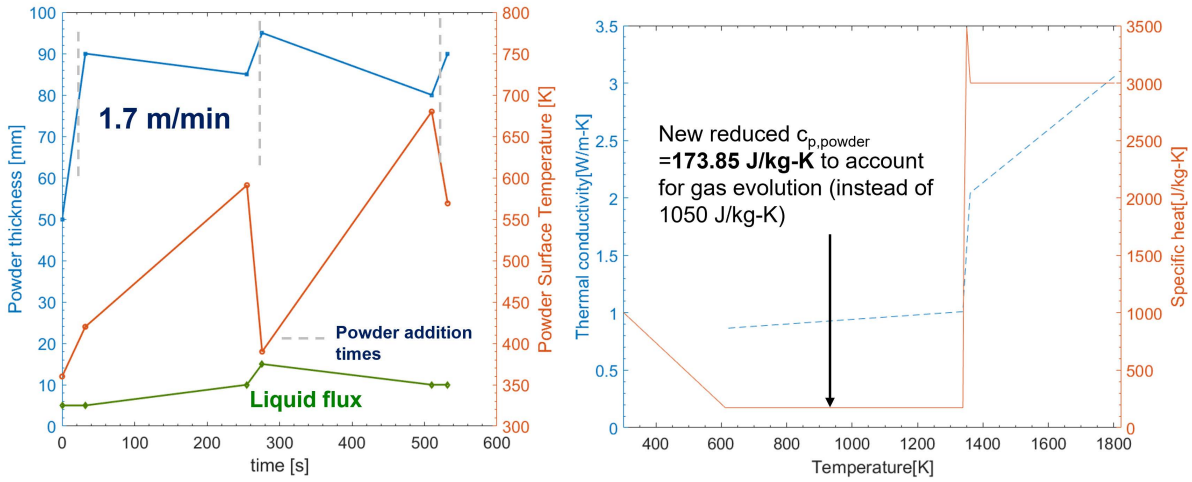

Figure 6.6 Continuous powder addition (a) Plant measurements of powder thickness and surface temperature b) Model Thermal properties [Case 3]

In this plant, continuous powder addition (semi-automatic) takes place through four tubes with valves, which work intending to provide a near-homogeneous powder distribution. The powder might create a hump at the location where it is released, but then gradually spreads out to attain a near-flat profile. Even though there is continuous powder addition, since the powder lump added has to spread out, the effective behavior is similar to intermittent addition as seen from the measurements. So, an auto-feed correction time of 250s is observed in the measurements when the powder top surface gets re-set due to the powder spreading out. One thing to note is that the powder and liquid flux levels vary along the strand cross-section in the plant, and our 1-D model can only make predictions at one location per run.

The casting conditions and other operating parameters are shown in Table 6.3.

Table 6.3 Casting and model parameters, domain dimensions, properties, and phase transition temperatures for continuous powder addition in a thick slab caster [Case 3]

Properties and dimensions	Value
Total powder/slag thickness, w_{tot}	90.83 mm
Casting speed, v_c	1.7 m/min
Strand Width, W	1.2 m
Strand Thickness, th	0.232 m m
Mold Oscillation frequency, f	100*v_c cpm
Oscillation stroke, s	7 mm
Powder consumption rate, Q	82.89 kg/hr
Ambient temperature (top surface)	300 K
Molten steel temperature (bottom boundary fixed temp.), $T_{melt,steel}$	1802 K
Heat Transfer coefficient, h_{tot}	29.62 W/m^2K
Powder Density, ρ_p	1353 kg/m^3
Sinter Density, ρ_s	1976 kg/m^3
Liquid Flux Density, ρ_f	2600 kg/m^3
Advection (consumption) velocity, $v_{cons,f}$	0.032 mm/s
Powder softening temperature, T_{sof}	1339 K
Sinter region temperature, $T_{sinter,mid}$	1350 K
Slag melting temperature, $T_{melt,slag}$	1361 K
Time step size, Δt (calculated by model- final)	$5.74 * 10^{-4}$ s

Similar trends are observed for Case 3 as in the previous two cases as shown in Figure 6.7. The powder surface drops (Figure 6.7(a)) due to liquid flux consumption and goes back up during addition times (when the lump of fresh powder added gradually spreads out). The liquid flux thickness is over-predicted by the model, which is expected to be improved by considering all the combustion physics in the multiphysics model (See Chapter 7). The surface temperatures increase when the powder height goes down, and when cold powder comes in contact with the measurement spot, the temperature drops to ambient temperature. The temperature prediction (Figure 6.7(b)) looks good for the first cycle but is low for the second cycle. But, there are also very few measurements for this case, so having more measurements for this case, might result in better validation.

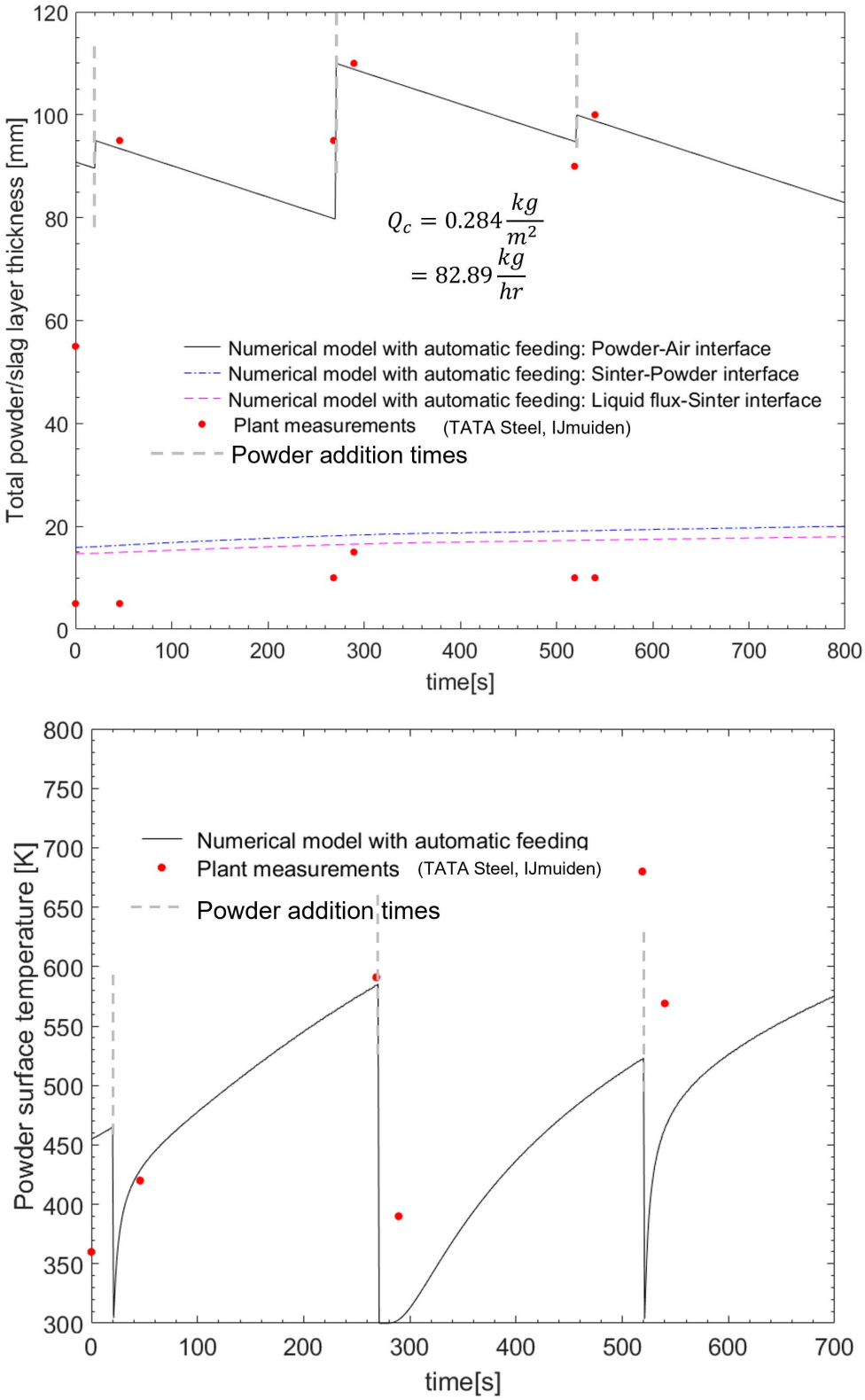

Figure 6.7 Continuous powder addition (a) Powder/slag thickness (b) Powder surface temperatures [Case 3]

6.4 Manual versus Automatic Feeding

The simple transient model has been validated with several plant cases, including a typical plant that prefers to add their mold powder manually (bags of powder) at intermittent times, and at another plant, that adds their powder in a continuous/semi-continuous manner. Some plants such as Voestalpine in Austria even have an advanced system of imaging the powder surface level, and continuously monitoring their powder height. Therefore, it is important to analyze the different types of powder addition and understand how the particular style of addition affects the powder and liquid slag thickness, and powder temperature, which in turn affects steel quality.

In this particular section, the model simulates both automated and manual powder feeding mechanisms and compares the results of powder/slag height, and surface temperature. For this study, a typical auto feed correction time scale of 10 s is used, when a robotic feeder passes by the local spot, and resets the powder level to a target value. The powder level and corresponding predicted surface temperature histories are shown in Figure 6.8.

Using an automated powder feeder helps in maintaining a near-constant powder/liquid pool height. A thicker liquid pool is observed for the current automated feeder case, especially at initial times relative to the manual feeder case. This is because the powder is thicker on average with automated feeding, which insulates the liquid flux layer, enabling it to melt powder at a faster rate. Surface temperatures recorded for the manual feeding case are higher due to (i) Lower total powder/slag thickness leading to less resistance to conduction through the layers and higher heat losses from the surface (ii) More time between powder additions for the slag to heat up (since cold powder is added at 300K). It is observed that relatively stringent control of powder surface temperatures/level is possible through automatic feeding since manual addition is not consistent about powder addition time intervals and powder addition amount.

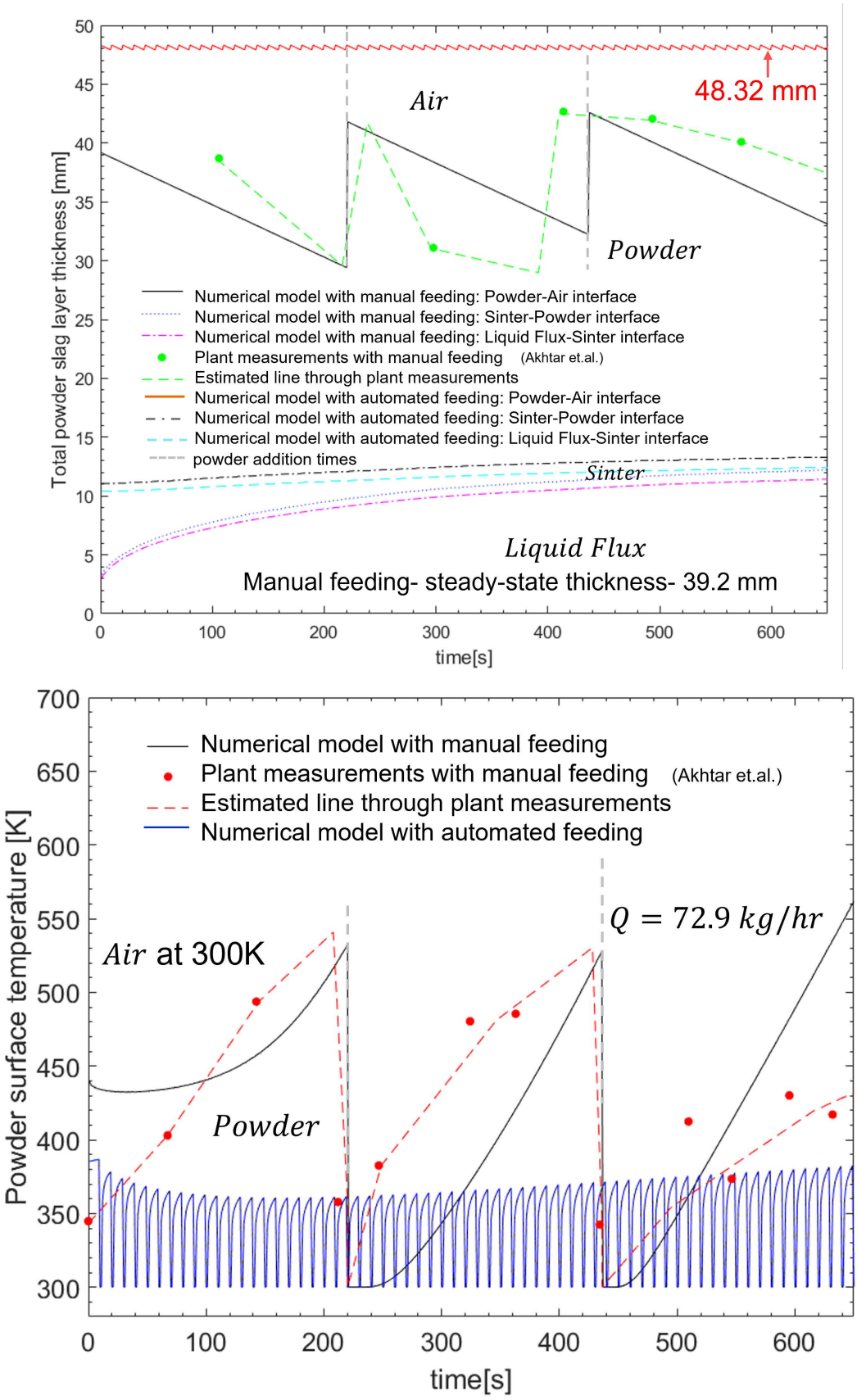

Figure 6.8 Comparison of Manual [Case 1] and Automated feeding [Case 1a] (a) Powder/slag thickness (b) Powder surface temperatures

6.5 Parametric Studies

Next, parametric studies were done to understand the effects of carbon content, packing ratio, and liquid flux consumption rate. For the runs with varying carbon content (Figure 6.9), a reduced specific heat approach was considered to account for the exothermic reactions taking place during carbon combustion. Starting with Case 1, the specific heat was lowered from 1050 J/kgK to 708.3 J/kgK, and carbon content was 1.6%, of which 50% was considered to be burnt. The carbon-burning temperature range was considered to be 600K-1368K. Other conditions are the same as given in Table 6.1.

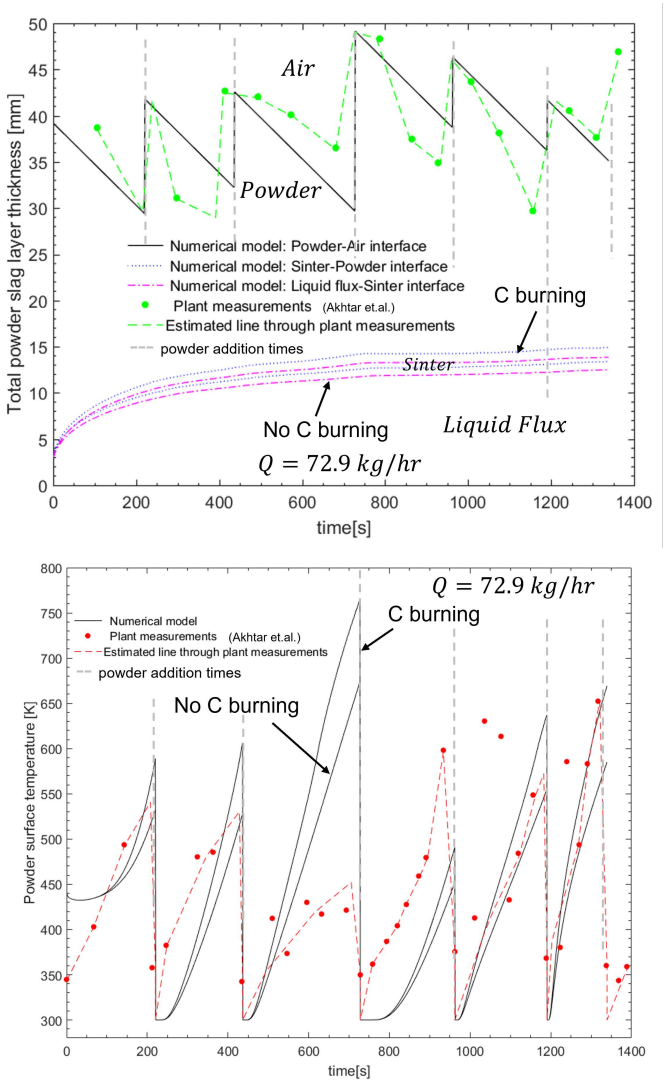

Figure 6.9 Parametric study on the effect of carbon content (a) Powder/Slag thickness (b) Powder surface temperature

This was done to verify that the model can predict expected trends for varying conditions. Including this effect increased the predicted temperatures as expected (due to the heat released during combustion), which in turn resulted in the formation of a deeper liquid flux melt pool (Figure 6.9). This indicates a slightly faster melting rate. As mentioned in the literature review, increasing carbon actually decreases the melting rate observed in the commercial operations. This is because carbon has an important slowing mechanism: by separating the powder particles which slows down the sintering process which overcomes this increase due to combustion.

For the packing ratio study, packing ratios based on body-centered cubic, face-centered cubic, and simple-cubic crystal structures were considered. Larger drops in powder levels were observed for the lowest-density, highest-porosity simple cubic case (as more pore spaces were available to be eliminated) which resulted in higher powder temperatures (Figure 6.10).

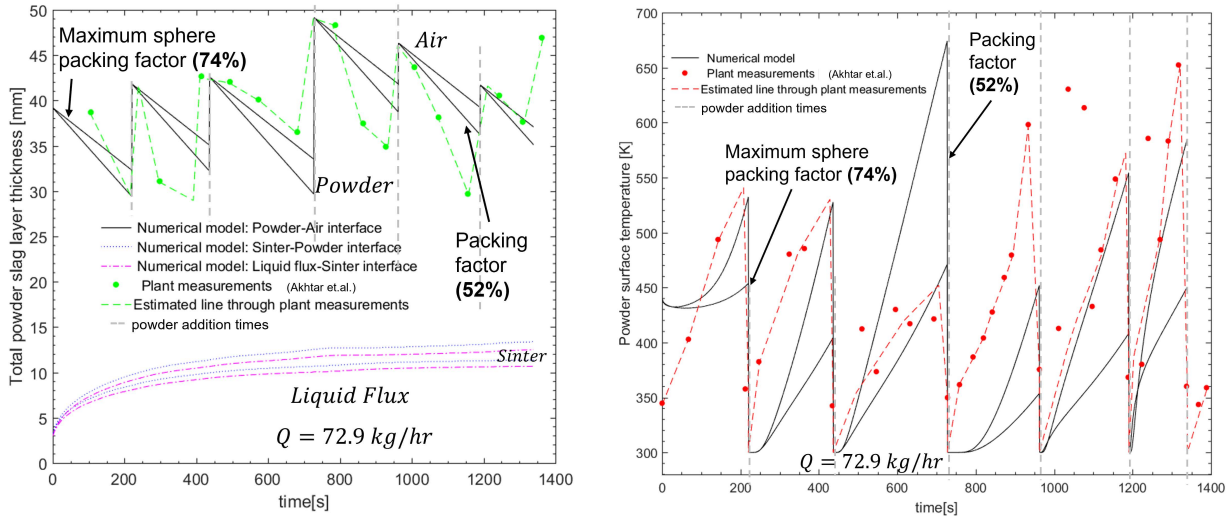

Figure 6.10 Parametric study on the effect of powder packing density (a) Powder/slag thickness (b) Powder surface temperatures

Similarly, higher flux consumption is also naturally predicted to cause greater drops in powder levels, resulting in shallower liquid flux layer thickness (Figure 6.11). The liquid flux leaving the domain advects heat along with it, so higher flux consumption leads to lower surface temperatures. In summary, the simple transient model predicts expected thermal behavior of the powder and liquid flux layers in the continuous casting process.

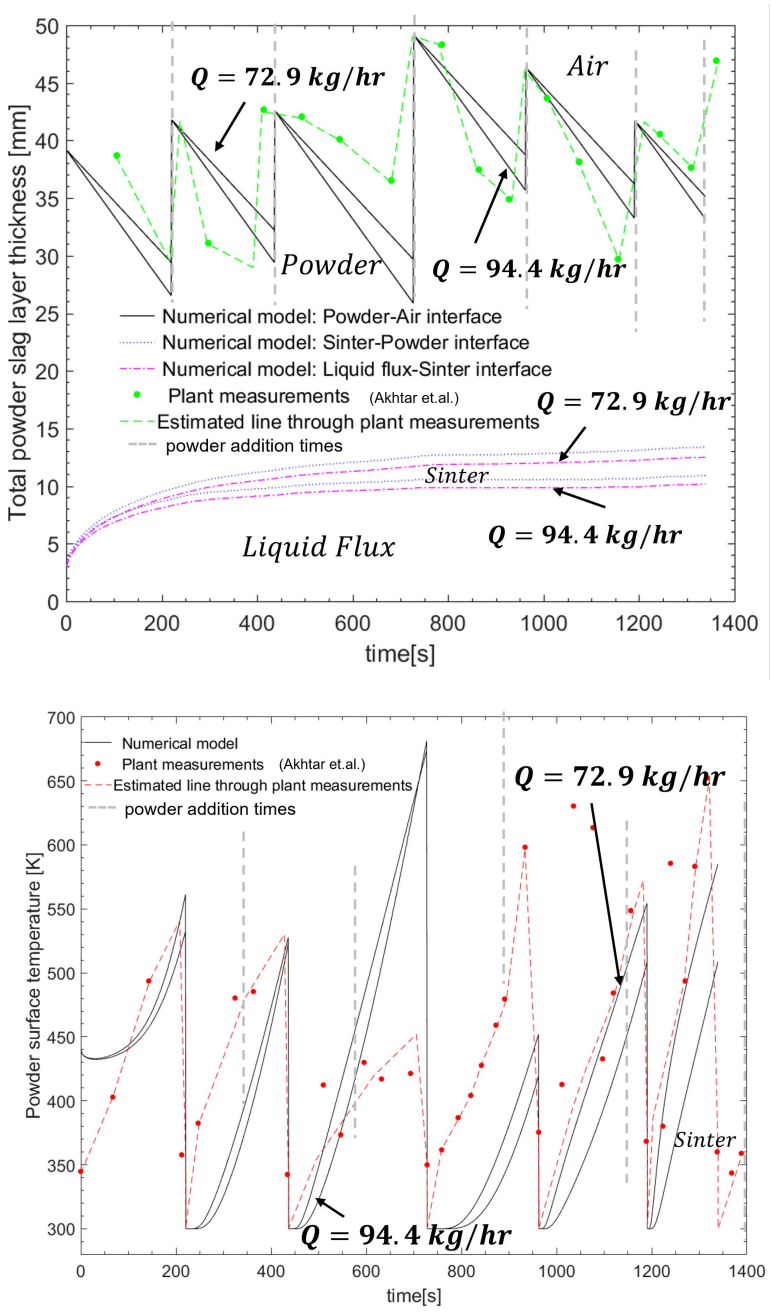

Figure 6.11 Parametric study on effect of flux consumption (a) Powder/slag thickness (b) Powder surface temperatures

CHAPTER 7

MULTI-PHYSICS MODEL APPLICATION TO CONTINUOUS CASTER

The multi-physics model described in Chapter 5 has been applied to the continuous caster. The complete model with the heat, and mass transfer, powder sintering behavior, carbon combustion, gas diffusion, and transport is simulated for the continuous caster at Dofasco plant, and the results are compared with plant measurements. It is highly effort-intensive, and expensive to measure the carbon and gas distribution through the powder/slag layers in an actual caster. So, the powder surface temperatures, and surface level measurements are used to validate the results of the multi-physics model. The results presented here include certain simplifications specifically, neglecting the effect of carbon advection in downward direction towards the powder bottom (along gravity), which would likely result in carbon accumulation at the bottom of the sinter layer. This simulation also neglects the effect of shrinkage velocity which would have likely caused a drop in powder height (in addition to powder level going down due to liquid slag consumption at the domain bottom), and carbon advection.

In comparison to the lab sintering experiment, this case is more advanced because the multi-physics model applied here also considers the presence of a liquid flux layer, which is constantly evolving due to heat transfer from the molten steel resulting in powder melting. This simulation also includes a liquid flux consumption velocity to incorporate the effect of liquid flux leaving the domain to lubricate the gap between the solidifying shell and copper mold. It is important to note that all the chemical reactions described in the multi-physics model (Chapter 5) are assumed to occur only in the powder/sinter layer. No gas diffusion or combustion is considered in the liquid flux layer. These assumptions are reasonable as the gasses and carbon required for these reactions have low density, and hence can't penetrate the flux layer. The carbon tends to float on top of the molten flux layer, where it accumulates with time. The gases considered in this study are also less likely to diffuse into the molten flux layer. Some small amounts of every gas can diffuse into the liquid flux layer. But, the concentrations are so low, that the reactions can be neglected.

Even though H ions being small can diffuse faster, there is so little H added, so the effective concentration of hydrogen will be low. H is detrimental because it creates H gas bubbles and porosity in the liquid slag layer in the gap, which lowers interfacial heat transfer, and in severe cases, causes a breakout (many plants have had big problems with breakouts caused by hydrogen).

As a result of heat and mass transfer, the powder level changes greatly with time, due to the combined effects of powder addition, liquid flux consumption, powder melting, sintering, density increase, and shrinkage. The shrinkage velocity model and the powder height drops due to shrinkage have been neglected

in the initial runs of the multiphysics model application to the continuous caster. The sinter-liquid slag interface and the powder-air interface move up and down as a result of energy balance, mass balance, sintering, and phase transition. Therefore the height of the powder-sinter region between these two interfaces is continuously changing, and so is the zone of sintering, carbon, and gas computation. Carbon and gas can't diffuse into the liquid flux layer, and the zone to the top of the powder top surface is filled with air and is at ambient temperature, so to save computational time, these equations are not solved in the air layer, or in the molten slag layer. The multiphysics model is applied to Case 1, and the casting conditions are presented in Table 7.1.

Table 7.1 Casting and model parameters, domain dimensions, properties, and phase transition temperatures for manual powder addition in a thick slab caster with ultra-low carbon steel slag [Case 1]]

Properties and dimensions	Value
Initial powder/slag thickness, $w_{tot,0}$	39.2 mm
Casting speed, v_c	1.2 m/min
Strand Width, W	1.531 m
Strand Thickness, th	0.22 m
Mold Oscillation frequency, f	93*v_c cpm
Oscillation stroke, s	7 mm
Powder consumption rate, Q	72.9 kg/hr
Ambient temperature (top surface)	300 K
Molten steel temperature (bottom boundary fixed temp.), $T_{melt,steel}$	1823 K
Cold Powder Density, ρ_p	620 kg/m^3
Fully Sintered Density, ρ_s	2700 kg/m^3
Liquid Flux Density, ρ_f	2600 kg/m^3
Liquid slag consumption velocity, $v_{cons,f}$	0.023 mm/s
Sinter region temperature, $T_{sinter,mid}$	1387 K
Slag melting temperature, $T_{melt,slag}$	1398 K
Time step size, Δt (calculated by model- final)	$6.47 * 10^{-6}$ s

7.1 Transient heat transfer results

The model is applied to the thick slab caster at Dofasco plant with ultra-low Carbon steel slag, where powder is added intermittently. This section will discuss the temperature distribution through powder/slag layers. The powder thermal properties and temperature contours are shown in Figure 7.1.

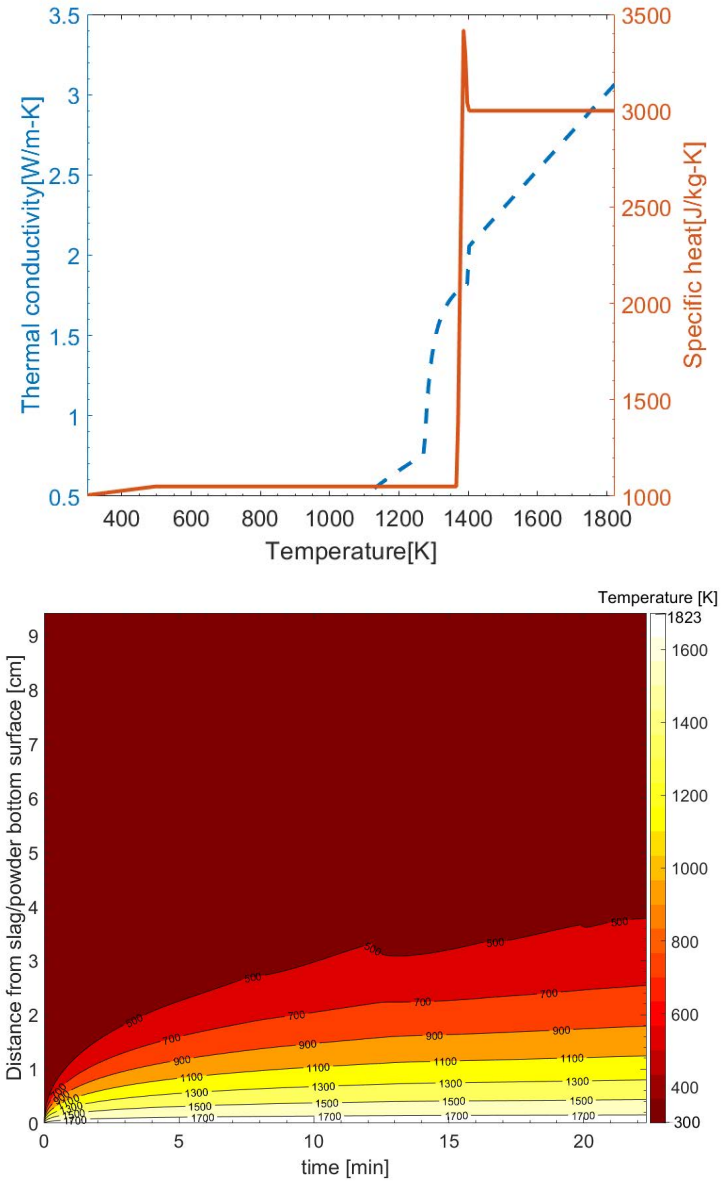

Figure 7.1 Powder/slag (a) Thermal properties (b) Temperature contours

The temperature naturally increases towards the domain bottom (molten steel-slag interface). Molten steel temperature is considered to be 1823 K for this case. The powder/slag level and surface temperature are shown in Figure 7.2.

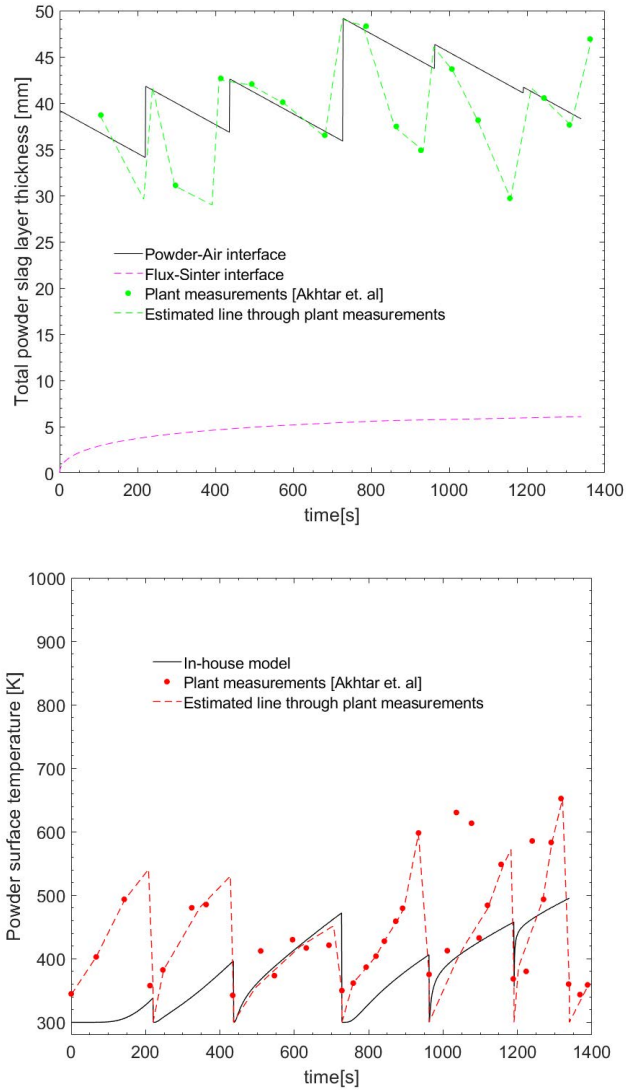

Figure 7.2 Model validation (a) Powder/slag thickness (b) Powder surface temperature

The powder top surface rises at powder addition times and falls continuously due to liquid flux consumption at domain bottom. Since the model is initialized with all cold powder (at 300K) to simulate the caster startup condition, there is no molten slag to begin with, but gradually as the powder heats up and melts, the liquid slag layer evolves. Since the effect of shrinkage velocity is neglected for this run, the powder layer doesn't exhibit the necessary drop due to powder shrinkage. In Figure 7.2 (b), we see the surface temperature rises due to higher conduction heat flux during flux consumption (as powder at the top falls and moves closer to higher temperatures when flux is removed). The temperature is reset to ambient temperature during powder additions as cold powder gets added to the top surface of the remaining powder in the mold. The temperatures are low compared to the measurements, but including

the shrinkage velocity effect is expected to result in more drop in powder heights, and thereby increase the surface temperature resulting in better match with measurements.

7.2 Powder Sintering results

The multiphysics model considers the effect of powder sintering, and densification with powder heating, and sintering time. At higher temperatures and longer times, the powder particles get more closely packed, thereby reducing pore spaces (both internal and external) resulting in higher density. The sintering kinetics results are seen in Figure 7.3. As seen in Figure 7.3(a), powder density increases with distance (and time) from the top surface towards the domain bottom, as sintering progresses.

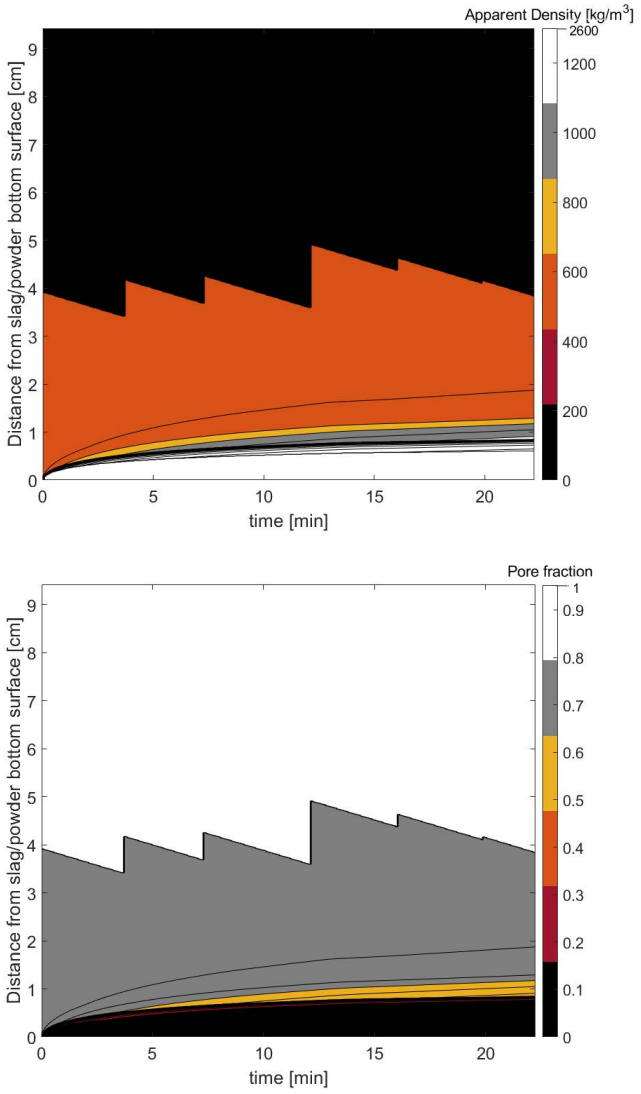

Figure 7.3 Powder sintering behavior (a) Density contours (b) Pore fraction contours

As we move down from the powder top surface, the density increases, due to higher temperatures, where sintering increases. So, the liquid slag layer at the domain bottom has the highest density. On the very top, we have air which has a low density of 1.225 kg/m^3. The amount of air in the domain changes based on the total powder/slag levels. In Figure 7.3(b), we see that cold powder at the top has a lot of porosity (77%), and as it moves down in the powder layer due to flux consumption, the pore spaces decrease as sintering progresses. At the very bottom, molten slag is present which is considered to have zero porosity.

7.3 Carbon and gas distribution results

The carbon and oxygen variation through the powder/slag layers predicted by the model are shown in Figure 7.4.

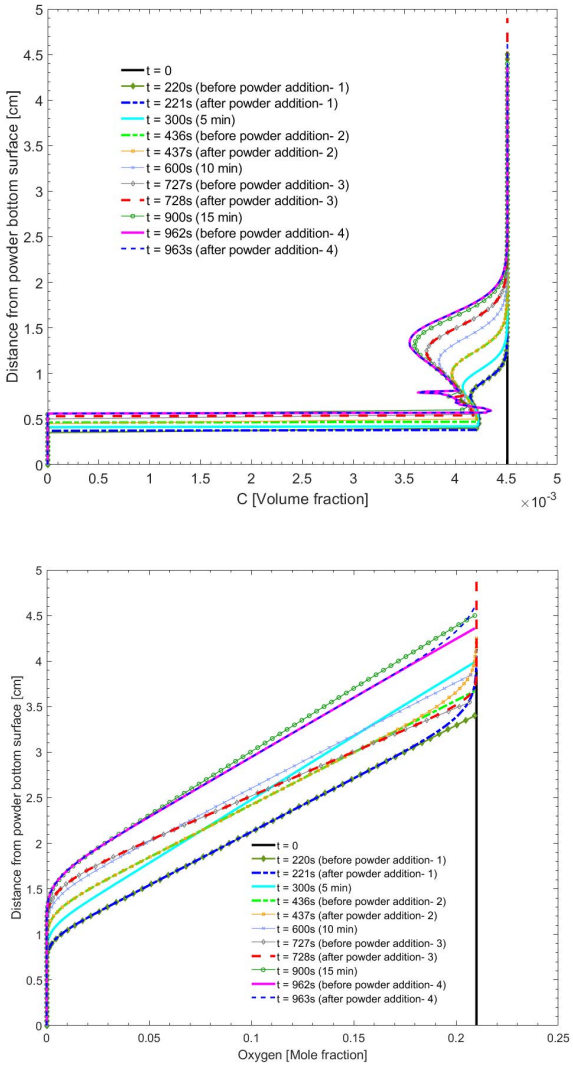

Figure 7.4 (a) Carbon volume fraction (b) Oxygen mole fraction showing the powder addition times

In the powder-top region, the temperature is too low for combustion reactions to occur, therefore the carbon content remains at the initial value. As we move a bit deeper into the powder column, carbon begins to combust by reacting with oxygen present in the pore space and reaches a minimum (Figure 7.4(a)). Once, available oxygen runs out, the carbon burning rate slows, and residual carbon content goes up. Close to the sinter-liquid slag interface, the temperatures are too high for CO_2 formation and promote Boudouard reaction to convert CO_2 into CO, which results in some more carbon burning. In the liquid slag layer at the domain bottom, no carbon is present, as carbon due to its being lighter than molten flux, cannot penetrate the slag layer, and keeps floating on top of the flux layer.

In Figure 7.4(b) at the powder top surface, we see that oxygen concentration is the same as ambient concentration, and moving down through the powder layer, the oxygen is consumed due to the carbon-burning gas reactions. Towards the powder bottom, since the temperatures are very high, the reactions are very fast, so almost all oxygen is used up (a low equilibrium concentration remains). At the very bottom up to ~ 0.5 cm, there is a molten flux layer, and since gas cannot diffuse into the slag layer, the oxygen concentration remains zero below the bottom of the sinter layer (i.e. the sinter layer/molten slag interface). The slopes at the powder top show that some oxygen is leaving the top surface as gaseous exhaust. It is important to note that the powder level jumps after every powder addition. Each time fresh powder is added, it brings new oxygen to the powder layer, which starts reacting once the powder heats up.

The nitrogen distribution through the powder/slag layer is shown in Figure 7.5. Nitrogen is an inert gas, so does not react with carbon, or other gases, but it advects, and diffuses, and is also released as exhaust.

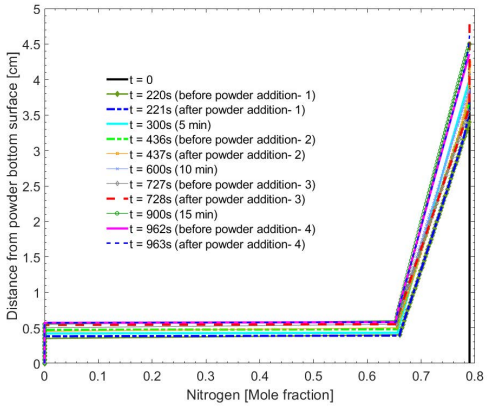

Figure 7.5 Nitrogen mole fraction showing the powder addition times

When the powder heats up, the gases expand, and can no longer remain confined in the available pore space if a constant pressure is maintained. Therefore gas gets released as exhaust, and that is why nitrogen content decreases as we move deeper in the powder towards high-temperature zones. As explained before,

like other gases, nitrogen cannot diffuse into the molten flux layer, so nitrogen concentration in the slag layer is zero.

The carbon dioxide and carbon monoxide mole fraction distributions are shown in Figure 7.6. In the top half of the powder, carbon dioxide is formed by the reaction of carbon with oxygen. Therefore, the CO_2 mole fraction is found to increase with distance below the top powder surface until we reach a critical distance in the powder mid-zone. In the lower half of the powder, CO_2 decreases as it is consumed by the reactions with carbon via the endothermic Boudouard reaction to form carbon monoxide. The powder heights rise after each addition depending on the amount of powder added, and the carbon concentration in this newly added layer is the same as the carbon concentration of cold powder at room temperature. The gas concentration is zero in the liquid flux layer.

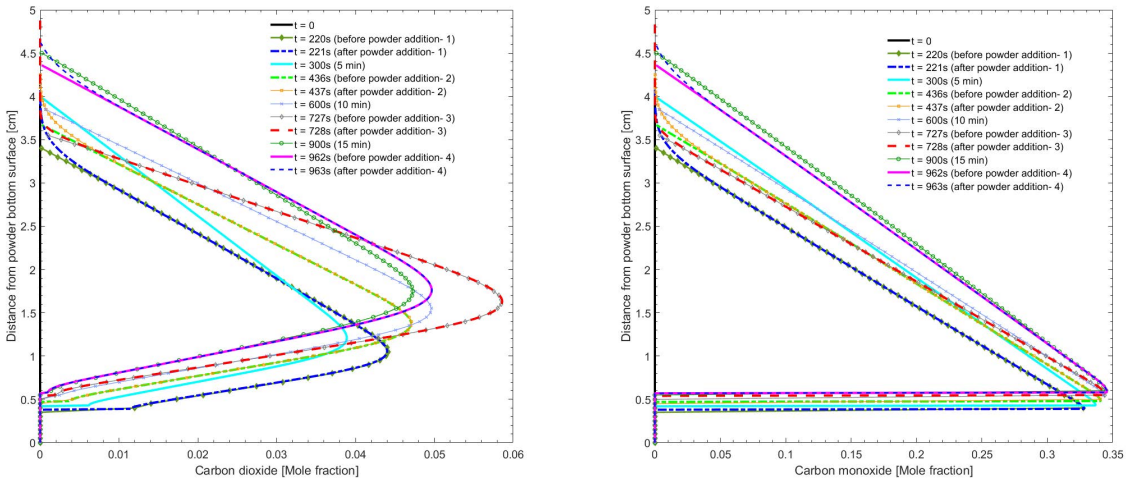

Figure 7.6 Mole fraction distributions of (a) Carbon dioxide (b) Carbon monoxide showing the powder addition times

As explained above, the Boudouard reaction becomes dominant in the powder bottom (bottom of the sinter layer which floats above the molten flux layer). This results in more CO_2 being burnt, and more CO being produced. At the powder-sinter/molten flux layer phase boundary, there is a steep gradient in gas concentration, as gas doesn't diffuse into the slag layer. Compared to the lab sintering experiment, the temperatures continue to increase with distance below the powder top surface to reach higher values. Toward the bottom of the sinter layer, the Boudouard reaction becomes more favorable and results in a higher concentration of CO and a lower concentration of CO_2 at the bottom of the powder.

The gaseous exhaust released from the caster (without any mixing in the air above the mold region) in the form of carbon dioxide and carbon monoxide are shown in Figure 7.7.

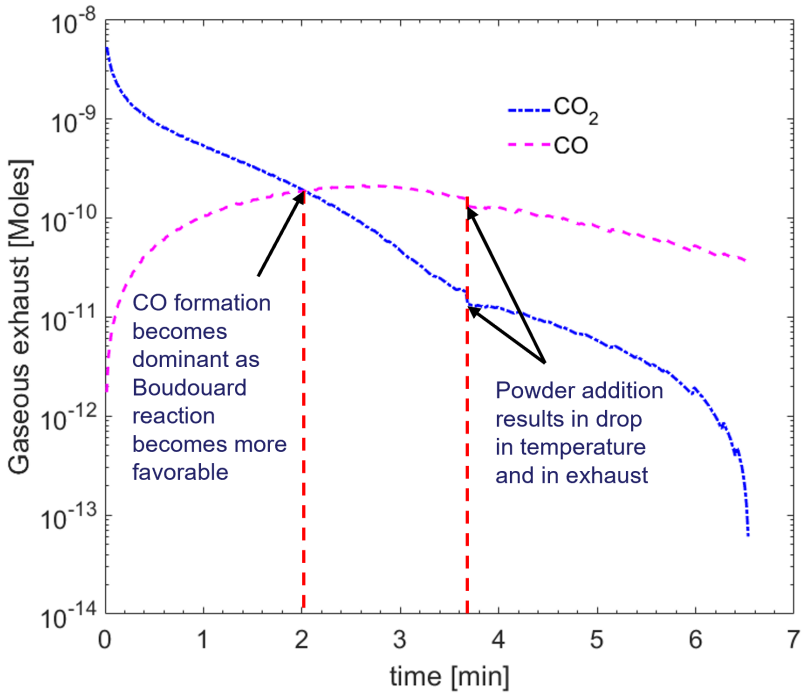

Figure 7.7 Gaseous exhaust exiting the top surface of the caster: Carbon dioxide and Carbon monoxide

At initial times, more CO_2 is released as exhaust compared to CO. But, as the powder heats up, the Boudouard reaction becomes more favorable, resulting in more CO formation than CO_2 formation. At $\sim 3.67min$, powder addition takes place at the powder top surface, which results in a drop in powder temperature. Due to the lower powder temperatures after the addition, there is a drop in CO and CO_2 exhaust.

The carbon combustion and gas transport physics have been successfully incorporated into the continuous caster. However, due to higher temperatures in the caster, the maximum gas diffusion rate is faster compared to that in the powder model, and the combustion rate reactions are non-linear thereby limiting the time-step size that can be used for the current explicit model.

The effect of carbon advection due to shrinkage and consumption velocity is implemented into the multiphysics model. It uses the same model methodology as the carbon advection effect implemented in the simulation of the lab sintering experiment and additionally includes the effect of the liquid flux layer and its consumption into the gap. The resulting carbon distribution is shown in Figure 7.8.

The model is run to simulate one powder addition cycle at the Dofasco caster containing the ULC slag. In the plant, transients occur due to powder addition every 3-5 min, and therefore the incoming cold powder slows down the heating conduction and sintering. Even though the powder is replenished with high frequency, the powder residence time is longer than the powder addition cycle time. So, this simulation is a

preliminary estimate of what might be expected in the plant.

The top zone of the powder is too cold to enable any carbon combustion. As we move deeper into the powder, the carbon burns by reacting with oxygen resulting in a small carbon depletion zone. Towards the powder bottom, it is observed that carbon accumulates near the powder bottom due to the combined effects of powder shrinkage and liquid flux consumption, resulting in carbon enrichment (higher carbon concentration than the initial value). The accumulation fraction observed in the caster sinter layer is greater than that of the lab sintering experiments, even though the time is more than 20 times shorter. This is because the consumption velocity is generally higher than the shrinkage velocity, and augments the advection effect. The current model is being improved to make better predictions of sintering including its effect on carbon enrichment, to include the effect of carbon on powder melting rate, and to validate this with plant measurements.

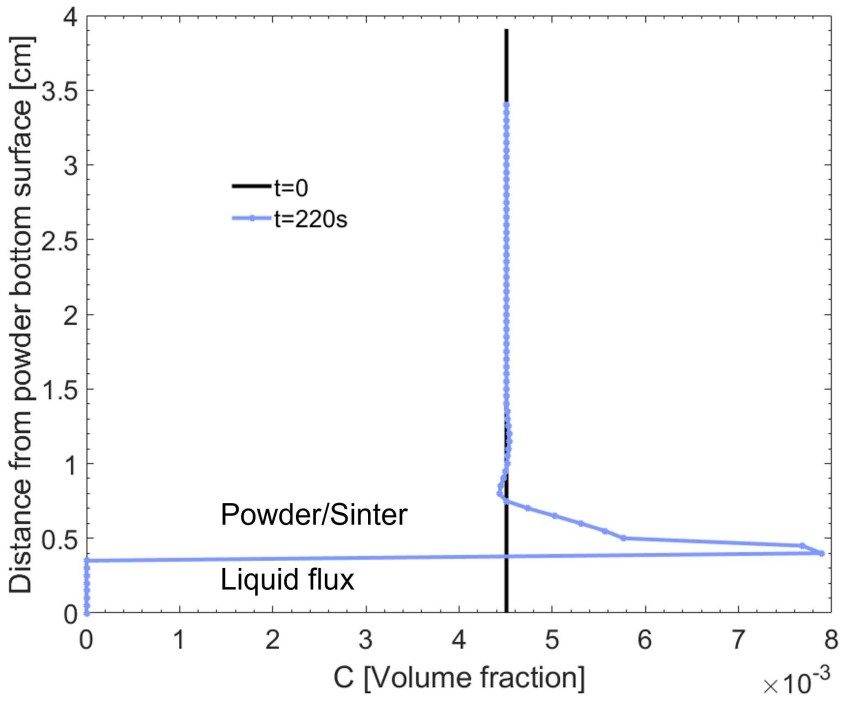

Figure 7.8 Carbon distribution through the powder/slag layers showing the enrichment near the powder bottom

7.4 Parametric study

The effect of convection due to fluid flow in the molten slag layer is studied in this section. The shear parameters of two industrial fluxes are shown in Table 7.2. A parametric study has been done on the Dofasco caster applying the multiphysics model to compare the base case of zero convection for ULC slag

with a case having molten steel shear velocity (surface velocity just beneath the slag layer) of 0.3 m/s chosen as a typical velocity within the window of good quality operation [85–89]. The thermal conductivity of the molten slag is enhanced by a Nusselt number (Nu) factor to account for the convection due to the fluid flow in the slag layer. Slag (a) (glassy [90]) has a Nu of 1.12 and slag (b) (crystalline [91]) has a Nu of 1.75 at 0.3 m/s [37]. The Dofasco slag simulated in this work is expected to be somewhat similar to these slags (a) and (b).

Table 7.2 Shear properties and parameters for industrial fluxes.[37]

Property/variable	Flux (a)	Flux (b)
Reference viscosity, μ_0 (Pa s)	0.87	0.39
Reference temperature, T_0 (°C)	1300	1300
Solidification temperature, T_s (°C)	850	1125
n	3.2	1.3

The equation used to calculate the flux viscosity variation with temperature is given by[37]:

$$\mu = \mu_0 (\frac{T_0 - T_s}{T - T_s})^n \tag{7.1}$$

The results from the multiphysics model simulations for the liquid flux thickness are shown in Figure 7.9.

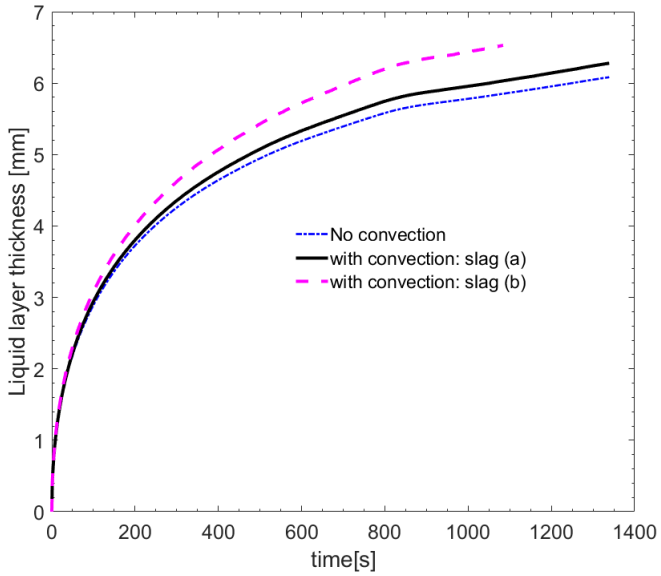

Figure 7.9 Parametric study on the effect of convection in the molten slag pool, showing fluxes (a) and (b) from literature [37], and ultra-low carbon steel slag from Dofasco [32] (no convection case)

It is observed that the cases that include the effect of convection in the molten slag pool have higher heat transfer due to mixing, resulting in faster powder melting, and consequently a deeper molten slag pool. The slag (b) has a lower viscosity at higher temperatures which generates more mixing and convection due to fluid flow in the liquid slag pool. The multiphysics model shows that the effect of fluid flow and convection in the slag pool results in a 3-10 % increase in the liquid flux thickness.

CHAPTER 8
CONCLUSIONS

8.1 General modeling conclusions

A novel multi-physics, finite-difference model has been developed to estimate the transient temperature distribution, sintering kinetics, phase-change behavior, mass transport, carbon burning, and gas transport through the top-surface powder and molten slag layers during continuous casting of steel. This multiphysics model incorporates rate kinetics to calculate powder properties and pore fraction in the powder/slag column and considers the effect of sintering. Powder densification due to sintering decreases the pore fraction which results in shrinkage and an increase in the thermal conductivity of powder. The powder model considers the effect of carbon combustion in the mold powder and can predict the resulting carbon and gas distribution due to chemical reactions. An exhaust model has been developed to maintain constant system pressure and help the gas mass balance model make more accurate predictions. Gas diffusion due to internal gradients has been incorporated into the model, which assists in evaluating the carbon distribution more accurately.

The carbon distribution in the top-surface powder layers is important because it affects carbon pickup and product contamination, and the viscosity and melting rate of the liquid slag, which provide lubrication to control mold heat transfer and prevent breakouts. To our knowledge, no prior model has attempted to predict the carbon distribution and detailed powder melting characteristics for a continuous caster. Additionally, it is arduous, and expensive to conduct experiments in the plant to measure the carbon and gas distribution through continuous casting mold powder/slag layers, and lab experiments cannot be accurately extrapolated to the plant scenario due to high temperatures, molten flux behavior, and effects of high-velocity turbulent flow in the mold of a real caster. Due to a lack of prior models, and experiments of carbon and gas variation through mold powders in a caster, this multiphysics model has been developed here in multiple steps systematically to generate valuable knowledge of the multiphysics of continuous casting mold powders. This has produced 3 models: a steady-state model, a transient model, and the complete multiphysics model, which each contain features to incorporate different phenomena that can be activated or deactivated.

Incorporating all of these physical phenomena present in our powder model (lab sintering experiment case without the molten flux layer) into our caster case gives us a better ability to understand the carbon combustion in mold powders, sintering behavior, and phase transitions. The model is being further developed to accurately predict the effect of carbon on the powder melting behavior. This should provide a

tool to enable simulations for parametric studies to understand how to operate their caster smoothly while optimizing mold powder performance.

8.2 Model verification

The steady-state model and the transient thermal model have been verified with a model developed in a commercial CFD package, Ansys Fluent.

8.3 Sintering model validation

The transient thermal model was validated with measurements in two different operating commercial slab casters. Given the powder thickness variations during intermittent powder feeding, the model matched the measured temperature histories.

The multiphysics model was first validated with measurements in a lab sintering experiment. In addition to matching reasonably well with predictions of a previous computational model, the current multiphysics model matches reasonably well with measurements of the total powder level drop after 2 hours, the temperature distribution at several different depths inside the powder layer, and the carbon concentration profile. The model predictions also matched approximately with the CO and CO_2 concentrations measured in the exhaust gas from the top surface of the powder layer. It is found that considering the density variation through the powder/slag layers (initial phase-dependent density for the caster, or accurate density estimate by implementing sintering kinetics) causes about a 10% increase in powder mass at the bottom to accurately predict the level changes in the powder, which also has a minor effect on the temperature distribution.

The multiphysics is further validated by its ability to match with trends observed in the plant. This includes the drop in powder/slag heights in between powder additions at the plant which results in in a rise in powder surface temperatures. It also predicts an increase in powder/slag temperatures, and density as we move closer to the molten steel-liquid flux phase boundary. It also exhibits a drop in powder carbon content due to combustion in powder mid-zone along with predicting the resulting gas distribution. Most importantly, it correctly predicts an increase in carbon content near the bottom of the sinter layer which is larger in the caster in comparison to the lab sintering experiment.

8.4 Caster Results

Powder surface temperatures in the caster are found to increase between powder additions, while the total powder/slag thickness drops due to liquid flux consumption into the gap. The current model can quantify this effect, which comprises several hundreds of degrees. For the case of continuous powder

additions, considering the effect of carbon combustion (even with a modified specific heat effect) is important to achieve reasonable model validation.

The time delay before beginning to heat up the top surface of the powder has a linear dependence on the amount of powder added during each addition cycle. Transient thermal model matches with plant predictions of powder/slag thickness, and surface temperature for several plant cases of manual, and automated feeding.

Parametric studies with the transient thermal model applied to the continuous caster reveal that

- Increasing slag consumption rate causes shallower liquid slag pool and lower powder surface temperatures.
- Increasing air content of the powder (lower packing density) causes a faster drop in powder surface levels, and higher powder temperatures.
- Higher auto-feed powder levels result in colder powder surface temperatures; and a near-constant liquid flux level, compared with manual feeding.
- Increasing the molten steel velocity beneath the powder layer increases convective mixing in the liquid slag layer and increases heat conduction, which slightly increases the powder melting rates.

8.5 Specific modeling conclusions

The key takeaways from the novel multiphysics model are summarized below:

- A new in-house model of transient heat transfer in slag layers has been verified with computational models using Ansys Fluent, validated with the lab experiments of sintering, and further validated with measurements in operating continuous slab casters.
- Densification due to sintering causes a decrease in pore fraction which results in shrinkage, and an increase in the thermal conductivity of powder.
- Powder surface temperature increases between powder additions, while the total powder/slag thickness drops due to liquid flux consumption into the gap and the shrinkage due to powder sintering, combined with increasing heat losses to the thinner and thus less-insulating powder bed cover.
- Considering phase-dependent powder/slag density is important to achieve a good match with measurements based on comparison with the lab experiments. The transient thermal model uses a

layer-dependent density, while the multi-physics model uses sintering kinetics to accurately predict the density variation through the powder/sinter layers.

- The carbon profile predicted has an 'S-shaped' profile due to various chemical reactions, gas diffusion, and mass transport mechanisms occurring in different regions of the powder/slag. At the powder top surface region, the carbon concentration stays constant as the temperature is too low for combustion to occur. Moving down through the powder, the carbon content decreases due to the reaction of carbon with oxygen. This continues deeper into the powder so long as oxygen is available, and then after that the carbon burning slows. Towards the powder bottom region, carbon is expected to increase due to mass advection due to both shrinkage and liquid slag consumption. At the very bottom, carbon reacts with carbon dioxide via the Boudouard reaction, and hence, the carbon content further decreases.

- An exhaust model is developed to predict the rate and composition of gases leaving the top surface., and to maintain constant system pressure, and helps the gas mass balance model make more accurate predictions. Exhaust gas in the lab sintering case exhibits an initial peak of carbon dioxide due to the exothermic carbon oxidation reaction leading to the formation of CO_2. The volume percent of CO_2 released is found to be higher than CO as the carbon oxidation reaction forming CO_2 occurs in a larger section of powder due to optimal thermal conditions, and availability of oxygen. At long times, the volume of gases released as exhaust approaches a steady state. There is a reasonably good match between the model prediction and measurements in the lab sintering experiment.

- Incorporating the effect of powder advection due to shrinkage due to sintering has improved the match with measurements of carbon concentration. Further improvements are being implemented into the model to accurately predict the effect of this downward movement of carbon, and achieve better validation with measurements. The extent of carbon accumulation in the caster is greater than in the lab sintering experiments. A new methodology is being developed to account for the decrease in powder sintering due to the presence of carbon particles (which separate the powder particles and decrease their ability to coalesce and sinter) which should decrease the powder melting rate as explained in the next chapter.

CHAPTER 9
FUTURE WORK

The future work can be divided into the following sections: improved sintering model, shrinkage velocity model, improved heat transfer model, effect of carbon on melting rate, additional gas balance models, carbon mass diffusion model, implicit solution procedure, parametric studies, and software package development.

9.1 Improved sintering model

In the current sintering model, the rate depends on both temperature, and time, such that sintering occurs at long times also when the powder is getting cooled, which is not realistic. The current sintering model needs to be replaced with a fundamentally-based microscale model of sintering, melting and carbon combustion on the scale of the particles which are hollow or spherical. The melting rate should be calculated by the model considering radial heat conduction and effect of changing particle shape, surface area, porosity, and heat conduction across the gaps and contact area rather than hard-wired to the measured consumption rate.

9.2 Shrinkage velocity model

The current model includes the mass transfer down the column of cells due to the shrinkage velocity (from the sintering model). Densification causes the powder to move downward with time according to its temperature history. The accompanying downward movement of carbon and gases tends to increase their concentration. This is currently overpredicted. In addition, the carbon dioxide in the exhaust is overpredcited, and the carbon monoxide is underpredicted perhaps because the Boudouard reaction deep in the powder is not strong enough. If the sintering was slower, then the shrinkage velocity would be lower, and there would be more pores for the Boudouard reaction. This might alleviate both the problems. The new shrinkage velocity from the new fundamentally-based sintering model should improve the model prediction, thereby giving a better match with the measurements.

9.3 Improved heat transfer model

The effect of gas transport, and fluid flow in the molten flux layer (enhancing the role of convective heat transfer) on the resulting heat transfer through the powder/sinter layers has been studied.

Including new phenomena such as the effects of fluid flow and its enhancement of heat and mass transport in the liquid flux layer, and particle melting model can help to better quantify of the thermal

profile in the powder/slag layer. The flow in the mold is complex and three-dimensional which causes a variation in liquid slag-steel interface profile, and velocity across the top surface. This effect should be taken into account such as by running the 1-D multiphysics model for different conditions at different locations over the steel surface.

9.4 Effect of carbon on melting rate

Increasing the carbon content of the mold powder is known to decrease the powder melting rate. However, the mechanism of how this occurs is not well understood. We want to test a hypothesis based on plant experience, which mentions that carbon separates the powder particles, hinders the sintering process, and hence slows down the rate of melting of the powder. The sintering model is currently step-wise coupled with the heat transfer model, but it is independent of the carbon combustion physics. The new sintering model described above, should be able to capture the effect of the carbon particles on sintering. This should enable the multiphysics model to quantify the effect of increasing carbon on decreasing powder melting rate.

9.5 Additional gas balance models

Other secondary models can be developed to predict the hydrogen, and fluorine distribution, and estimate the effects of water vapor on the various combustion reactions.

Hydrogen is detrimental because it creates H gas bubbles and porosity in the liquid slag layer in the gap, which lowers interfacial heat transfer, and in severe cases, causes a breakout (many plants have had big problems with breakouts caused by hydrogen). This can occur if the liquid flux is thin, or if H atom can diffuse through the flux layer. The exhaust gas prediction should be augmented to include fluorine.

The rate of CO oxidation is generally driven by the humidity in the gas stream. In the absence of humidity, the rates are much slower. Therefore, taking into account the effect of humidity in the mold powder on the combustion reactions will represent the steel plant operating conditions more accurately and result in an better prediction of the carbon distribution in the powder/slag layer.

Fluorine is a poisonous gas and over-exposure can be fatal (New Jersey prescribes a limit of 0.1ppm averaged over a 10-hour work shift). Calcium fluoride is added to the mold powder to control the liquid slag fluidity. However, it can decompose to release fluorine gas/fluoride-based compounds, which are poisonous and can be harmful to the operators working on the shop floor. So, it is important to predict the hydrogen and fluorine gas behavior and distribution (and gas levels in the air above the powder) for different ranges of casting conditions in the plant.

9.6 Carbon Mass diffusion model

The model should be improved to enable the estimation of the importance of material and process parameters on carbon pick-up by molten steel due to the effects of mass diffusion of carbon from the mold powder into the liquid flux. The fluid flow beneath the powder layers changes the surface profile, leading to the high-C concentrated sinter layer directly contacting the molten steel. This mechanism also needs to be incorporated into the new model.

9.7 Implicit solution procedure

Our existing explicit model needs to be improved by implementing a semi-implicit formulation to enable large time steps through the simulation to decrease computational times. The temperature and sintering models can remain explicit because their critical minimum time-step sizes are already sufficiently large. By implementing this, the model can run faster, and better perform validation with plant measurements.

The temperatures in powder/slag layers in the continuous caster are much higher due to the presence of the liquid flux layer which is in contact with the molten steel. These high-temperature conditions can cause model difficulties as higher gas diffusion speeds and greater reaction rates (which are already non-linear) will limit the model to use a small time step size to ensure numerical accuracy. An implicit Newton-Raphson iterative procedure along with Tri-Diagonal Matrix Algorithm (TDMA) should be considered to solve the gas balance equations (express the mole fractions, and gas concentrations in the form of the gas moles for each species) simultaneously. It will be important to determine the value/range of the under-relaxation parameter that can be used to ensure model stability and accuracy. It will also be important to determine how big of a time step size can be used to save computational time without compromising on numerical accuracy.

9.8 Further Parametric studies

The best final version of the multiphysics model should be run in several different parametric studies to investigate the important effects of casting parameters and powder composition to reveal important practical results, such as the effect of casting speed on powder consumption. The studies can enable better plant practices resulting in a superior mold powder performance.

9.9 Develop software package

The final model should be converted into a user-friendly GUI package, to enable plant engineers to predict transients at the plant, and to generate flash warning when powder addition is required, or when the temperatures fall below a critical value.

REFERENCES

[1] Steel statistical yearbook. *World Steel Association*, 2017. URL https://www.worldsteel.org/en/dam/jcr:3e275c73-6f11-4e7f-a5d823d9bc5c508f/Steel+Statistical+Yearbook+2017.pdf.

[2] B. G. Thomas. Continuous casting process. URL http://ccc.mines.edu/introduction/tundish.html.

[3] B. G. Thomas. Mold powders presentation. *personal communication*, 2019.

[4] J. Moore. An overview for the requirements of continuous casting mold fluxes. In *Steelmaking Conference Proceedings*, volume 74, pages 615–621, 1991.

[5] C. Pinheiro. Mold flux for continuous casting of steel. *Iron and Steelmaker*, 21(12):12–14, 1994.

[6] K. C. Mills, S. Sridhar, A.S. Normanton, and S.T. Mallaband. Mould flux behaviour in continuous casting. In *The Brimacombe Memorial Symposium*, pages 781–794, 2000.

[7] C. Pinheiro. Mold flux for continuous casting of steel. *Iron Steelmaker*, 22(1):43–44, 1995.

[8] M Emi. The mechanisms for sticking type break-outs and new developments in continuous casting mold fluxes. In *Steelmaking Conference Proceedings.*, volume 74, pages 623–630, 1991.

[9] S. Feldbauer, I. Jimbo, A. Sharan, K. Shimizu, W. King, J. Stepanek, J. Harman, and A.W. Cramb. Physical properties of mold slags that are relevant to clean steel manufacture. In *Steelmaking Conference Proceedings.*, volume 78, pages 655–667, 1995.

[10] C. Däcker K. C. Mills. *The Casting Powders Book*. Springer, 2018. doi: https://doi.org/10.1007/978-3-319-53616-3.

[11] N. Masuo M. Fuji T. Matsuyama T. Nakano, K. Nagano. Model analysis of melting process of mold powder for continuous casting of steel. *Nippon steel technical report. Overseas*, 34:21–30, 1987.

[12] M. Supradist, A. W. Cramb, and K. Schwerdtfeger. Combustion of carbon in casting powder in a temperature gradient. *ISIJ International*, 44(5):817–826, 2004. doi: 10.2355/isijinternational.44.817.

[13] K. Schwerdtfeger and A. Jablonka. Kinetics of carbon combustion in packings of casting powder. *Steel research*, 64(1):77–86, 1993.

[14] N. Gruber. Effect of carbon on the melting behavior of a mold powder under high heating rates. *BHM Berg-und Hüttenmännische Monatshefte*, 168(11):521–526, 2023.

[15] T. Kargul. The analysis of gas evolved from casting powder during heating in the mold. *Journal of Thermal Analysis and Calorimetry*, 139(2):877–884, 2020.

[16] I. Marschall, N. Kölbl, H. Harmuth, and C. Atzenhofer. Identification of secondary raw materials in mold powders and their melting behavior. *Journal of Iron and Steel research international*, 26: 403–411, 2019.

[17] F. Chen, G. Wen, P. Tang, L. Yu, and F. Han. The role of carbonaceous materials in mold powder and influence on melting behavior. *Journal of Thermal Analysis and Calorimetry*, 147(20): 10965–10975, 2022.

[18] D. Singh, P. Bhardwaj, Y. D. Yang, A. McLean, M. Hasegawa, and M. Iwase. The influence of carbonaceous material on the melting behaviour of mould powder. *Steel Research international*, 81 (11):974–979, 2010.

[19] E Benavidez, L Santini, and E Brandaleze. Decomposition kinetic of carbonaceous materials used in a mold flux design. *Journal of thermal analysis and calorimetry*, 103(2):485–493, 2011.

[20] M. S. El-Genk and J-M P. Tournier. Development and validation of a model for the chemical kinetics of graphite oxidation. *Journal of Nuclear Materials*, 411(1-3):193–207, 2011.

[21] B. Xie, J. Wu, and Y. Gan. Study on amount and scheme of carbon mixed in cc mold fluxes. *Steelmaking Proceedings*, 74:647–651, 1991.

[22] T. C Brown et al. Carbon oxidation kinetics from evolved carbon oxide analysis during temperature-programmed oxidation. *Carbon*, 39(5):725–732, 2001.

[23] L. Xiaowei, R. Jean-Charles, and Y. Suyuan. Effect of temperature on graphite oxidation behavior. *Nuclear Engineering and Design*, 227(3):273–280, 2004.

[24] G. Blyholder and H. Eyring. Kinetics of graphite oxidation. *The Journal of Physical Chemistry*, 61(5): 682–688, 1957.

[25] W.A. Propp. Graphite oxidation thermodynamics/reactions. Technical report, Idaho National Lab.(INL), Idaho Falls, ID (United States), 1998.

[26] J.N. Ong Jr. On the kinetics of oxidation of graphite. *Carbon*, 2(3):281–297, 1964.

[27] R.J. Tyler, H.J. Wouterlood, and M.F.R. Mulcahy. Kinetics of the graphite-oxygen reaction near 1000 k. *Carbon*, 14(5):271–278, 1976.

[28] C. I. Contescu, R. W. Mee, J. D. Arregui-Mena, N. C Gallego, T. D. Burchell, J. J. Kane, W. E. Windes, et al. Beyond the classical kinetic model for chronic graphite oxidation by moisture in high temperature gas-cooled reactors. *Carbon*, 127:158–169, 2018.

[29] E.T. Turkdogan and J.V. Vinters. Kinetics of oxidation of graphite and charcoal in carbon dioxide. *Carbon*, 7(1):101–117, 1969.

[30] F. Chen, G. Wen, P. Tang, and Q. Fu. Test method of mold powder melting rate based on copper bath and its application. In *TMS Annual Meeting & Exhibition*, pages 147–156. Springer, 2023.

[31] J.A. Kromhout and D.W. Van der Plas. Melting speed of mould powders: determination and application in casting practice. *Ironmaking & steelmaking*, 29(4):303–307, 2002.

[32] A. Akhtar. Analysis of the nail board experiment to measure the liquid slag depth in steel continuous casting). Technical report, University of Illinois, Urbana-Champaign, 2016.

[33] A. Akhtar, B. G. Thomas, and J. Sengupta. Analysis of nail board measurements of liquid slag layer depth. *Proceedings of the AISTech*, pages 1427–1438, 2016.

[34] R. McDavid. Flow and thermal behavior of the top surface flux/powders in continuous casting molds. Technical report, University of Illinois, Urbana Champaign, 1994.

[35] H. Nakato, T. Sakuraya, T. Nozaki, T. Emi, , and H. Nishikawa. Physical and chemical properties of casting powders affecting the mold lubrication during continuous casting. (retroactive coverage). *Steelmaking Proceedings*, 69:137–143, 1986.

[36] J. Cho, H. Shibata, T. Emi, and M. Suzuki. Radiative heat transfer through mold flux film during initial solidification in continuous casting of steel. *ISIJ International*, 38(3):268–275, 1998. doi: 10.2355/isijinternational.38.268.

[37] B. Zhao. Numerical study of flow and heat transfer in a molten flux layer. *International Journal of Heat and Fluid Flow*, 26(1):105–118, 2005. ISSN 0142-727X. doi: https://doi.org/10.1016/j.ijheatfluidflow.2004.05.016.

[38] K. R. Kirchartz and H. Oertel. Three-dimensional thermal cellular convection in rectangular boxes. *Journal of Fluid Mechanics*, 192:249 – 286, 1988. URL https://api.semanticscholar.org/CorpusID:121070777.

[39] M. M. Wolf. Mould powder consumption- a useful criterion? *Proceedings of 2nd European Conference on Continuous Casting*, 1:78, 1994.

[40] M. Suzuki, M. Suzuki, and M. Nakada. Perspectives of research on high-speed conventional slabcontinuous casting of carbon steels. *ISIJ International*, 41(7):670–682, 2001. doi: 10.2355/isijinternational.41.670.

[41] T. Koichi, M. Hiroshi, N. Shin-ichi, T. Mitsuhiro, N. Masayuki, and K. Masami. Estimation of mold powder consumption in continuous casting. *Tetsu To Hagane-journal of The Iron and Steel Institute of Japan*, 84:617–624, 1998. URL https://api.semanticscholar.org/CorpusID:138740590.

[42] I. R. Lee J. W. Kim K. H. Moon O. D. Kwon, J. Choi and Y. K. Shin. *Steelmaking Conference Proceedings, ISS-AIME, Warrendale, PA,*, page 561, 1991.

[43] H-J Shin, S-H Kim, B. G. Thomas, G-G Lee, J-M Park, and J. Sengupta. Measurement and prediction of lubrication, powder consumption, and oscillation mark profiles in ultra-low carbon steel slabs. *ISIJ International*, 46(11):1635–1644, 2006. doi: 10.2355/isijinternational.46.1635.

[44] F. Thümmler and W. Thomma. The sintering process. *Metallurgical Reviews*, 12(1):69–108, 1967.

[45] J. Rekola. Isothermal sintering kinetics of uosub (2+ x). Technical report, Helsinki Univ. of Technology, 1978.

[46] F. Han, L. Yu, G. Wen, X. Wang, F. Zhang, J. Jia, and Sh. Gu. The effect of composition segregation of mold powder produced by spray granulation on the sintering performance. *Journal of Materials Research and Technology*, 20:448–458, 2022. ISSN 2238-7854. doi: https://doi.org/10.1016/j.jmrt.2022.07.111.

[47] J. C. Maya, F. Chejne, C. A. Gómez, and S. K. Bhatia. Effect of the cao sintering on the calcination rate of caco3 under atmospheres containing co2. *AIChE Journal*, 64(10):3638–3648, 2018.

[48] K. Yasui and K. Hamamoto. Comparison between cold sintering and dry pressing of caco3 at room temperature by numerical simulations. *AIP Advances*, 12(4), 2022.

[49] K. Yasui and K. Hamamoto. Simple physical model with empirical formulas for solid-state sintering of caco3 for estimation of porosity. *AIP Advances*, 13(4), 2023.

[50] J. C Maya, F. Chejne, and S. K. Bhatia. On the modeling of the co2-catalyzed sintering of calcium oxide. *AIChE Journal*, 63(8):3286–3296, 2017.

[51] R. H. Borgwardt. Sintering of nascent calcium oxide. *Chemical Engineering Science*, 44(1):53–60, 1989. ISSN 0009-2509. doi: https://doi.org/10.1016/0009-2509(89)85232-7. URL https://www.sciencedirect.com/science/article/pii/0009250989852327.

[52] W.L. De Keyser, R. Wollast, and P-H Duvigneaud. The sintering of activated cao. *Journal of Materials Science*, 4:989–996, 1969.

[53] R.M. German and Z.A. Munir. Surface area reduction during isothermal sintering. *Journal of the American Ceramic Society*, 59(9-10):379–383, 1976.

[54] F. Chen, G. Wen, P. Cheng, P. Tang, and Z. Hou. Simulation of the effect of flux layer thickness on the melting behavior of mold fluxes based on the copper bath method. *Metallurgical and Materials Transactions B*, pages 1–13, 2024.

[55] J. Marioton A. Delhalle, M. Larrecq and P. Riboud. Slag melting and behaviour at meniscus level in a cc mold. *Steelmaking Proceedings*, 69:145–152, 1986.

[56] S. P. Andersson. Thermal conductivity of powders used in continuous casting of steelpart 2–powders. *Ironmaking & Steelmaking*, 42(6):465–470, 2015.

[57] S. P. Andersson and C. Eggertson. Thermal conductivity of powders used in continuous casting of steel: Part 1–glassy and crystalline slags. *Ironmaking & Steelmaking*, 42(6):456–464, 2015.

[58] N. Gruber. Liquefaction controlling components and their effect on carbon-free mold powders. *Metallurgical and Materials Transactions B*, 54(6):3092–3100, 2023.

[59] H. Takeuchi, H. Mori, T. Nishida, T. Yanal, and K. Mukunashi. Development of a carbon-free casting powder for continuous casting of steels. *Transactions of the Iron and Steel Institute of Japan*, 19(5): 274–282, 1979. doi: 10.2355/isijinternational1966.19.274.

[60] P. Bhardwaj. *Respect to Mold Powder Design for Continuous Casting of Steel*. PhD thesis, University of Toronto, 2007.

[61] M. Kawamoto, K. Nakajima, T. Kanazawa, and K. Nakai. Design principles of mold powder for high speed continuous casting. *Tetsu-to-hagané*, 80(3):219–224, 1994.

[62] R. M. McDavid and B. G. Thomas. Flow and thermal behavior of the top surface flux/powder layers in continuous casting molds. *Metallurgical and Materials transactions B*, 27:672–685, 1996.

[63] J.A. Kromhout, S. Melzer, E.W. Zinngrebe, A.A. Kamperman, and R. Boom. Mould powder requirements for high-speed casting. *Steel Research international*, 79(2):143–148, 2008.

[64] J.A. Kromhout, C. Liebske, S. Melzer, A.A. Kamperman, and R. Boom. Mould powder investigations for high speed casting. *Ironmaking & Steelmaking*, 36(4):291–299, 2009.

[65] F Neumann, J Neal, and M Pedroza. Mold fluxes in high speed thin slab casting. In *Seventy Ninth Conference of the Steelmaking Division of the Iron and Steel Society*, pages 249–257, 1996.

[66] J Moore. Mold flux developments for high speed slab casting. In *Seventy Ninth Conference of the Steelmaking Division of the Iron and Steel Society*, pages 259–264, 1996.

[67] J.A. Kromhout and R.C. Schimmel. Understanding mould powders for high-speed casting. *Ironmaking & Steelmaking*, 45(3):249–256, 2018.

[68] K. C. Mills. The influence of structure on the physico-chemical properties of slags. *ISIJ International*, 33(1):148–155, 1993. doi: 10.2355/isijinternational.33.148.

[69] T. Matsushita, T. Ishikawa, P-F Paradis, K. Mukai, and S. Seetharaman. Density measurements of mould flux slags by electrostatic levitation method. *ISIJ International*, 46(4):606–610, 2006. doi: 10.2355/isijinternational.46.606.

[70] K. C. Mills and A. B. Fox. The role of mould fluxes in continuous casting-so simple yet so complex. *ISIJ International*, 43(10):1479–1486, 2003. doi: 10.2355/isijinternational.43.1479.

[71] C. Lefebvre, J. P. Radot, J. N. Pontoire, and Y. Roux. Development of a continuous casting mould powder for the limitation of recarburization in ulc steels. *Revue de metallurgie Cahiers d'informations techniques*, 94(4):489, 1997.

[72] H. Nakato, S. Takeuchi, T. Fujii, T. Nozaki, and M. Washio. Characteristics of new mold fluxes for strand casting of low and ultra low carbon steel slabs. In *Steelmaking Conference Proceedings*, volume 74, pages 639–646, 1991.

[73] T. Nakano, T. Kishi, K. Koyama, T. Komai, and S. Naitoh. Mold powder technology for continuous casting of aluminium-killed steel. *ISIJ Transactions*, 24:950–956, 1984.

[74] A. B. Fox, K. C. Mills, D. Lever, C. Bezerra, C. Valadares, I. Unamuno, J. J. Laraudogoitia, and J. Gisby. Development of fluoride-free fluxes for billet casting. *ISIJ International*, 45(7):1051–1058, 2005. doi: 10.2355/isijinternational.45.1051.

[75] W. Wang, D. Cai, and L. Zhang. A review of fluorine-free mold flux development. *ISIJ International*, 58(11):1957–1964, 2018. doi: 10.2355/isijinternational.ISIJINT-2018-232.

[76] M. C. C. Bezerra, C. A. G. Valadares, I. P. Rocha, J. R. Bolota, M. C. Carboni, I. L. de Mattos Scripnic, C. R. Santos, K. Mills, and D. Lever. Impact of fluorine free mould flux use on continuous casting process. *International Porto Alegre—RS Brazil*, 2006.

[77] The MathWorks Inc. Optimization toolbox version: 9.5, R2023a Update 4. URL https://www.mathworks.com.

[78] J. Kromhout. Mold powders presentation. *Tata Steel, RD, IJmuiden, The Netherlands*, personal communication, 2023.

[79] H.W. Russel. Principles of heat flow in porous insulators. *Journal of American Ceramic Society*, (18): 1–5, 1935.

[80] J. Warnatz, U. Maas, R. W. Dibble, and J. Warnatz. *Combustion*. Springer, 2006.

[81] E.T. Turkdogan and J.V. Vinters. Effect of carbon monoxide on the rate of oxidation of charcoal, graphite and coke in carbon dioxide. *Carbon*, 8(1):39–53, 1970. ISSN 0008-6223. doi: https://doi.org/10.1016/0008-6223(70)90127-2. URL https://www.sciencedirect.com/science/article/pii/0008622370901272.

[82] K. Schwerdtfeger, J. Sardemann, and H-J Grethe. Oxidation of carbon and decomposition of carbonate during the heating of casting powders. *Stahl und Eisen(Germany)*, 2:57–64, 1994.

[83] R. B. Bird, W. E. Stewart, and E. N. Lightfoot. *Transport phenomena*. John Wiley Sons, New York, rev. 2nd ed. edition, 2007. ISBN 0470115394.

[84] M. Supradist. Temperature measurements. *personal communication*, July, 2024.

[85] S-M Cho and B. G. Thomas. Electromagnetic effects on solidification defect formation in continuous steel casting. *JOM*, 72(10):3610–3627, 2020.

[86] J. Kubota, N. Kubo, M. Suzuki, T. Ishii, R. Nishimachi, and N. Aramaki. Steel flow control with travelling magnetic field for slab continuous caster mold. *Tetsu-to-hagane*, 86(4):271–277, 2000.

[87] H. Nakamura, S. Kohira, J. Kubota, R. Kondo, M. Suzuki, and Y Shiratani. Technology for production of high quality slab at high speed casting. In *Steelmaking Conference Proceedings.*, volume 75, pages 409–415, 1992.

[88] T. Teshima, M. Osame, K. Okimoto, and Y. Nimura. Improvement of surface property of steel at high casting speed. In *Proceedings of Steelmaking Conference (The Iron and Steel Society, Warrendale)*, volume 71, page 111–118, 1988.

[89] J. Kubota, K. Okimoto, A. Shirayama, and H. Murakami. In *Steelmaking Conference Proceedings (The Iron and Steel Society, Warrendale)*, page 233–241, 1991.

[90] D. Larson. Criteria for selecting mold powders to optimize continuous cast steel quality. *Ind. Heat.*, 53 (4):16–19, 1986.

[91] M. D. Lanyi and C. J Rosa. Viscosity of casting fluxes used during continuous casting of steel. *Metallurgical Transactions B*, 12:287–298, 1981.

APPENDIX A

NOMENCLATURE

Table A.1 Parameters used for energy and mass balance calculation.

Property/variable	Unit/Value
Nodal location (distance from domain bottom), z	m
Time, t, and Time step size, dt	s
Temperature, T	K
Liquid flux density, ρ_f	2600 kg/m^3
Powder/Slag density, ρ	kg/m^3
Thermal conductivity, k	$W/m-K$
Specific heat, c_p	$J/kg-K$
Powder level drop, $ht_{shrinkage}$	m
Slag consumption velocity, $v_{cons,f}$	m/s
Powder shrinkage velocity, $v_{shrink,p}$	m/s
Powder mass in cell, m_p	kg
Rate of powder addition, $\dot{m}_{add,p}$	kg/s
Rate of liquid flux consumption, $\dot{m}_{cons,f}$	kg/s
Rate of powder advection due to sintering, $\dot{m}_{adv}$	kg/s
Time step number, r (previous),$r+1$ (current)	#
Powder/slag interface, $w^r_{inter,1,2,3,4}$ (after mass balance)	m
Powder/slag interface, $w^r_{final,1,2,3,4}$ (after energy balance)	m
Domain bottom, $w^r_{final,1}$,$w^r_{inter,1}$ (fixed)	m
Liquid flux- sinter interface, $w^r_{final,2}$,$w^r_{inter,2}$ (moving)	m
Powder-air interface, $w^r_{final,3}$,$w^r_{inter,3}$ (moving)	m
Domain top, $w^r_{final,4}$,$w^r_{inter,4}$ (fixed)	m
Strand cross-section area, A_c	m^2

Table A.2 Parameters used for densification calculation in current model.

Property/variable	Unit/Value
Apparent density, ρ^0_{app} (cold powder at 300K)	0.62 g/cm^3
Solid powder density, ρ_s (fully sintered)	2.7 g/cm^3
Instantaneous powder density, ρ_{app}	g/cm^3
Sintering rate constant, K_s (Based on experiments [12])	0 ($T < 400°C$)
	0.036 mass fraction $min^{-0.5}$ ($T = 600°C$)
	0.045 mass fraction $min^{-0.5}$ ($T = 800°C$)
	0.361 mass fraction $min^{-0.5}$ ($T = 1000°C$)
Solid powder thermal conductivity, k_{solid}	2 $W/m-K$
Gas thermal conductivity, k_{gas}	0.026 $W/m-K$
Effective thermal conductivity, k_{eff}	$W/m-K$
Void/Pore fraction, α_g	#
Time, t	min
Sintering parameter, n	0.5

Table A.3 Parameters used for combustion calculation.

Property/variable	Unit/Value
Molecular weight of oxygen, M_{O_2}	32 g/mol
Molecular weight of nitrogen, M_{N_2}	28.02 g/mol
Pressure, P	$1atm$
Collision diameter, $\sigma_{O_2-N_2}(=\frac{\sigma_{O_2}+\sigma_{N_2}}{2})$	A^o
Collision integral for $O_2 - N_2$ mixture at dimensionless temperature, $\Omega_{D_{O_2-N_2}}$	K
Temperature for Lennard-Jones potential, $T^*_{O_2-N_2}$ $(=[\frac{\kappa}{\epsilon}]_{O_2-N_2} * T)$	K
Boltzmann constant, κ	J/K
Initial Carbon volume fraction, $g_{C,0}$	0.0141 (lab expt.), 0.0045 (caster)
Instantaneous carbon volume fraction, g_C	#
Carbon density, ρ_C	$2.2g/cm^3$
Molecular mass of carbon, M_C	12.011 g/mol
Exponent in rate equation 1 (r_1), α	1.87 at 400 $^\circ C$
Temperature, T	K
Chemical reaction rates in 4-eCM, r_1, r_2, r_3, r_4	$mol/cm^3/min$
Mole fraction of gaseous component,i, x_i	#
Reaction rate constant, k_{O_2}	$atm^{-1}min^{-1}$
Equilibrium constant for rate equation $1(r_1)$, K_1	#
Exponent in rate equation equation 2, (r_2), β	1 at $400^\circ C$
Gas fraction based on sintering kinetics, α_g,	#
Gas concentration, c_g	mol/cm^3

APPENDIX B

COPYRIGHT PERMISSIONS

B.1 Permission from Prof. B.G. Thomas, and Continuous Casting Center(CCC), Mines

Dear Lipsa,

Of course, you have permission to use any figures created in the Continuous Casting Center, with copyright held by the CCC, so long as proper reference is given to the figure creator (if it is not you).

--Brian.

Brian G. Thomas
Research Professor of Mechanical Engineering, Colorado School of Mines,

CJ Gauthier Professor Emeritus and Research Professor, University of Illinois,

Department of Mechanical Engineering, Brown Hall W470-A
1610 Illinois Street, Golden, CO 80401
303-273-3309 bgthomas@mines.edu

From: Lipsa Das (Student) <lipsadas@mines.edu>
Sent: Tuesday, November 19, 2024 9:22 AM
To: Brian Thomas <bgthomas@mines.edu>
Subject: Request to use copyrighted material in my PhD Thesis

Hi Prof. Thomas,

I hope you are doing well. I have included a couple of figures from your work to introduce the continuous casting process in my Thesis (please see attached)

As per the university's rule of "using copyrighted material" (https://www.mines.edu/graduate-studies/thesis-writers-guide/),

“if you want to include in your thesis a Figure or Table from a source for which you were not an author (e.g. a journal article, textbook, website, technical report), you must OBTAIN and INCLUDE any necessary permissions from the original author and/or publisher. Otherwise, even if you cite the original source, you will be in violation of copyright law.”

I am requesting permission to use the attached figures in my thesis, with due credits given to you and the Continuous Casting Center.

Please give me permission to use these figures from this paper and confirm your approval as soon as possible. I have to submit my thesis soon, and I am looking forward to a quick reply from you. Thank you so much for your time and efforts. I appreciate your help, kindness, and understanding.

Best regards,
Lipsa

Figure B.1 Copyright permission for figures 1.1 and 1.2 in the Thesis

B.2 Permission from Nippon Steel

NIPPON STEEL CORPORATION

Research & Development Date: 11/18/2024

Request for permission to reproduce copyrighted material

Dear

I am preparing my Ph.D. dissertation entitled:

Modeling of Continuous Casting Mold Powder Behavior: Heat Transfer, Combustion, Sintering, and Melting

For submission to Thesis and Dissertations published by Colorado School of Mines at ProQuest.

I wish to have your permission to include in my article the following material:

Photo 1 (Melting process of mold powder in continuous casting), and Figure 14 (Change in calculated molten powder pool thickness and measured pool thickness in mold of continuous caster)

From the article written by Taketo Nakano, Kyoichi Nagano, Noriyoshi Masuo, Masao Fuji, Toshio Matsuyama.

in the publication "Model Analysis of Melting Process of Mold Powder for Continuous Casting of Steel" in Nippon Steel Technical Report No. 34, July 1987

If permission is granted for the use of this material, the author(s) and your publication will be credited as the source. If you would like the credit line to take any special form, please let me know what this should be.

I should be greatly appreciate if you would indicate your agreement by signing and returning one copy this form. Thank you for your cooperation.

Name: Lipsa Das
Affiliation: Colorado School of Mines
Fax:
E-mail: lipsadas@mines.edu

Ref. No.: 2024-38

Permission granted to reproduce the material specified above:

木下 恵介 (Signature of copyright holder/author)

11/21/2024 (Date)

Credit line to be used:

Figure B.2 Copyright permission for figures 1.3(b), 2.4, and 5.1(b) in the Thesis

B.3 Permission from Elseiver

ELSEVIER LICENSE
TERMS AND CONDITIONS

Nov 19, 2024

This Agreement between Lipsa Das/ Colorado School of Mines ("You") and Elsevier ("Elsevier") consists of your license details and the terms and conditions provided by Elsevier and Copyright Clearance Center.

License Number	5912700656432
License date	Nov 19, 2024
Licensed Content Publisher	Elsevier
Licensed Content Publication	International Journal of Heat and Fluid Flow
Licensed Content Title	Numerical study of flow and heat transfer in a molten flux layer
Licensed Content Author	B. Zhao,S.P. Vanka,B.G. Thomas
Licensed Content Date	Feb 1, 2005
Licensed Content Volume	26
Licensed Content Issue	1
Licensed Content Pages	14
Start Page	105
End Page	118

Figure B.3 Copyright permission for figures 2.1 and 2.2 in the Thesis

B.4 Permission from AIST Transactions (formerly Steelmaking Proceedings)

Thank you, Lipsa. Your request is approved.

From: Lipsa Das (Student) <lipsadas@mines.edu>
Sent: Friday, November 15, 2024 9:49 PM
To: Amanda Woods <awoods@aist.org>
Subject: RE: [EXTERNAL] Copyright Permission Request Confirmation- IMPORTANT

[External Email]

Dear Amanda,

I hope you are doing well. I am a PhD candidate at Mines planning to submit my Ph.D. Thesis soon. I have included a couple of figures from Steelmaking Proceedings in my thesis to cover the excellent work done by researchers as a part of my literature review. I have submitted the copyright permission form (with all the information given below in the confirmation email, also the copyright form is attached).

As per the university's rule of "using copyrighted material" (https://www.mines.edu/graduate-studies/thesis-writers-guide/),

"if you want to include in your thesis a Figure or Table from a source for which you were not an author (e.g. a journal article, textbook, website, technical report), you must OBTAIN and INCLUDE any necessary permissions from the original author and/or publisher. Otherwise, even if you cite the original source, you will be in violation of copyright law."

I have attached my request for permission to include two figures (used for my literature review in my PhD thesis- the figures are attached), from the research article by "***B. Xie, Y. Gan ,J. Wu. Study on amount and scheme of carbon mixed in cc mold fluxes. Steelmaking Proceedings, 74:647–651, 1991*** *(Figure 3), and* ***A. Delhalle, J. Marioton , M. Larrecq and P. Riboud. Slag melting and behaviour at meniscus level in a cc mold. Steelmaking Proceedings, 69:145–152, 1986*** *(figure 2)*.

Kindly allow me permission to use these figures from these papers. Please confirm your approval as soon as possible. I have to submit my thesis soon, and I am looking forward to a quick reply from you. Thank you so much for your time, and efforts. I appreciate your help, kindness, and understanding.

Best regards,
Lipsa

Figure B.4 Copyright permission for figures 2.3 and 2.5 in the Thesis

B.5 Permission from Iron and Steel Institute of Japan(ISIJ)

Dear Ms. Lipsa Das

Regarding Figure 2(b) and Figure 7 published in **ISIJ International Vol. 44 (2004), No. 5**, which was previously requested, we have granted permission to reproduce them under the CC license, provided that they are not modified.

We have also granted permission to reproduce Figure 4 published **in ISIJ Transactions Vol. 24 (1984)**, which was additionally requested.

As CC license applies, we will not send you a permission letter. Please feel free to use them, provided that you clearly indicate the source.

Best regards
Ms. Chiharu KAMEI
ISIJ

From: tensai <tensai@isij.or.jp>
Sent: Friday, November 15, 2024 12:06 AM
To: Lipsa Das (Student) <lipsadas@mines.edu>
Subject: [EXTERNAL] RE: Request to use copyrighted material in my PhD dissertation- Thank you!

Dear Mr./Ms. Lipsa Das
Do you modify the two figures ?
If “No”, you need not submit the permission request to me.
If “Yes”, I will get permission to reprint from my boss.
Best regards
(Ms.)Chiharu KAMEI, ISIJ
e-mail: tensai@isij.or.jp

From: Lipsa Das (Student) <lipsadas@mines.edu>
To: tensai <tensai@isij.or.jp>
Subject: IMP: Request to use copyrighted material in my PhD dissertation- Thank you!

Dear Sir/Ma'am,

I hope you are doing well. I am a PhD candidate at the Colorado School of Mines

I have attached my request for permission to include two figures (used for my model validation in my PhD thesis), from the research article by “*Mawin Supradist, Alan W. Cramb, Klaus Schwerdtfeger*” published in ***ISIJ International, Vol. 44 (2004), No. 5, pp. 817-826***. Kindly allow me permission to use these Figures 2b, and 7 from this work. Please confirm by sending an approval email containing the signed copyright permission form. I have to submit my thesis soon, and I am looking forward to a quick reply from you. Thank you so much for your time, and efforts. I appreciate your help, kindness, and understanding.

Figure B.5 Copyright permission for figures 2.6, and 5.7(a) in the Thesis

B.6 Permission from TATA Steel, IJmuiden, Netherlands

From: Senge, Stefan <Stefan.Senge@tatasteeleurope.com>
Sent: Thursday, November 21, 2024 5:12 AM
To: Lipsa Das (Student) <lipsadas@mines.edu>
Subject: RE: [EXTERNAL] RE: Permission to use optical micrographs of mold powder from TATA in my Ph.D. dissertation

Hi Lipsa,

It is approved.
Only the reference needs some adjustment.

Please use this in you reference list:
Jan Kromhout. Mold powders presentation. Tata Steel, R&D, IJmuiden, The Netherlands, personal communication.
Met vriendelijke groet / Kind regards,

Stefan
Stefan Senge
T: +31 (0) 251 4 93849
M: +31 (0)6 203 94 302
Sensitivity: general

From: Lipsa Das (Student) <lipsadas@mines.edu>
Sent: Wednesday, November 20, 2024 9:49 AM
To: Senge, Stefan <Stefan.Senge@tatasteeleurope.com>
Subject: RE: [EXTERNAL] RE: Permission to use optical micrographs of mold powder from TATA in my Ph.D. dissertation

External email

Dear Stefan,
Thanks a lot for your quick response. Much appreciated! I am very happy to know that the IP team seems positive about including the optical micrographs in our work. Please find attached the parts of my thesis where these images have been used and the reference list. Please let me know if I should modify Ref. 29 to present it in a certain form/detail. Kindly keep this confidential. Thank you so much for considering my request for copyright permission and for discussing this with your IP team. Thanks a lot for your time and efforts. I am excited to get your final approval.

Best regards,
Lipsa

Figure B.6 Copyright permission for figures 3.1, 4.1, and 5.2 (a)-(c) in the Thesis

B.7 Permission from former CCC researcher, Adnan Akhtar

Dear Lipsa,

Congratulations on defending your PhD.
Yes, you can use the figures that I generated for your thesis.

Regards
Adnan

On Fri, Nov 15, 2024 at 4:05 AM Lipsa Das (Student) <lipsadas@mines.edu> wrote:

Dear Adnan,

I hope you are doing well. I recently defended my Ph.D. thesis, and currently I am finalizing my thesis to submit it soon. I would like your permission to use the figures for Fluent mesh, properties for HSLA slag, and transient heating of cold powder that I used for model validation in my work (please see attached) in my thesis. Kindly let me know if I can use them with due credits given to you, and University of Illinois, Urbana Champaign for the images. Thanks a lot, I am looking forward to hearing from you.

Best regards,
Lipsa

Figure B.7 Copyright permission for figures 3.5 (a)-(b), 4.3 (a)-(b), and 4.4(b) in the Thesis

B.8 Permission from Iron and Steel Institute of Japan (ISIJ)

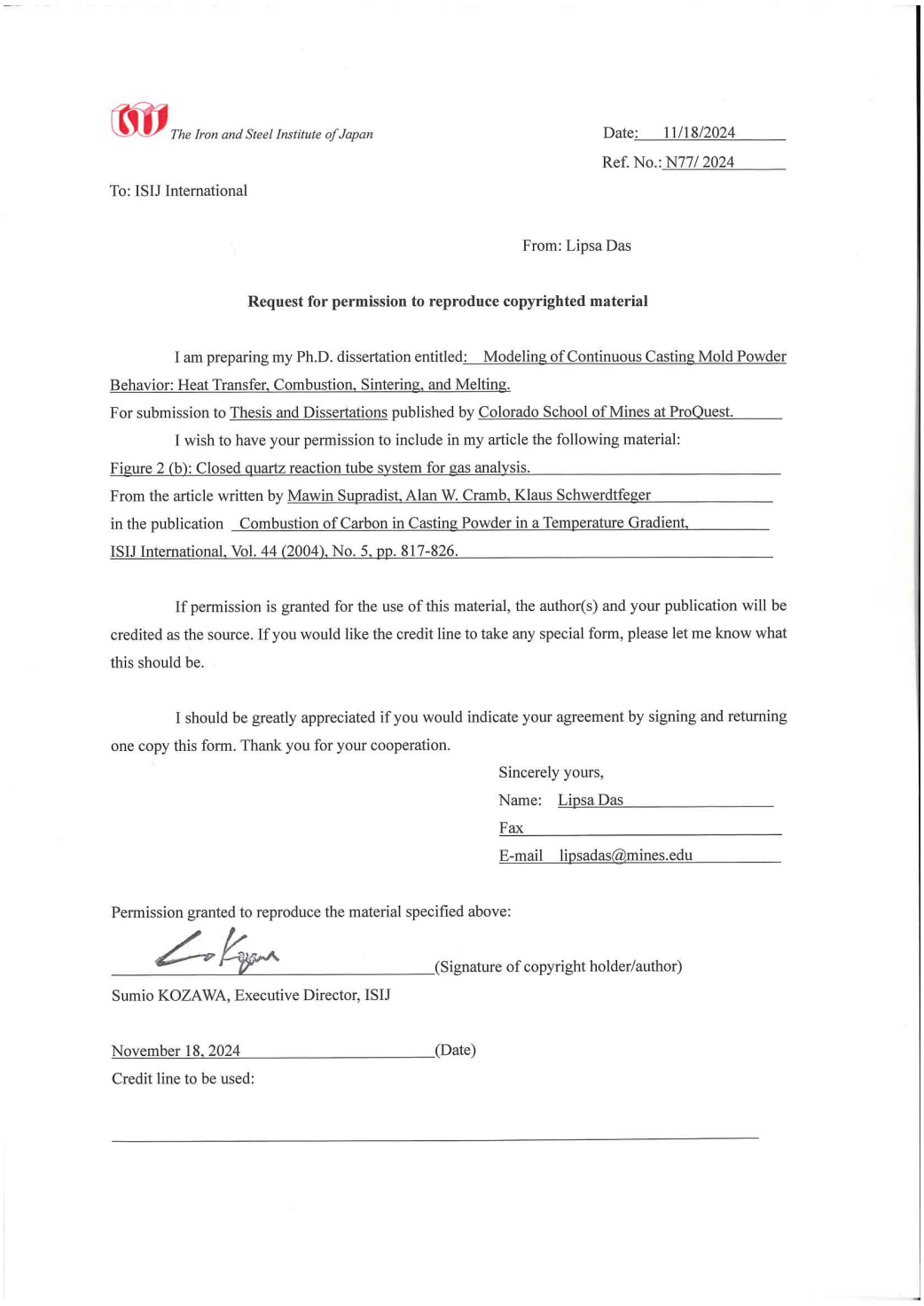

The Iron and Steel Institute of Japan

Date: 11/18/2024

Ref. No.: N77/ 2024

To: ISIJ International

From: Lipsa Das

Request for permission to reproduce copyrighted material

I am preparing my Ph.D. dissertation entitled: Modeling of Continuous Casting Mold Powder Behavior: Heat Transfer, Combustion, Sintering, and Melting.
For submission to Thesis and Dissertations published by Colorado School of Mines at ProQuest.

I wish to have your permission to include in my article the following material:
Figure 2 (b): Closed quartz reaction tube system for gas analysis.
From the article written by Mawin Supradist, Alan W. Cramb, Klaus Schwerdtfeger
in the publication Combustion of Carbon in Casting Powder in a Temperature Gradient,
ISIJ International, Vol. 44 (2004), No. 5, pp. 817-826.

If permission is granted for the use of this material, the author(s) and your publication will be credited as the source. If you would like the credit line to take any special form, please let me know what this should be.

I should be greatly appreciated if you would indicate your agreement by signing and returning one copy this form. Thank you for your cooperation.

Sincerely yours,
Name: Lipsa Das
Fax
E-mail lipsadas@mines.edu

Permission granted to reproduce the material specified above:

(Signature of copyright holder/author)
Sumio KOZAWA, Executive Director, ISIJ

November 18, 2024 (Date)
Credit line to be used:

Figure B.8 Copyright permission for figure 5.5 in the Thesis